Cryogenic Optomechanics with Silica Microresonators

by

Allison MacDonald

A thesis submitted in partial fulfillment of the requirements for the degree of

Master of Science

Department of Physics

University of Alberta

Abstract

Cavity optomechanical devices are interesting systems for probing quantum mechanical behaviour of mesoscopic objects. A basic requirement for these types of experiments is preparation of the mechanical resonator in, or at least very close to, its ground state. Although active laser cooling techniques can help this process, conventional cryogenic (pre-)cooling is nonetheless necessary.

This thesis introduces a custom-made apparatus, housed on the base plate of a commercial dilution refrigerator, for coupling light into an optomechanical resonator via a tapered optical fiber. Our system incorporates full three-dimensional control of the taper-resonator coupling conditions, enabling critical coupling at cryogenic temperatures. It also features an optical microscope which permits *in situ* imaging and alignment of the taper and resonator, while causing minimal heating to the environment.

Optomechanical measurements of silica bottle resonators, which exhibit optical whispering gallery modes and high-quality mechanical breathing modes, are performed using the dilution fridge system. Several methods for enhancing the detection of small mechanical signals are tested and a method for determining the temperature of the mechanical mode is described and implemented. The tight confinement of light circulating in the bottle resonator leads to increased optical absorption and significant heating of the silica, which manifests itself in both the optical and mechanical properties of the resonator. We present the first measurements of these resonators for mechanical mode temperatures as low as 4 K, and fridge temperatures down to 9 mK.

Preface

Much of the work presented in this thesis was accomplished through the collaborative efforts of a number of people in the Davis lab, including (but not limited to) Bradley Hauer (BH), Paul Kim (PK), Callum Doolin (CD), Hugh Ramp (HR), Thomas Clark (TC), Xavier Rojas (XR), Greg Popowich (GP), Aron Fredrick (AF), Alex Hoy (AH), Pearse Doolin (PD) and John Davis (JD).

The room temperature coupling chamber was designed by BH and TC, and constructed by BH, TC, myself and the University of Alberta physics machine shop. It was based upon the design of a very similar chamber, which was designed and built by BH and PK. This apparatus is described in [B. D. Hauer, P. H. Kim, C. Doolin, A. J. R. MacDonald, H. Ramp, and J. P. Davis. On-chip cavity optomechanical coupling. *EPJ Techniques and Instrumentation*, 1:4, 2014].

The dilution fridge coupling apparatus was designed by PK, BH, GP, XR, AH, myself and JD. The parts were fabricated and constructed by BH, PK, GP, XR, myself and the University of Alberta physics machine shop. Design and fabrication of the bottle mounts and fiber holders used at low temperature were done by BH, PK and myself. BH and I performed tests of gluing procedures for these mounts. The dilution fridge optical microscope was designed by GP, JD and myself. GP and I constructed the microscope. Initial room-temperature tests were performed by AF and myself. Details of this apparatus have been published in [A. J. R. MacDonald, G. G. Popowich, B. D. Hauer, P. H. Kim, A. Fredrick, X. Rojas, P. Doolin, and J. P. Davis. Optical microscope and tapered fiber coupling apparatus for a dilution refrigerator. *Review of Scientific Instruments*, 86(1):013107, 2015].

Bottle resonators and tapered fibers used in the experiments presented here were fabricated by BH and myself. The pulling apparatus was designed and built by BH. Initial measurements of bottle mechanical modes were performed by PD. BH and I performed COMSOL simulations of these modes.

TC, BH and I designed and implemented the optical detection schemes, including balanced optical homodyne detection. The data acquistion system was designed by CD and accompanying software was written by CD, HR and myself.

BH developed a genetic algorithm used for fitting the multistable optical resonances. BH and I elucidated the theory used for calibration of the mechanical mode temperature and for fitting nonlinear optical resonances.

Measurements and data analysis are my original work, in consultation with BH and JD.

Aside from the experiments presented in this thesis, I had supporting roles in experiments led by PK and CD featuring on-chip optomechanical devices consisting of torsional oscillators and cantilevers coupled to optical disks, as described in [P. H. Kim, C. Doolin, B. D. Hauer, A. J. R. MacDonald, M. R. Freeman, P. E. Barclay, and J. P. Davis. Nanoscale torsional optomechanics. *Applied Physics Letters*, 102(5):053102, 2013], [C. Doolin, P. H. Kim, B. D. Hauer, A. J. R. MacDonald, and J. P. Davis. Multidimensional optomechanical cantilevers for high-frequency force sensing. *New Journal of Physics*, 16:035001, 2014] and [C. Doolin, B. D. Hauer, P. H. Kim, A. J. R. MacDonald, H. Ramp, and J. P. Davis. Nonlinear optomechanics in the stationary regime. *Physical Review A*, 89(5):053838, 2014]. I also assisted with optical alignment and fitting algorithms for optomechanical experiments with buckled dome microcavities in [M. H. Bitarafan, H. Ramp, T. Allen, C. Potts, X. Rojas, A. MacDonald, J. P. Davis and R. G. DeCorby. Thermo-mechanical properties of buckled dome Fabry-Perot microcavities. *J. Opt. Soc. Am. B* 32(6):1132, 2015]. Finally, along with BH, I measured the depth of glass microfluidic cells using a white-light interferometric imaging system, published in [X. Rojas, B. D. Hauer, A. J. R. MacDonald, P. Saberi, Y. Yang and J. P. Davis. Ultrasonic interferometer for first-sound measurements of confined ^{4}He. *Physical Review B*, 89(17):174508, 2014].

To my parents, Anne and Gord.

Acknowledgements

I would like to begin by thanking my supervisor, Professor John Davis, for his steadfast guidance and (especially) optimism during the course of my degree work. His enthusiasm for science and unwavering belief that the next great discovery was just around the corner was refreshing and necessary to the success of the entire group, especially on those (not so infrequent) days when experimental success was particularly elusive. I am extremely appreciative of the very collaborative and supportive environment he has cultivated in the entire group, and for the freedom he has given each of us in pursuing our own interests.

I am also grateful to my comrades in the Davis lab who have been not just my colleagues during the last three years, but also my teammates and friends. Firstly, to the optomechanics team with whom all of my work was conducted: I can't imagine a better or more talented group of people to work with. I would like to thank Paul Kim, who designed much of the apparatus I used in this work and was the nanofab guru of the team; Callum Doolin, who programmed almost all of the instruments I used and who was ever-patient in helping me understand them; Hugh Ramp, who not only let me distract him with my coding and Latex issues, but was also an awesome office-mate and let me eat all the cookies; and Brad Hauer, who was my partner in the low temp optomechanics experiment and the theory engine of the entire lab. I am also grateful to Xavier Rojas and Fabien Souris, who were both generous in sharing their knowledge of low temperature physics and in encouraging me to practice my French. I would like to thank Tushar for his helpful discussions on a number of topics and his great humour. To all the summer students who worked in our group over the years, especially Parnian Saberi, Tommy Clark and Brynn Lewis, with whom I had the pleasure of working with directly, thank you for you hard work and companionship. Finally, I would like to thank Yikai Yang, Abdul Suhel, Ruhul Amin and Kyle Reid, with whom I had less overlap but who were nonetheless wonderful friends and colleagues.

I owe a debt of gratitude to Greg Popowich, who designed much of the dilution fridge apparatus and who provided answers to my seemingly unending questions. The staff of the physics machine shop were also incredibly helpful in solving many of the practical problems that arose in my experiment.

I would like to thank my committee members, Professors Frank Hegmann and Lindsay LeBlanc, for the guidance and occasional loan of lab equipment. The groups of Professors Mark Freeman and Wayne Hiebert were also generous in lending both equipment and expertise. I would also like to thank my previous mentors at McMaster, Waterloo and SFU, who cultivated in me a love of science and patiently endeavoured to teach me something of their respective fields along the way.

To my friends here, thank you for the pub nights, sports teams and thanksgiving dinners. To my friends at home, thank you for putting up with yet another rescheduled Skype call and for always finding time for me during my sometimes very brief appearances in Ontario.

I would like to thank my adopted Alberta families, especially the Hauer/Pratt clan who have welcomed me so warmly into their fold and the Viscount Park Pipe Band, who made Edmonton much more my home than I could have hoped for. You kept the gift of music in my life and made band practice a joy even when it meant coercing me out of the lab after yet another long week.

Finally, I am deeply indebted to my other half, Brad, who supported me in innumerable ways and who proofread this entire thesis, as well as to my family, especially my parents and my sister, Kimberley, who have continued to believe in me and encourage me to pursue my passions. There is nothing that quite compares to the unconditional love and encouragement you have shown me; I hope that someday I can prove myself worthy of it.

Contents

List of Tables

List of Figures

List of Symbols and Abbreviations

A	fit amplitude of $S_{VV}(\omega)$ [$\mathrm{V}^2/\mathrm{s}^2$]	16
A_{mech}	area under the mechanical peak [V^2]	93
A_{mod}	area under the phase modulation peak [V^2]	93
G	optomechanical coupling strength [GHz/nm]	19
P	input laser power [W]	9
Q_{m}	mechanical quality factor	15
Q_{opt}	optical quality factor	7
R	radius [m]	5
$R_{4.2}$	ratio corresponding to $T = 4.2$ K	95
R_{T}	ratio of A_{mech} to A_{mod} at temperature T	93
$S_{VV}(\omega)$	voltage power spectral density [V^2/Hz]	15
$S_{\phi\phi}(\omega)$	phase modulation power spectral density [rad^2/Hz]	92
$S_{xx}(\omega)$	displacement power spectral density [m^2/Hz]	13
T	temperature [K]	3
V_{π}	voltage required to produce a π phase shift across the EOM [V]	88
Δ	laser detuning [2π Hz]	9
Δ_{nl}	nonlinear detuning parameter [2π Hz]	72
$\Delta_{\mathrm{nl}}^{(2)}$	second-order nonlinear detuning parameter [2π Hz]	81
Γ	mechanical damping rate [2π Hz]	13
Γ_{OM}	optomechanical damping rate [2π Hz]	22
Ω_{mod}	EOM modulation angular frequency [2π Hz]	88
Ω_{m}	mechanical angular resonance frequency [2π Hz]	3

α	mechanical transduction coefficient [$\mathrm{V}^2/\mathrm{m}^2$]	16
α_{mod}	phase modulation transduction coefficient [$\mathrm{V}^2/\mathrm{rad}^2$]	92
$\bar{\Delta}$	renormalized laser detuning including the optomechanical interaction [2π Hz]	21
$\bar{a}$	steady-state cavity field [$\sqrt{\text{photons}}$]	9
$\bar{n}$	average phonon occupation	2
β	phase modulation depth [rad]	88
γ	linewidth of the phase modulation [2π Hz]	91
$\hat{a}(\hat{a}^\dagger)$	photon annihilation (creation) operator	19
$\hat{b}(\hat{b}^\dagger)$	phonon annihilation (creation) operator	19
$\hbar$	reduced Planck constant [1.054×10^{-34} Js]	3
κ	total optical decay rate [2π Hz]	7
κ_0	intrinsic optical decay rate [2π Hz]	7
κ_{ex}	external optical decay rate [2π Hz]	7
λ_{o}	resonant wavelength [nm]	7
ω_o	optical angular resonance frequency [2π Hz]	7
ξ	optomechanical modulation strength	88
a	intracavity light field [$\sqrt{\text{photons}}$]	9
c	speed of light [2.98×10^8 m/s]	5
f_{m}	natural mechanical resonance frequency [Hz]	15
g	field-enhanced optomechanical coupling rate [2π Hz]	22
g_0	vacuum optomechanical coupling rate [2π Hz]	19
k_{B}	Boltzmann constant [1.38×10^{-23} J/K]	3
m_{eff}	effective mass [kg]	13
n_0	material index of refraction	5
n_{cav}	number of photons in the cavity	9
s_{in}	input optical amplitude [$\sqrt{\text{photons/s}}$]	9
s_{out}	output optical amplitude from the cavity [$\sqrt{\text{photons/s}}$]	10
$x(t)$	position of the mechanical resonator [m]	12
x_0	amplitude of the mechanical resonator's motion [m]	14

x_{zpf}	amplitude of mechanical zero-point fluctuations [m]	19
ADC	analog-to-digital converter	58
AOM	acousto-optic modulator	64
APD	avalanche photodiode	59
BPD	balanced photodetector	63
CCD	charge-coupled device	48
CMOS	complementary metal-oxide-semiconductor	49
DAQ	data acquisition	55
EDFA	erbium-doped fiber amplifier	59
EOM	electro-optic modulator	88
FPC	fiber polarization controller	59
FT	fine tuning	57
HeNe	Helium-Neon	48
HPF	high-pass filter	58
IVC	inner vacuum can	38
LC	inductor-capacitor	1
LED	light-emitting diode	49
LN_2	liquid nitrogen	38
LPF	low-pass filter	58
MEMS	micro-electromechanical system	59
MZI	Mach-Zehnder interferometer	59
OFHC	oxygen-free high conductivity	45
OVC	outer vacuum can	38
PD	photodiode	30
PI	proportional-integrator	65
PM	power meter	59
PSD	power spectral density	13
QND	quantum non-demolition	2
RF	radio frequency	48

TE	transverse electric	5
TM	transverse magnetic	5
VC	variable coupler	59
VOA	variable optical attenuator	59
WDM	wavelength division multiplexer	59
WGM	whispering gallery mode	4

CHAPTER 1

Introduction

Nano- and micro-mechanical resonators are promising devices for a wide range of practical and fundamental science applications. Their small masses, high frequencies and versatility in coupling to other systems make them suitable sensors of a number of phenomena on very small scales [1]. Recent experimental successes include the detection of a single virus [2], as well as coupling to individual superconducting qubits [3, 4] and spins [5]. The remarkably small motion of these mechanical oscillators can be transduced in a number of ways, including piezoresistively [6], capacitively [3], or interferometrically [7, 8]. As improvements in modern fabrication techniques continue to push towards reduced physical dimensions, these detection methods tend to scale poorly.

By contrast, cavity optomechanical systems [9, 10, 11, 12] consisting of coupled mechanical and optical resonators scale more favourably due to the resonant optical enhancement provided by the cavity. These systems include Fabry-Pérot-type cavities with moving mirrors [13], membrane-in-the-middle setups [14], coupled photonic and phononic crystal structures [15], superconducting inductor-capacitor (LC) circuits [16, 17], clouds of atoms trapped within optical cavities [18], whispering gallery mode resonators with moving boundary conditions [19, 20] and mechanical oscillators coupled to optical cavities via the near-field [21, 22]. Such optomechanical systems have demonstrated the ability to make continuous measurements of mechanical motion with precision near or below the standard quantum limit imposed by back action of the measurement device on the probed system [18, 23, 24]. Although cavity optomechanics has its origins in gravity-wave observatories with mirrors spaced kilometres apart [25], optomechanical systems have also been proven extremely sensitive on much smaller scales. They have been demonstrated to be exquisite sensors of position [23], force [21, 26, 27], torque [22, 28], and acceleration [29]. Furthermore, the relative ease with which the mechanical element can be adapted to couple to many other systems makes optomechanical systems interesting candidates for quantum information processing architectures [30, 31].

The optomechanical interaction itself can be exploited to prepare exotic states of both light and mechanics, including mechanical Fock states [32, 33], squeezed states [34] and entangled states [35, 36]. A phenomenon analogous to electromagnetically-induced transparency, termed optomechanically-induced transparency, is observed in these systems [37, 38], and has promising applications for storage of classical and quantum states of light [39], as well as for converting optical photons from one wavelength to another [40, 41, 42, 43].

Finally, the relatively large size of the mechanical oscillator elements, which are composed of a large number of atoms, make them interesting for probing the validity of quantum mechanics at larger scales. The observation of the quantum mechanical behaviour of a nano- or micro-mechanical resonator, which more closely resembles our everyday experiences than most systems conventionally described as "quantum", is a major focus of the optomechanics community. A method of accomplishing this would be to perform a quantum non-demolition (QND) measurement of the energy of the resonator, in the hopes of measuring quantized jumps in the resonator's phonon occupation [33]. One very important prerequisite to performing these types of measurements is preparation of the mechanical oscillator in or very near its ground state. This cannot be accomplished without passive cryogenic cooling of the device, although active laser cooling techniques may also be necessary.

To that end, we have constructed an apparatus to facilitate optical coupling from a tapered optical fiber to optomechanical devices inside a commercial dilution refrigerator. In contrast to other contemporary optical-frequency systems, which use helium flow cryostats [19, 44, 45] with limited base temperatures or lossy and rigid on-chip coupling techniques inside dilution refrigerators [46], the system described here is more versatile, allowing full control over the coupling conditions and cross-compatibility between on- and off-chip devices at temperatures as low as 9 mK. A notable improvement over other systems is the construction of an optical microscope, based on the use of a coherent bundle of optical fibers, inside the fridge that allows alignment of a tapered optical fiber to a resonator through *in situ* imaging of the device with a resolution of 1 μm [47].

To test this system, cryogenic measurements were made using bottle optomechanical resonators [48, 49]. Bottles are silica optical whispering gallery mode cavities fabricated by melting standard optical fibers into spheroidally-shaped objects supported by stems along the original fiber axis, as shown in Figure 1.1. These resonators are of interest in our experiments because they possess high-frequency mechanical breathing modes. Since the average number of phonons, $\bar{n}$, is described by the Bose-Einstein distribution

$$\bar{n} = \frac{1}{e^{\hbar\Omega_m/k_BT} - 1}, \tag{1.1}$$

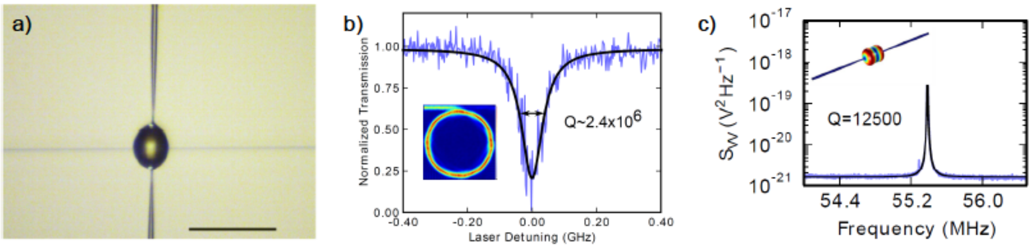

Figure 1.1: (a) Photograph of a bottle resonator and tapered fiber, used for coupling input light (scalebar 100 μm). (b) Optical resonance of the bottle with inset simulated optical mode shape. (c) Power spectral density of a bottle mechanical mode with inset simulated mechanical modeshape. The bottle resonator exhibits large optomechanical coupling thanks to the significant overlap in the optical and mechanical modes, which are both localized near the equator of the bottle.

modes with higher mechanical frequency Ω_m will have a lower average phonon occupation for a given temperature T. Here, $\hbar$ is the reduced Planck constant and k_B is the Boltzmann constant. Furthermore, the significant overlap between the bottle optical and mechanical modes (shown in Figure 1.1) leads to a large optomechanical coupling. This, along with the high-quality nature (denoted by Q in Figure 1.1) of the optical and mechanical modes, facilitates detection of the mechanical motion at low $\bar{n}$.

Bottle resonators also exhibit extremely tight confinement of circulating light [49], have large evanescent fields that can be used for various sensing applications [50, 51] and have highly tunable optical resonance spectra through the application of tension to the stems [49, 52]. They are transparent to both visible and near-infrared wavelengths and support high-quality mechanical breathing modes [47], making them promising candidates for wavelength-conversion [40, 42, 41] and optical pulse storage [39] applications.

The rest of the thesis is outlined as follows: Chapter 2 describes the theory of optical and mechanical resonators, as well as their coupling through the optomechanical interaction. Chapter 3 outlines the apparatus and methods used in the experiments performed in this thesis, including the optical microscope which is the subject of Ref. 47. Chapter 4 presents the results of optical and mechanical characterizations of the bottle resonators performed at ambient and cryogenic temperatures. It also outlines a method for calibrating the temperature of the mechanical mode based on an optical signal. Finally, Chapter 5 briefly summarizes the work and discusses the possible directions for future low temperature optomechanics experiments. Appendix A gives a detailed derivation of the mechanical mode thermometry presented in Chapter 4.

CHAPTER 2

Theory

In this chapter, we outline the theory required to understand the experiments that follow. We begin by describing the optical modes of whispering gallery mode resonators in Section 2.1 and the mechanism for coupling light into these resonators via tapered optical fibers in Section 2.2. Next, we describe in Section 2.3 the spectral response of a damped harmonic oscillator and its calibration in the case of thermally-driven motion. Finally, we describe the interaction between coupled optical and mechanical resonators through both a Hamiltonian formalism and coupled equations of motion in Section 2.4, and discuss active and passive cooling techniques in Section 2.5.

2.1 Optical Resonators

Optical resonators, including Fabry-Pérot-like cavities which confine light by multiple reflections between end mirrors [13, 14, 53], photonic crystal structures which trap light in defects of a regular lattice [15, 54, 55, 56], LC circuits [16, 17, 35], and whispering gallery mode (WGM) resonators [49, 57, 58, 59], spatially and temporally confine light, leading to an enhancement in the stored optical field. Here we focus on WGM resonators, which were first understood in the context of acoustic waves at St. Paul's Cathedral in London [60]. Lord Rayleigh realized that whispers of certain pitches travelled along the outer wall of the cathedral's dome to return to the speaker. Optical WGMs function in a similar manner: light waves circulate near the exterior of a circular cross-section of dielectric structures such as spheres, bottles, toroids and disks.

The strong optical field enhancement in WGM resonators makes them useful in applications requiring large optical intensities such as harmonic generation [58, 61], Raman lasing [62], optical parametric oscillation [63, 64] and frequency comb generation [65]. Furthermore, because WGMs circulate near the outer surface of a dielectric, they have a large evanescent field which facilitates interactions with other systems in the near field. Thus WGMs can be used for refractometric [66, 67] and microfluidic sensing [50, 51, 68], virus detection [69, 70], and cavity quantum elecrodynamics [71], as well as coupling to quantum dots [59] and nitrogen-vacancy centres in diamond [72], both of which are promising in quantum information applications.

2.1.1 Whispering Gallery Modes[1]

The field profiles of spherical WGM resonators with radius R can be determined analytically beginning with Maxwell's equations in a homogeneous volume without free charges or currents. From these, the wave equations of the electric ($\vec{E}$) and magnetic ($\vec{B}$) fields are given by

$$\vec{\nabla}^2 \vec{E} = \left(\frac{n_0}{c}\right)^2 \frac{\partial^2 \vec{E}}{\partial t^2} \tag{2.1}$$

$$\vec{\nabla}^2 \vec{B} = \left(\frac{n_0}{c}\right)^2 \frac{\partial^2 \vec{B}}{\partial t^2}, \tag{2.2}$$

where n_0 is the refractive index of the medium and c is the speed of light in vacuum. Assuming a plane-wave time dependence, $\vec{E}(t), \vec{B}(t) \propto e^{\pm i\omega t}$, we obtain the Helmholtz equations

$$\left(\vec{\nabla}^2 + k^2\right) \vec{E} = 0 \tag{2.3}$$

$$\left(\vec{\nabla}^2 + k^2\right) \vec{B} = 0, \tag{2.4}$$

where $k = \omega n_0/c$ is the wavevector of the resulting electromagnetic wave and ω is its angular frequency. Since the modes of interest arise in spherical objects, we will use spherical coordinates, defined by the radius $r \in [0, \infty)$, the azimuthal angle $\phi \in [0, 2\pi)$ and the polar angle $\theta \in [0, \pi)$

Equations (2.3) and (2.4) are vector equations, with solutions for each of the vector components E_i, B_i where $i \in \{r, \phi, \theta\}$. These modes are polarized predominantly in the $\hat{\theta}$ direction, as confirmed by numerical simulations [73] so we solve for only B_θ and E_θ for transverse magnetic (TM) and transverse electric (TE) modes, respectively.

---

[1] This discussion follows Ref. [73] and [74] closely.

We can then write Equations (2.3) and (2.4) as scalar equations, which have separable solutions ψ for each of the coordinates

$$E_\theta, B_\theta = \Psi_{qlm}(r,\phi,\theta) = N\psi_r(r)\psi_\phi(\phi)\psi_\theta(\theta) \tag{2.5}$$

where N is a normalization constant, and q, l, m are numbers which label the mode. Whispering gallery modes are characterized by a high azimuthal mode order $m \gg 1$ and low polar mode order $l - |m|$, such that $l \sim |m|$.

Inserting Equation (2.5) into Equations (2.3) and (2.4), and separating the variables yields three differential equations, one for each coordinate

$$\frac{1}{\psi_\phi}\frac{d^2\psi_\phi}{d\phi^2} = -m^2 \tag{2.6}$$

$$\cos\theta\frac{d}{d\theta}\left(\cos\theta\frac{d\psi_\theta}{d\theta}\right) - m^2\psi_\theta + l(l+1)\psi_\theta\cos^2\theta = 0 \tag{2.7}$$

$$\frac{1}{\psi_r}\frac{d}{dr}\left(r^2\frac{d\psi_r}{dr}\right) + k^2r^2 - l(l+1) = 0, \tag{2.8}$$

The solutions to the azimuthal and polar differential equations are given by the spherical harmonics $Y_l^m(\theta,\phi)$, which are derived from the Legendre polynomials $P_l^m(\cos\theta)$,

$$\psi_\theta(\theta)\psi_\phi(\phi) = Y_l^m(\theta,\phi) = P_l^m(\cos\theta)e^{\pm im\phi}. \tag{2.9}$$

The solutions to the radial equation are given by the spherical Bessel functions $j_l(kn_0r)$ inside the sphere. Outside of the sphere, the field can be approximated as exponentially decaying [73, 74]. The entire radial solution is thus given by

$$\psi_r(r) = \begin{cases} Bj_l(n_0kr) & \text{if } r \leq R \\ C\exp(-\alpha_s(r-R)) & \text{if } r > R. \end{cases} \tag{2.10}$$

In the above, $\alpha_s = \sqrt{\beta_l^2 - k^2n'^2}$ and the propagation constant is $\beta_l = \sqrt{l(l+1)}R$, where n' is the index of the surrounding medium (usually air or vacuum). B and C are normalization constants.

The characteristic equation for each mode can be determined by solving the boundary conditions imposed by Maxwell's equations at $r = R$ for each of the TE and TM modes. The resulting wavevector k is given by [73]

$$\left(\eta_s\alpha_s + \frac{l}{R}\right) j_l(kn_0R) = kn_0 j_{l+1}(kn_0R), \tag{2.11}$$

where $\eta_s = 1$ for TE modes and $\eta_s = n_0^2/n'^2$ for TM modes.

For purely equatorial modes ($l = |m|$), the resonance condition is given by [74, 75]

$$l = \frac{2\pi R n_0 c_1}{\lambda_\mathrm{o}}, \tag{2.12}$$

for resonant vacuum wavelength λ_o. The constant c_1 accounts for the fact that the mode is not completely confined to the sphere and has non-negligible amplitude in the evanescent field at $r > R$.

2.1.2 Characteristics of Optical Resonators

The modes of an optical cavity are characterized by a number of parameters. The simplest is the resonant frequency (ω_o) or wavelength (λ_o), which is defined by the resonance condition in Equation (2.12) for equatorial WGMs. This is simply the frequency of light at which maximum constructive interference occurs inside the resonator. An optical resonator can have more than one mode and thus multiple resonant frequencies.

The spectral linewidth of one of these optical resonances is given by its total decay rate κ, which for the purposes of this thesis will be defined as the full width at half maximum of the resonance lineshape. This parameter describes the rate at which photons are lost from the optical mode. These loss mechanisms can be further classified as intrinsic, given by the rate κ_0, or external, given by κ_ex. The total loss rate is the sum of these contributions,

$$\kappa = \kappa_0 + \kappa_\mathrm{ex}. \tag{2.13}$$

The external loss rate κ_ex is also referred to as the coupling rate, since it describes the rate at which photons are coupled into or out of the optical cavity from external optical fields. Intrinsic loss arises from a number of sources including material absorption, scattering losses, absorption by impurities and bending losses in WGMs [76]. The lifetime τ of a photon in the cavity is given by the inverse of the decay rate,

$$\tau = 1/\kappa. \tag{2.14}$$

From the lifetime, we can specify the optical quality factor Q_opt,

$$Q_{\mathrm{opt}} = \tau\omega_{\mathrm{o}} = \omega_{\mathrm{o}}/\kappa, \tag{2.15}$$

which describes the temporal confinement of the light in the cavity. For spherical WGMs, Q_{opt} of up to 10^{10}, limited only by material absorption and Rayleigh scattering, have been observed at visible wavelengths [77].

Finally, the mode volume [78],

$$V_0 = \int dV \left(\frac{\sqrt{\varepsilon}|E|}{\max(|\sqrt{\varepsilon}E|)} \right)^2 , \tag{2.16}$$

of the optical cavity is a measure of the spatial confinement of light within the optical mode of the dielectric. Here, ε is the dielectric constant and the integral is defined over the real-space volume of the resonator. The ratio of Q/V_0 is an important metric in determining the strength of the light-matter interaction in an optical resonator, with the highest Q/V_0 ratios demonstrated in WGM resonators [79].

2.2 Tapered Fiber Coupling to WGM Resonators

There are several methods that can be used to couple light into and out of a whispering gallery mode resonator. These include grating couplers [80] or lensed fibers [24] leading to on-chip tapered waveguides and prism coupling [81, 82]. We use tapered fiber coupling, due to its superior phase-matching and coupling efficiency [59, 83, 84], for coupling to both the bottle resonators investigated in this thesis and on-chip optomechanical devices described elsewhere [22, 26, 85, 86, 87].

Standard single mode optical fibers support a single propagating optical mode in the wavelength range of interest through total internal reflection of light between the core of the fiber and its lower-index cladding. For optical fibers which are single mode at 1550 nm, an 8 μm diameter core and 125 μm cladding confine most of the mode in the core, with a small fraction of the light propagating in the evanescent field in the cladding. Tapered fibers consist of a much thinner core (see Table 2.1) clad by vacuum or air (or in some instances, water [67]), resulting in a larger evanescent field. For the tapers in this thesis, the diameter of a single mode optical fiber is adiabatically reduced to a size of $\sim$1 μm with an exponential profile [86, 88]. Coupling of light from the guided taper mode to the optical resonator mode occurs through an overlap of the evanescent fields of the two modes or, in an equivalent picture, through frustrated total internal reflection [73]. Here, we describe theoretically the coupled taper-resonator system. Technical details of fabricating tapered fibers are described in Section 3.1.

λ (nm)	n_{co}	n_{cl}	d_{c} (nm)	
			WGA	Numerical
637	1.47	1.00	452.6	452.6
	1.47	1.33	778.8	778.9
780	1.47	1.00	554.1	554.2
	1.47	1.33	953.6	953.7
1310	1.47	1.00	930.7	930.7
	1.47	1.33	1601.6	1601.7
1550	1.47	1.00	1101.2	1101.2
	1.47	1.33	1895.0	1895.1

Table 2.1: Single mode cutoff diameter (largest diameter at which only a single optical mode is supported) of a glass core ($n_{\mathrm{co}} = 1.47$) tapered fiber for the wavelength and medium of interest ($n_{\mathrm{cl}} = 1.00$ for air/vacuum and 1.33 for water). Diameters calculated analytically using the weakly guided approximation (WGA) and numerically in Ref. 86. Most of the tapered fibers used in this thesis have diameters of $\sim$1 μm, suitable for 1550 nm light in air or vacuum. Reproduced from Ref. 86 under the Creative Commons Attribution License Agreement.

2.2.1 Optical Input-Output Theory

For the work discussed in this thesis, we will work in the regime of large photon numbers, so it is sufficient to consider only the classical equation of motion for the optical field inside the cavity. Following Ref. 11, we write the equation of motion for light in an optical cavity coupled to an input field at rate κ_{ex} as

$$\dot{a} = -\frac{\kappa}{2}a + i\Delta a + \sqrt{\kappa_{\mathrm{ex}}}s_{\mathrm{in}} \tag{2.17}$$

in the frame rotating at the drive laser frequency ω_{L}. We will call a the optical field in the cavity although it is normalized in terms of photon number such that

$$n_{\mathrm{cav}} = |a|^2 \tag{2.18}$$

is the number of photons in the cavity. Here, κ is the total optical decay rate, κ_{ex} is the coupling rate, $\Delta = \omega_{\mathrm{L}} - \omega_{\mathrm{o}}$ is the laser detuning from the optical resonance and s_{in} is a complex amplitude which has units of $\sqrt{\mathrm{photons/s}}$, such that $|s_{\mathrm{in}}|^2 = P/\hbar\omega_{\mathrm{L}}$ is the rate of photons incident on the cavity-taper junction for a given input power P.

We can solve for the steady-state field $\bar{a}$ inside the cavity at a particular laser detuning by setting $\dot{a} = 0$. This gives

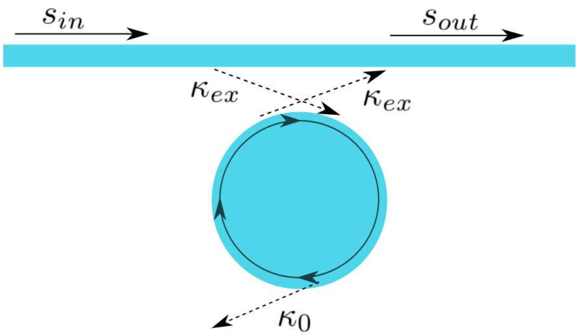

Figure 2.1: Schematic depicting coupling (κ_{ex}) from the tapered fiber to the resonator, and intrinsic loss (κ_0) of the resonator.

$$\bar{a} = \frac{\sqrt{\kappa_{\mathrm{ex}}}}{\frac{\kappa}{2} - i\Delta} s_{\mathrm{in}}. \tag{2.19}$$

The number of photons in the cavity is then given by

$$n_{\mathrm{cav}} = \frac{\kappa_{\mathrm{ex}}}{\frac{\kappa^2}{4} + \Delta^2} |s_{\mathrm{in}}|^2. \tag{2.20}$$

At the output of the cavity, the output optical amplitude s_{out} is given by

$$s_{\mathrm{out}} = s_{\mathrm{in}} - \sqrt{\kappa_{\mathrm{ex}}} a \tag{2.21}$$

such that the rate of photons output by the cavity $\dot{n}_{\mathrm{out}} = |s_{\mathrm{out}}|^2$ is then

$$\dot{n}_{\mathrm{out}} = |s_{\mathrm{in}}|^2 \left(1 - \frac{\kappa_0 \kappa_{\mathrm{ex}}}{\frac{\kappa^2}{4} + \Delta^2} \right) \tag{2.22}$$

and the phase of the output light, ϕ_{out}, is

$$\phi_{\mathrm{out}} = \arctan \left(\frac{-\kappa_{\mathrm{ex}} \Delta}{\frac{\kappa}{4} (\kappa - 2\kappa_{\mathrm{ex}}) + \Delta^2} \right). \tag{2.23}$$

For the experiments presented here, $\kappa_0/2\pi$ is typically in the range of $10 - 30$ MHz, while $\kappa_{\mathrm{ex}}/2\pi$ can vary from MHz to GHz. With input powers of $P = 0.1 - 100$ μW ($|s_{\mathrm{in}}|^2 \approx 10^{11} - 10^{15}$ photons/s for wavelengths around 1550 nm), there are between 10^3 and 10^7 photons in the cavity when the laser is on-resonance.

2.2.1.1 Coupling Regimes

Fitting an optical resonance with Equation (2.22), we can extract the optical resonance frequency ω_o (from the detuning Δ) and the total decay rate κ of the resonance, which in turn gives access to the optical quality factor via $Q_\mathrm{opt} = \omega_\mathrm{o}/\kappa$. We can also in principle extract both κ_ex and κ_0 from the on-resonance normalized transmission minimum ($T_\mathrm{min} = \dot{n}_\mathrm{out}/|s_\mathrm{in}|^2$ at $\Delta = 0$) given by

$$T_\mathrm{min} = 1 - \frac{4\kappa_\mathrm{ex}\kappa_0}{\kappa^2}. \tag{2.24}$$

However, since κ_0 and κ_ex appear symmetrically in Equation (2.24), there is some ambiguity between the two solutions, which we will call $\kappa_\pm$, of this equation:

$$\kappa_\pm = \frac{\kappa}{2} \pm \frac{\kappa}{2}\sqrt{T_\mathrm{min}}. \tag{2.25}$$

Either κ_+ or κ_- corresponds to κ_0 but it is not clear from Equation (2.25) which. There are then three distinct coupling regimes in the taper-resonator system which determine the characteristics of the resonance. The first is the under-coupled regime, in which cavity photons are primarily lost through internal mechanisms ($\kappa_0 > \kappa_\mathrm{ex}$). If instead photons are coupled to and from the input waveguide at a much faster rate than they are lost through intrinsic cavity decay mechanisms ($\kappa_\mathrm{ex} > \kappa_0$), then the resonator is said to be over-coupled. This regime is useful for applications requiring minimal optical losses of the input photons [89], such as generating entanglement between the input light field and the mechanical oscillations of an optomechanical resonator [35, 36].

Finally, between under- and over-coupling is the critical coupling condition, which occurs when $\kappa_\mathrm{ex} = \kappa_0$. Experimentally, this condition occurs only for good phase-, polarization- and mode-matching between the input taper mode and the cavity optical mode. If this condition is met, then extinction of the transmission can be observed on-resonance [84, 90], as seen in Equation (2.24). Figure 2.2 illustrates the qualitatively different appearance of the phase and transmission spectra of the resonance for under-, critically- and over-coupled resonances. Note that the change in the phase of the transmitted light between the blue- and red-detuned sides of the resonance is much more pronounced for over-coupling, meaning that κ_ex and κ_0 can be identified if phase information is available [91, 92].

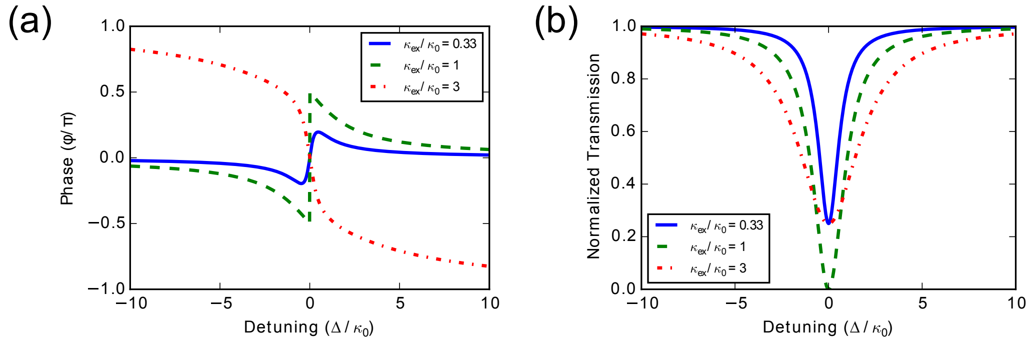

Figure 2.2: (a) Calculated phase (Equation (2.23)) and (b) normalized transmission (Equation (2.22)) of output light across an optical resonance with fixed intrinsic decay rate κ_0 and increasing external coupling κ_{ex} for an under- (solid blue), critically- (dashed green) and over-coupled (dotted red) resonance.

2.3 Mechanical Resonators

Nano- and micro-mechanical oscillators are of increasing interest in both fundamental metrological studies and small-scale sensing applications. Their mesoscopic size makes them ideal for testing the fundamental limits of quantum mechanics [4, 93] and their versatility in coupling to other systems of interest make them ideally suited for use as biological [2, 94], mass [95, 96] and torque sensors [7, 22, 28], as well as for coupling to single spins [5] or qubits [3].

2.3.1 Thermomechcanical Calibration of Resonator Motion[2]

If a mechanical resonator is subject only to incoherent thermal forces, a measurement of its motion can be calibrated to give the absolute displacement given prior knowledge of a few simple parameters. This is important for both sensing applications and fundamental tests of quantum mechanics.

2.3.1.1 Power Spectral Densities

First, let us consider the position of a mechanical resonator as a function of time, denoted by $x(t)$. Suppose that we measure $x(t)$ by some process (how is not important just yet, but in our experiments we will use WGMs to transduce the motion as an optical signal). Then we can calculate its autocorrelation function as

---

[2] The following discussion follows closely from Ref. [97].

$$R_{xx}(t) = \lim_{\tau_\mathrm{m}\to\infty} \frac{1}{\tau_\mathrm{m}} \int_0^{\tau_\mathrm{m}} dt'\, x(t')x(t'+t), \tag{2.26}$$

where τ_m is the measurement time.

The two-sided power spectral density (PSD) of $x(t)$, $P_{xx}(\omega)$, is defined as the Fourier transform of R_{xx}, yielding

$$P_{xx}(\omega) = \int_{-\infty}^{+\infty} dt\, R_{xx}(t) e^{i\omega t}. \tag{2.27}$$

$P_{xx}(\omega)$ is a function, defined over all positive and negative frequencies, which will be proportional to the total energy in the signal $x(t)$ when integrated over the entire frequency domain. In most experiments, negative frequencies are not physical, so we define the single-sided PSD $S_{xx}(\omega)$ over positive frequencies such that $\int_{-\infty}^{+\infty} P_{xx}(\omega)\, d\omega = \int_0^{+\infty} S_{xx}(\omega)\, d\omega$. Since any physically meaningful classical $P_{xx}(\omega)$ is an even function, $S_{xx}(\omega) = 2P_{xx}(\omega)$ in the positive frequency domain.

2.3.1.2 The Damped Harmonic Oscillator

We can model each of the resonator's modes as a damped harmonic oscillator driven only by incoherent thermal forces $F(t)$. We will consider only one mode, although our analysis holds equally well for any mode of the mechanical resonator, given the appropriate set of parameters. We can write down the equation of motion for the position of the resonator $x(t)$ as

$$m_\mathrm{eff}\ddot{x} + m_\mathrm{eff}\Gamma\dot{x} + m_\mathrm{eff}\Omega_\mathrm{m}^2 x = F \tag{2.28}$$

where Γ is the linear damping rate and Ω_m is the angular resonance frequency of the mechanical mode. The effective mass of the resonator, m_eff, is mode-dependent and accounts for the extended nature of the mechanical resonator [97]. It is given by

$$m_\mathrm{eff} = \int dV\, \rho(\vec{r})|\vec{z}(\vec{r})|^2, \tag{2.29}$$

where $\rho(\vec{r})$ is the density of the material and $\vec{z}(\vec{r})$ is the displacement, or modeshape, of the resonator at each point $\vec{r}$ in space, normalized such that the maximum of $|\vec{z}(\vec{r})|$ has unit magnitude.

We can solve Equation (2.28) in the frequency domain by taking its Fourier transform, defined for a function $h(t)$ as

$$H(\omega) = \int_0^\infty e^{i\omega t} h(t) dt. \tag{2.30}$$

This gives

$$X(\omega)[-\omega^2 + i\omega\Gamma + \Omega_\mathrm{m}^2] = \frac{F(\omega)}{m_\mathrm{eff}}, \tag{2.31}$$

where $X(\omega)$ and $F(\omega)$ are the Fourier transforms of the position $x(t)$ and thermal force $F(t)$, respectively.

The single-sided PSD $S_{xx}(\omega)$ of the resonator's motion can be related to $X(\omega)$ by [97]

$$S_{xx}(\omega) = \lim_{\tau_\mathrm{m}\to\infty} \frac{1}{\tau_\mathrm{m}} |X(\omega)|^2, \tag{2.32}$$

so we can write Equation (2.31) in terms of the PSDs of the mechanical motion and the thermal forces. Noting also that because the thermal forces described by $F(t)$ are incoherent and therefore flat across the frequency range of interest, we can take $S_{FF}(\omega) = \lim_{\tau_\mathrm{m}\to\infty} \frac{1}{\tau_\mathrm{m}} |F(\omega)|^2 = S_{FF}^\mathrm{th}$ to be constant and

$$S_{xx}(\omega) = |\chi(\omega)|^2 S_{FF}^\mathrm{th}. \tag{2.33}$$

Here,

$$\chi(\omega) = \frac{1}{m_\mathrm{eff}[\Omega_\mathrm{m}^2 - \omega^2 - i\Gamma\omega]} \tag{2.34}$$

is the mechanical susceptibility which relates $S_{xx}(\omega)$ to the PSD of the applied force $S_{FF}(\omega)$. The constant S_{FF}^th can be determined from the equipartition theorem, which states that each quadratic degree of freedom carries an average energy of $\frac{1}{2}k_\mathrm{B}T$,

$$\frac{1}{2} m_\mathrm{eff} \langle x^2(t)\rangle \Omega_\mathrm{m}^2 = \frac{1}{2} k_\mathrm{B} T, \tag{2.35}$$

where T is the temperature of the mechanical mode. The root-mean-squared amplitude of the position, x_0, is defined by

$$x_0^2 = \langle x^2(t)\rangle = \frac{k_\mathrm{B} T}{m_\mathrm{eff}\Omega_\mathrm{m}^2}. \tag{2.36}$$

We can also calculate $\langle x^2(t)\rangle$ using Equation (2.26) with $t = 0$,

$$\langle x^2(t)\rangle = \frac{1}{\tau_\mathrm{m}}\int_0^{\tau_\mathrm{m}} dt'\,[x(t')]^2 = R_{xx}(0), \tag{2.37}$$

as long as the duration of the measurement τ_m is taken to be much longer than the period of oscillation of the mechanical mode ($2\pi\Omega_\mathrm{m}^{-1}$). Noting from Equation (2.27) that we can recover the autocorrelation function $R_{xx}(t)$ by taking the inverse Fourier transform of $P_{xx}(\omega)$ (or equivalently, of $S_{xx}(\omega)$) over the appropriate domain, we find that

$$R_{xx}(0) = \langle x^2(t)\rangle = \frac{1}{2\pi}\int_0^{\infty} d\omega\, S_{xx}(\omega). \tag{2.38}$$

Integrating Equation (2.33) and substituting the result into Equation (2.38) we find [97]

$$\langle x^2(t)\rangle = \frac{S_{FF}^\mathrm{th} Q_\mathrm{m}}{4\Omega_\mathrm{m}^3 m_\mathrm{eff}^2}. \tag{2.39}$$

Here we have introduced the mechanical quality factor $Q_\mathrm{m} = \Omega_\mathrm{m}/\Gamma$, valid in the high-$Q$ regime ($Q_\mathrm{m} \gg \frac{1}{2}$). Finally, equating Equations (2.36) and (2.39), we have

$$S_{FF}^\mathrm{th} = \frac{4k_\mathrm{B}Tm_\mathrm{eff}\Omega_\mathrm{m}}{Q_\mathrm{m}}, \tag{2.40}$$

and

$$S_{xx}(\omega) = \frac{4k_\mathrm{B}T\Omega_\mathrm{m}}{m_\mathrm{eff}Q_\mathrm{m}[(\Omega_\mathrm{m}^2-\omega^2)^2 + (\omega\Omega_\mathrm{m}/Q_\mathrm{m})^2]}. \tag{2.41}$$

Or, in terms of the natural frequency, f (resonance frequency f_m),

$$S_{xx}(f) = \frac{k_\mathrm{B}Tf_\mathrm{m}}{2\pi^3 m_\mathrm{eff}Q_\mathrm{m}[(f_\mathrm{m}^2-f^2)^2 + (ff_\mathrm{m}/Q_\mathrm{m})^2]}. \tag{2.42}$$

2.3.1.3 Calibration of a Voltage Signal

Of course, the signal used to measure the motion of the mechanical resonator does not appear exactly as in Equation (2.42). Instead, it consists of a voltage signal $V(t)$, for which a power spectral density, $S_{VV}(f)$ can be calculated, analogous to Equation (2.32). This signal usually contains some system-dependent noise, S_{VV}^NF which we assume is locally broadband in the region of the signal of interest, such that we can write

$$S_{VV}(f) = S_{VV}^\mathrm{NF} + \alpha S_{xx}(f). \tag{2.43}$$

Here, α is a detection-dependent scaling factor that describes how the motion of the resonator $x(t)$ is transduced into the voltage signal $V(t)$. For optomechanical detection, it will vary based on laser power, photodiode response and electronic gains as well as the coupling strength betweeen the optical resonance and the mechanical motion. If all other factors are known or calibrated, this optomechanical coupling can be inferred from the measured voltage spectrum $S_{VV}(f)$ [34, 85, 98].

In practice, we fit the spectrum $S_{VV}(f)$ with Equations (2.42) and (2.43), using S_{VV}^{NF}, Q_{m}, $A = \alpha k_{\mathrm{B}} T / 2\pi^3 m_{\mathrm{eff}}$ and f_{m} as the fit parameters. If we know the temperature and effective mass of the resonator, we can determine α and the displacement PSD. This is usually what is done in room temperature measurements, where the resonator is well-thermalized to its surroundings. However, if we don't know T, we could also determine its value using knowledge of α. This is the basis for the mechanical mode thermometry described in Section 4.3.3.

2.3.2 Mechanical Modes of Bottle Resonators

The mechanical modes of the bottle resonators studied in this thesis consist of a family of equatorial "breathing" and "squishing" modes, as shown in Figure 2.3. These modes are simulated using finite element modelling in COMSOL by constructing two sets of models, one which includes and the other which excludes the bottle stems. Realistic and detectable modes are identified as those which appear in both sets of simulations, have minimal displacements in the bottle stems (*i.e.*, aren't stem-modes) and which have large displacements near the equator since that is where the optical modes used to detect the mechanical motion are localized. These simulated modeshapes are used to calculate m_{eff}, as defined in Equation (2.29).

2.3.2.1 Sources of Mechanical Losses

The linewidth or damping rate $\Gamma = \Omega_{\mathrm{m}}/Q_{\mathrm{m}}$ of the mechanical resonator can also be interpreted as the rate at which phonons are lost from the resonator. There are several mechanisms through which this can happen, including viscous damping [99, 100], clamping losses [8] and intrinsic material losses. Viscous damping occurs as a result of mechanical motion being limited by the non-zero viscosity of the surrounding medium such as air or water. This tends to be eliminated in high-vacuum environments, but is not the limiting contribution to mechanical losses in the bottle resonators studied here (Ref. 100 sees just a four times increase in Q_{m} for toroidal breathing modes between ambient and vacuum pressures). Clamping losses occur when phonons tunnel out of the resonator through the

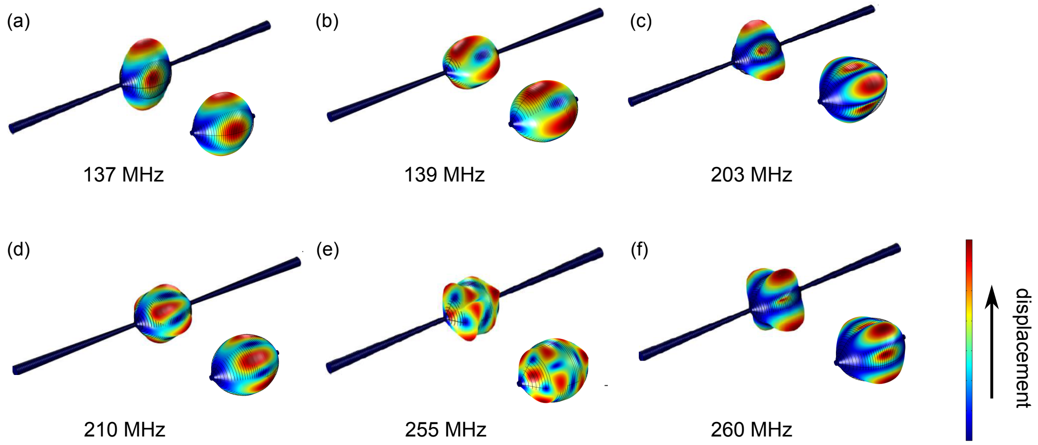

Figure 2.3: Mechanical modes and resonance frequencies of a 25 μm diameter bottle resonator with and without stems simulated using COMSOL.

clamping structure or substrate. We reduce the effects of clamping losses by fabricating bottles with thin stems [100]. Since the mechanical modes studied are generally concentrated around the equator of the bottle, far removed from the stems, it is not easy for phonons to travel from the mode volume to the outside stems. In the case of the bottles studied here, we believe the dominant sources of mechanical loss are internal, arising primarily from a distribution of two-level systems in the amorphous glass sample which permit phonon excitation across an asymmetric double-well potential [101, 102, 103].

2.4 The Optomechanical Interaction

Now that we have described optical and mechanical resonators separately, we quantitatively address the coupling between them. The canonical picture of an optomechanical resonator is shown in Figure 2.4, and consists of a Fabry-Pérot resonator in which one mirror is free to move. As the resonance frequency of the Fabry-Pérot cavity depends on its length, any motion of the free mirror modifies the optical resonance frequency. In turn, the optical field built up inside the cavity exerts a radiation pressure force on the mirror, driving its oscillations. In this section, we model the optomechanical interaction first through a Hamiltonian formalism and then with coupled equations of motion, which are used to describe dynamical backaction effects.

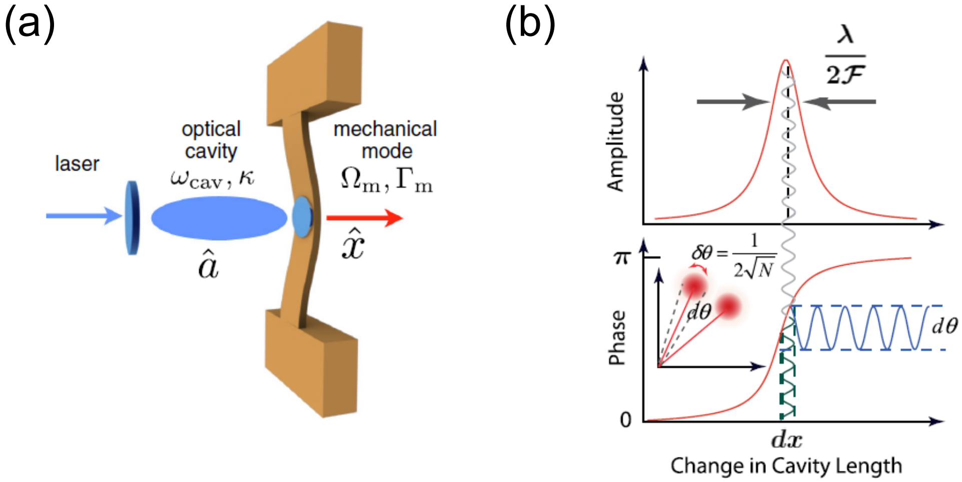

Figure 2.4: (a) Canonical picture of optomechanical coupling in a Fabry-Pérot resonator. (b) As the mechanical resonator moves, the optical resonance frequency is modulated, leading to an oscillating amplitude (top) and phase (bottom) of the intracavity light. Detection of the mechanical motion can be accomplished through either the phase or amplitude signal. Reprinted with permission from [M. Aspelmeyer, T. J. Kippenberg, and F. Marquardt. Cavity optomechanics. *Reviews of Modern Physics*, 86(4):1391–1452, 2014]. Copyright 2014 by the American Physical Society.

2.4.1 Hamiltonian Formulation

The Hamiltonian for independent optical and mechanical resonators can be written as

$$\hat{H} = \hbar\omega_{\mathrm{o}}\left(\hat{a}^{\dagger}\hat{a} + \frac{1}{2}\right) + \hbar\Omega_{\mathrm{m}}\left(\hat{b}^{\dagger}\hat{b} + \frac{1}{2}\right), \tag{2.44}$$

where $\hat{a}^{\dagger}, \hat{a}$ ($\hat{b}^{\dagger}, \hat{b}$) are the creation, annihilation operators for the optical (mechanical) mode, and ω_{o} (Ω_{m}) is the resonance frequency of the optical (mechanical) oscillator. The optomechanical interaction results in a position-dependent optical resonance frequency, which can be expanded as a Taylor series for small displacements. To first order, we have

$$\omega_{\mathrm{o}} \to \omega_{\mathrm{o}}(\hat{x}) \approx \omega_{\mathrm{o}} - G\hat{x} \tag{2.45}$$

where the linear optomechanical coupling strength is $G = -\frac{\partial \omega_{\mathrm{o}}}{\partial x}$. Nonlinear coupling can be accounted for by adding additional terms in the Taylor series [14, 85]. Inserting Equation (2.45) into Equation (2.44), we have

$$\hat{H} = \hbar(\omega_{\mathrm{o}} - G\hat{x})\hat{a}^{\dagger}\hat{a} + \hbar\Omega_{\mathrm{m}}\hat{b}^{\dagger}\hat{b} \tag{2.46}$$

where we have omitted the zero-point energy $\hbar\omega_{\mathrm{o}}/2$ and $\hbar\Omega_{\mathrm{m}}/2$ of each oscillator since they are static and negligible in the regimes of large photon and phonon numbers.

Transforming Equation (2.46) to a frame rotating at the drive laser frequency ω_{L}, we obtain [11, 104]

$$\hat{H} = -\hbar\Delta\hat{a}^{\dagger}\hat{a} - \hbar g_0(\hat{b} + \hat{b}^{\dagger})\hat{a}^{\dagger}\hat{a} + \hbar\Omega_{\mathrm{m}}\hat{b}^{\dagger}\hat{b}. \tag{2.47}$$

Here we have written the position operator $\hat{x} = x_{\mathrm{zpf}}(\hat{b} + \hat{b}^{\dagger})$ in terms of the amplitude of the mechanical mode's zero-point fluctuations

$$x_{\mathrm{zpf}} = \sqrt{\frac{\hbar}{2m_{\mathrm{eff}}\Omega_{\mathrm{m}}}} \tag{2.48}$$

and its creation and annihilation operators. This zero-point motion can be thought of as the spread in the mechanical oscillator's ground state wavefunction. We have also introduced the vacuum optomechanical coupling rate

$$g_0 = Gx_{\mathrm{zpf}}, \tag{2.49}$$

which represents the strength of optomechanical coupling that exists between a single photon and a single phonon. The effective mass, m_{eff}, is defined as in Equation (2.29).

By taking the derivative of the Hamiltonian in Equation (2.46) with respect to the position operator $\hat{x}$, we determine the radiation pressure force that the intracavity field exerts on the mechanical mode,

$$\hat{F}_{\text{rad}} = -\frac{\partial \hat{H}}{\partial \hat{x}} = \hbar G \hat{a}^\dagger \hat{a}. \tag{2.50}$$

This force in turn shifts the equilibrium of the mechanical oscillator's position from 0 to

$$\bar{x} = \langle \hat{x} \rangle = \frac{\langle \hat{F}_{\text{rad}} \rangle}{m_{\text{eff}} \Omega_{\text{m}}^2}. \tag{2.51}$$

This new equilibrium position of the mechanical resonator in turn results in a new static resonance frequency of the optical cavity $\omega_{\text{o}} \to \omega_{\text{o}}(\bar{x}) = \omega_{\text{o}} - G\bar{x}$.

2.4.2 Equations of Motion - Dynamical Backaction

Further insight into the dynamical effects of the interaction can be gained by studying the coupled optical and mechanical equations of motion. Since we deal exclusively with large numbers of both photons and phonons, we will consider only the classical equations of motion, taking $\hat{a} \to a$ and $\hat{x} \to x$. Unlike the Hamiltonian of the previous section, which assumes a closed system and thus conservation of energy, the equations of motion include both optical and mechanical decay mechanisms. These are analogous to Equations (2.17) and (2.28), but include the optomechanical interaction through a radiation pressure force, $\hbar G|a|^2$, and a position-dependent optical resonance frequency, $\omega_{\text{o}} - Gx$, in the mechanical and optical equations of motion, respectively. For an external driving force $F_{\text{ext}}(t)$, the resulting equations in the rotating picture are coupled,

$$m_{\text{eff}}\ddot{x} = -m_{\text{eff}}\Omega_{\text{m}}^2 x - m_{\text{eff}}\Gamma\dot{x} + \hbar G|a|^2 + F_{\text{ext}}(t) \tag{2.52}$$

$$\dot{a} = \left[i(\Delta + Gx) - \frac{\kappa}{2} \right] a + \sqrt{\kappa_{\text{ex}}} s_{\text{in}}. \tag{2.53}$$

We seek to solve the above system of equations by expanding both the intracavity field $a(t) = \bar{a} + \delta a(t)$ and the position $x(t) = \bar{x} + \delta x(t)$ around their respective equilibria and neglecting terms of $\mathcal{O}(\delta^2)$. The equations of motion thus become

$$\begin{aligned} m_{\mathrm{eff}}\ddot{\delta x} &= -m_{\mathrm{eff}}\Omega_{\mathrm{m}}^2\delta x - m_{\mathrm{eff}}\Gamma\dot{\delta x} + \hbar G(\bar{a}^*\delta a + \bar{a}\delta a^*) + F_{\mathrm{ext}}(t) && (2.54)\\ \dot{\delta a} &= i\left(\bar{\Delta} - \frac{\kappa}{2}\right)(\bar{a} + \delta a) + iG\bar{a}\delta x + \sqrt{\kappa_{\mathrm{ex}}}s_{\mathrm{in}}, && (2.55) \end{aligned}$$

where we have used Equation (2.51) to simplify Equation (2.54) and we have renormalized the laser detuning ($\Delta \to \bar{\Delta} = \Delta + G\bar{x}$) to include the static shift of the cavity resonance frequency due to the new equilibrium position of the mechanical resonator. Recalling the stationary state solution to the intracavity field for detuning Δ (Equation (2.19)) we can write

$$\dot{\delta a} = \left[i\bar{\Delta} - \frac{\kappa}{2}\right]\delta a + iG\bar{a}\delta x. \tag{2.56}$$

We now Fourier transform the equations of motion, keeping in mind the identity $\delta a^*(\omega) = (\delta a(-\omega))^*$:

$$\begin{aligned} i\omega\delta a(\omega) &= \left[i\bar{\Delta} - \frac{\kappa}{2}\right]\delta a(\omega) + iG\bar{a}\delta x(\omega) && (2.57)\\ -\omega^2 m_{\mathrm{eff}}\delta x(\omega) &= -m_{\mathrm{eff}}\Omega_{\mathrm{m}}^2\delta x(\omega) - i m_{\mathrm{eff}}\omega\Gamma\delta x(\omega) + \hbar G\left[\bar{a}(\delta a(\omega))^* + \bar{a}^*\delta a(\omega)\right] + F_{\mathrm{ext}}(\omega). && (2.58) \end{aligned}$$

We first solve Equation (2.57) for the function $\chi_{\mathrm{cav}}(\omega)$ which describes the cavity response to motion of the mechanical resonator, $\delta x(t)$,

$$\delta a(\omega) = iG\bar{a}\chi_{\mathrm{cav}}(\omega)\delta x(\omega) = \frac{iG\bar{a}}{i(\omega - \bar{\Delta}) + \kappa/2}\delta x(\omega). \tag{2.59}$$

We can now use this to solve Equation (2.58) to obtain the mechanical response to the external driving force $F_{\mathrm{ext}}(\omega)$:

$$\begin{aligned} \delta x(\omega) &= \chi_{\mathrm{OM}}(\omega)F_{\mathrm{ext}}(\omega) && (2.60)\\ &= \frac{F_{\mathrm{ext}}(\omega)}{m_{\mathrm{eff}}(\Omega_{\mathrm{m}}^2 - \omega^2 - i\omega\Gamma) + \Sigma(\omega)}, && (2.61) \end{aligned}$$

where $\chi_{\mathrm{OM}}(\omega)$ is the mechanical susceptibility to $F_{\mathrm{ext}}(\omega)$ in the presence of the optomechanical interaction [104]. It is similar to Equation (2.34), with the addition of an optomechanical contribution $\Sigma(\omega)$, given by

$$\Sigma(\omega) = -i\hbar G^2|\bar{a}|^2 \left(\chi_{\mathrm{cav}}(\omega) - \chi^*_{\mathrm{cav}}(-\omega)\right). \tag{2.62}$$

If we compare the above result to Equation (2.34), we infer that the imaginary part of the complex susceptibility describes the damping of mechanical oscillations while the real part describes the frequency. Examining Equation (2.61), evaluated near the bare mechanical resonance frequency Ω_{m}, we see that both the resonance frequency and the mechanical damping rate are modified by the optomechanical interaction according to

$$\delta(\Omega_{\mathrm{m}}^2) = 2g^2\Omega_{\mathrm{m}} \left\{ \frac{\Omega_{\mathrm{m}} + \bar{\Delta}}{(\Omega_{\mathrm{m}} + \bar{\Delta})^2 + \kappa^2/4} - \frac{\Omega_{\mathrm{m}} - \bar{\Delta}}{(\Omega_{\mathrm{m}} - \bar{\Delta})^2 + \kappa^2/4} \right\} \tag{2.63}$$

and

$$\Gamma_{\mathrm{OM}} = g^2\kappa \left\{ \frac{1}{(\Omega_{\mathrm{m}} + \bar{\Delta})^2 + \kappa^2/4} - \frac{1}{(\Omega_{\mathrm{m}} - \bar{\Delta})^2 + \kappa^2/4} \right\}. \tag{2.64}$$

Here, $g = \bar{a}g_0$ is the field-enhanced optomechanical coupling rate. Equation (2.63) describes a light-induced frequency shift while Equation (2.64) describes the optomechanical contribution Γ_{OM} to the mechanical damping such that the total damping rate is given by $\Gamma_T = \Gamma + \Gamma_{\mathrm{OM}}$. Γ_{OM} can take on both positive and negative values depending on the detuning of the laser from the cavity resonance. A red detuned laser ($\bar{\Delta} = \omega_{\mathrm{L}} - \omega_{\mathrm{o}}(\bar{x}) < 0$) results in a positive optomechanical damping, effectively cooling the mode and increasing the total mechanical linewidth. In a quantum mechanical picture, this occurs because Raman scattering processes in which a photon scatters from a phonon to increase in energy are resonantly enhanced, reducing the number of phonons in the mechanical mode.

In the case of blue laser detuning ($\bar{\Delta} > 0$), the opposite is true. The optomechanical damping becomes negative and therefore reduces the mechanical linewidth, heating or amplifying the motion. If the total mechanical linewidth ($\Gamma_{\mathrm{OM}} + \Gamma$) is reduced to 0, there exists an optomechanical instability and a nonlinear treatment of the dynamics is necessary [11]. This parameter regime can be exploited to generate self-sustained oscillations [105, 106] and synchronization of multiple oscillators [107].

Note that for a laser which is resonant with the optical cavity, $\bar{\Delta} = 0$, Equations (2.63) and (2.64) are zero and the mechanical damping rate and resonance frequency are left unchanged. Thus a measurement of the mechanics made on-resonance exerts no dynamical backaction on the mechanical resonator (although it may still impart a static backaction which shifts the equilibrium position due to the radiation pressure force exerted by the photons in the cavity).

It is also worth noting that the equations above (*i.e.*, linearized) are not sufficient approximations for devices in the strong coupling regime ($g > \kappa$) [11]. There, the small terms proportional to $\delta x \delta a$ become important and cannot be neglected. In these cases, the optical spring effect and optomechanical damping terms lead to first a non-Lorentzian lineshape and eventually a normal mode splitting of the mechanical resonance into two hybridized modes [13, 108].

2.4.3 Optomechanical Coupling in WGM Resonators

Optomechanical coupling in WGM resonators can occur through overlap of the evanescent field of the WGM with a mechanical element, such as in the case of microdisks, toroids or microspheres coupled via the evanescent field to cantilevers, strings, or membranes [21, 22, 109]. In these configurations, the optomechanical coupling occurs as the motion of the mechanical element causes a change in the effective refractive index of the optical mode. Optomechanical coupling is also commonly observed in systems such as microspheres [39], disks [41] and toroids [110] which exhibit radial breathing modes. In these cases, the mechanical mode occupies the same (or nearly the same) volume as the optical mode, such that the mechanical motion causes a change in the boundary conditions of the material, thus modulating the optical resonance frequency.

For the case of a microsphere (or nearly-spherical bottle resonator) interacting with a radial breathing mode, the optomechanical coupling strength can be derived quite simply by considering the resonator as a Fabry-Pérot resonator with periodic boundary conditions. The Fabry-Pérot has resonance frequencies which are given by the condition

$$\omega_l = \frac{l\pi c}{L}, \tag{2.65}$$

where l is the mode label and L is the length of the cavity. Similarly, a spherical WGM resonator has the resonance condition (as in Equation (2.12))

$$\omega_l = \frac{lc}{n_0 c_1 R}, \tag{2.66}$$

where R is the radius of the WGM resonator. If we now consider small changes to the radius $R \to R + r$, where $r \ll R$, such as would occur in a radial breathing mode, we find

$$\omega_l(r) = \frac{lc}{n_0 c_1 (R + r)} \simeq \omega_l \left(1 - \frac{r}{R}\right). \tag{2.67}$$

Defining the optomechanical coupling as $G = -\frac{\partial \omega_l}{\partial r}$ results in a relatively simple expression for the optomechanical coupling strength,

$$G = \frac{\omega_l}{R}. \tag{2.68}$$

2.5 Low Temperature Optomechanics

Optomechanical devices are interesting systems not only for practical applications but also for fundamental tests of the validity of quantum mechanics on large scales. The sensitivity of optomechanical devices makes them ideally suited to study this quantum-to-classical crossover, and the observation of the quantum mechanical ground state of a mesoscopic object is the subject of significant efforts [4, 16, 46, 111, 112].

Furthermore, the hybrid nature of these systems makes them appealing candidates for many quantum information processing architectures. Photons are promising information carriers for their speed and limited decoherence. However, the difficulty in coupling photons to one another makes other quantum systems, such as spins or superconducting circuits more favourable as qubit implementations. Optomechanical devices are perhaps uniquely suited as transducers between a wide variety of qubit systems and optical photons which could act as flying qubits to mediate information transfer between distant qubit systems [30].

A central requirement to the above experiments is preparation of the mechanical resonator in, or very near, its ground state [33]. Most micro- and nano-mechanical resonators operate at frequencies ranging from kHz to GHz, such that they are subject to significant thermal occupation at room temperature. The average phonon occupation for a resonator of frequency Ω_m in thermal equilibrium with a bath of temperature T is given by

$$\bar{n} = \frac{1}{e^{\hbar\Omega_\mathrm{m}/k_\mathrm{B}T} - 1}, \tag{2.69}$$

which for $\bar{n} \gg 1$ can be approximated by $\bar{n} \approx \frac{k_\mathrm{B}T}{\hbar\Omega_\mathrm{m}}$. Even at a temperature of 10 mK, attainable in a commercial dilution refrigerator, only mechanical resonators with $\Omega_\mathrm{m}/2\pi \gtrsim$ 150 MHz can be passively cooled into their ground states. This necessitates the use of active cooling processes to reach the ground state of most devices.

2.5.1 Optomechanical Cooling

A technique similar to laser cooling of atoms can be used as a non-equilibrium process to cool mechanical resonators into their ground states [11, 19, 20, 112]. Returning to Equation

(2.64), we see that it has two terms, each of which is clearly enhanced in turn for laser detunings $\bar{\Delta} = \pm\Omega_{\mathrm{m}}$. These two terms can be thought of in an equivalent picture as arising from scattering of photons in the laser drive field from the motion of the mechanical resonator. This scattering gives rise to motional sidebands in the spectrum of the optical cavity, as measured in [17, 20, 93]. Tuning the laser to either motional sideband ($\bar{\Delta} = \pm\Omega_{\mathrm{m}}$) resonantly enhances either the Stokes or anti-Stokes scattering process due to the large density of photon states in the optical cavity, as illustrated in Figure 2.5. For red-detuned beams, the anti-Stokes process is enhanced, where a drive photon absorbs a phonon from the mechanical resonator and increases in energy to be resonant with the optical cavity. A blue-detuned laser drive results in Stokes scattering, where the laser photon loses energy in the form of a phonon in order to scatter into the optical cavity.

These scattering processes can be exploited to either amplify ($\bar{\Delta} > 0$) the motion by adding phonons to the resonator or to cool ($\bar{\Delta} < 0$) the mechanical resonator by removing phonons. We can analyze how efficient this cooling is by studying the rates of these Stokes and anti-Stokes scattering processes. Let us denote A^{+} (A^{-}) as the Stokes (anti-Stokes) scattering amplitude. The Stokes process takes the resonator from the n phonon state to the $n+1$ phonon state so the rate of phonons being injected into the mechanical mode is [11, 104]

$$\Gamma_{n\to n+1} = (n+1)A^{+} \tag{2.70}$$

while the anti-Stokes scattering process results in a rate

$$\Gamma_{n\to n-1} = nA^{-}. \tag{2.71}$$

The total cooling rate is then given by [11, 104]

$$\Gamma_{\mathrm{OM}} = A^{-} - A^{+}. \tag{2.72}$$

While these Stokes and anti-Stokes scattering processes are occurring, the mechanical resonator is also in contact with a thermal bath, which has an average phonon occupation $\bar{n}_{\mathrm{th}}$ and exchanges phonons with the mechanical mode at the mechanical damping rate Γ. The average occupation of the mechanical resonator is given by the weighted sum of the Fock state populations P_n as $\bar{n} = \Sigma_{n=0}^{\infty} nP_n$, and the change in this average occupation is determined by both Stokes and thermal processes,

$$\dot{\bar{n}} = (\bar{n}+1)(A^{+} + A^{+}_{\mathrm{th}}) - \bar{n}(A^{-} + A^{-}_{\mathrm{th}}), \tag{2.73}$$

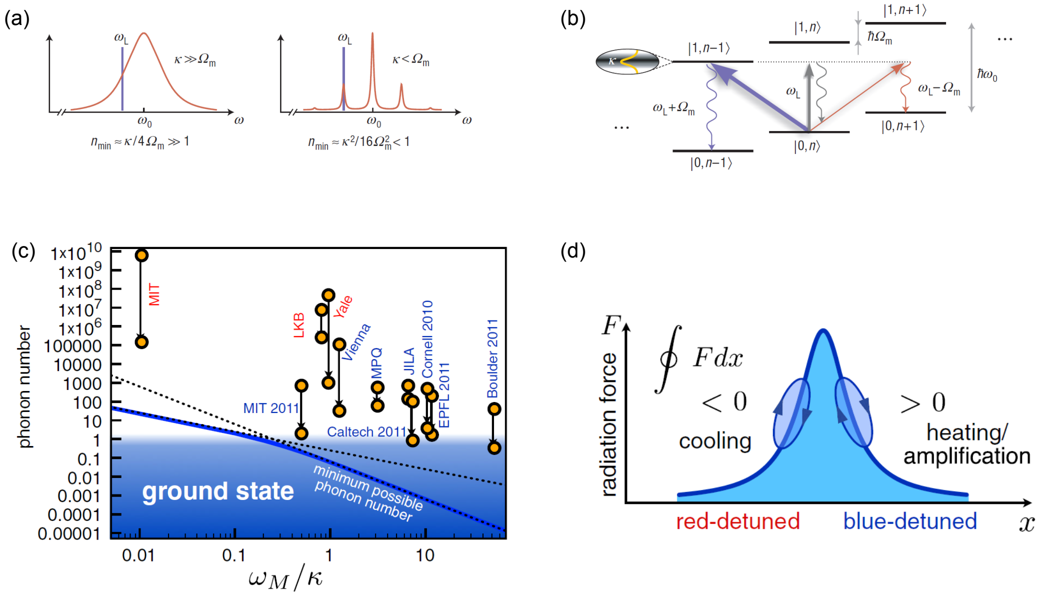

Figure 2.5: (a) Schematic depicting optomechanical cooling in the Doppler (left) and resolved sideband (right) regimes. Motional sidebands arising from scattering of photons from mechanical phonons are visible in the resolved sideband case. (b) Schematic of the optomechanical heating and cooling processes illustrated in terms of the addition and subtraction of phonons from the mechanical mode. (c) Experiments exhibiting laser cooling of optomechanical devices. (d) Work done by the radiation pressure force during one mechanical cycle. The presence of the cavity leads to a retardation of the radiation pressure relative to the mechanical motion, which in turn leads to heating or cooling of the mechanics. (a) and (b) reprinted by permission from Macmillan Publishers Ltd: Nature Physics [A. Schliesser, R. Rivière, G. Anetsberger, O. Arcizet, and T. J. Kippenberg. Resolved-sideband cooling of a micromechanical oscillator. *Nature Physics*, 4(5):415–419, 2008], copyright 2008. (c) and (d) reprinted with permission from [M. Aspelmeyer, T. J. Kippenberg, and F. Marquardt. Cavity optomechanics. *Reviews of Modern Physics*, 86(4):1391–1452, 2014]. Copyright 2014 by the American Physical Society.

where the thermal phonon exchange amplitudes are given by $A^{-}_{\mathrm{th}} = \bar{n}_{\mathrm{th}}\Gamma$ and $A^{+}_{\mathrm{th}} = (\bar{n}_{\mathrm{th}} + 1)\Gamma$. Solving for the steady state phonon occupation ($\dot{\bar{n}} = 0$) gives a final occupation $\bar{n}_f$ of

$$\bar{n}_f = \frac{A^{+} + \bar{n}_{\mathrm{th}}\Gamma}{\Gamma_{\mathrm{OM}} + \Gamma}. \tag{2.74}$$

If we now assume that the mechanical resonator is completely isolated from its thermal bath (in other words, we have a mechanical resonator with infintely high Q_{m}), then $\Gamma = 0$ and we can determine the theoretical absolute minimum phonon occupation,

$$\bar{n}_{\mathrm{min}} = A^{+}/\Gamma_{\mathrm{OM}}. \tag{2.75}$$

Substituting this into Equation (2.74) we obtain

$$\bar{n}_f = \frac{\bar{n}_{\mathrm{min}}\Gamma_{\mathrm{OM}} + \bar{n}_{\mathrm{th}}\Gamma}{\Gamma_{\mathrm{OM}} + \Gamma}. \tag{2.76}$$

The scattering rates A^{+} and A^{-} can be determined using Fermi's Golden Rule or quantum noise spectra [113], which in turn determine $\bar{n}_{\mathrm{min}}$ [11]. For the resolved-sideband regime ($\Omega_{\mathrm{m}} \gg \kappa$), this results in

$$\bar{n}_{\mathrm{min}} = \left(\frac{\kappa}{4\Omega_{\mathrm{m}}}\right)^2 \ll 1. \tag{2.77}$$

Thus, the level of sideband resolution dictates the theoretical limit for ground-state cooling. Note that the minimum occupancy $\bar{n}_{\mathrm{min}}$ is independent of the optomechanical coupling strength g_0 and the laser power. These factors do play a role in how close we can get to reaching this theoretical limit, through the optomechanical damping rate Γ_{OM} which is maximized for a laser detuning of $\bar{\Delta} = -\Omega_{\mathrm{m}}$. The corresponding cooling rate is

$$\Gamma_{\mathrm{OM}} = 4\frac{g^2}{\kappa}, \tag{2.78}$$

which does depend on the optomechanical coupling strength and input optical power.

For optomechanical devices in the Doppler regime ($\kappa \gg \Omega_{\mathrm{m}}$), this limit is given by

$$\bar{n}_{\mathrm{min}} = \frac{\kappa}{4\Omega_{\mathrm{m}}} \gg 1 \tag{2.79}$$

for a detuning of $\bar{\Delta} = -\kappa/2$. The corresponding cooling rate is given by

$$\Gamma_{\mathrm{OM}} = 8\Omega_{\mathrm{m}} \left(\frac{g}{\kappa}\right)^2 , \tag{2.80}$$

which we note is not the maximum cooling rate (which occurs at $\bar{\Delta} = -\kappa/2\sqrt{3}$) [11]. It is thus impossible to cool an optomechanical device in the Doppler regime to its ground state in this way, although there has been some success in reducing the phonon occupation in this regime [114, 115]. One interpretation of this fundamental limit is that the optical decay time of κ implies an energy uncertainty of $\Delta E \sim \hbar\kappa$ - much larger than the ground state energy $\hbar\Omega_{\mathrm{m}}/2$ [20]. Since the average energy of the system cannot be smaller than its uncertainty, it is not possible to cool to the ground state with this method. Ground-state cooling for these devices is, however, possible using other techniques such as pulsed cooling [116, 117] or in dissipatively-coupled optomechanical systems (in which $\kappa \rightarrow \kappa(x)$) [118]. Figure 2.5(c) illustrates a number of optomechanical cooling experiments.

Optomechanical cooling can also be understood by examining the phase diagram traced out by the motion of the mechanical resonator in the radiation pressure force versus x space, as shown in Figure 2.5(d). As the position of the mechanical resonator changes, so too does the resonance frequency of the cavity. The existence of the optical cavity leads to a retardation of the radiation pressure force acting on the mechanical resonator relative to the motion of the resonator. This in turn means that the radiation pressure force sweeps out an area (instead of a line) over the course of a mechanical period and thus does work on the oscillator. Whether energy is extracted or added to the mechanical resonator is dependent on the detuning of the laser. In the Doppler regime, the cooling power is small, since the relative timescales of the optics and mechanics mean that the intracavity field responds nearly instantaneously (on the timescale of a mechanical period) to changes in x. There is, however, still a slight retardation of the radiation pressure force, as seen in Equation (2.64) so that some cooling or heating is possible. In the resolved-sideband regime, intracavity photons are long-lived, resulting in a large retardation of the radiation pressure force and the potential for strong cooling or heating of the mechanics.

Note that although laser cooling is necessary to reach the mechanical ground state of many optomechanical systems, Equation (2.76) shows that passive cryogenic precooling is still a requirement, due to the coupling of the resonator to the thermal bath. This passive precooling can be accomplished by a number of techniques including dilution refrigeration [16, 46, 47] and exchange gas cooling in helium flow cryostats [19, 44, 45]. Cryogenic cooling is further advantageous in that it does not increase the total damping rate of the mechanical resonator, which lowers Q_{m} and can make observing small mechanical oscillations on a (relatively) large background very difficult. Finally, optomechanical systems could be used to sensitively probe interesting phenomena such as superconductivity and superfluidity [80, 119] which manifest themselves only at low temperatures.

CHAPTER 3

Experimental Methods and Dilution Fridge Apparatus

There are several key components that must first be developed in order to study the optomechanical interaction in silica bottle resonators at low temperatures. The first is fabricating both the tapered optical fiber used to couple light into the resonator (Section 3.1) as well as the resonator itself (Section 3.2). Secondly, we must have an apparatus that houses the taper and resonator, and enables their manipulation. At room temperature (Section 3.3), this is fairly straightforward and we use the same apparatus as described elsewhere [86, 87]. However, inside a dilution fridge, significant consideration must be given to space constraints, thermal anchoring and accessibility (Section 3.4). Another important consideration is the ability to align the optomechanical resonator and tapered fiber relative to each other. Our apparatus addresses this challenge with a home-built optical microscope that allows *in situ* imaging of the taper and resonator (Section 3.4.3). Finally, a suitable arrangement of optics and electronics is required to detect the small signal of the optomechanical interaction (Section 3.5).

3.1 Tapered Fiber Fabrication

Tapered optical fibers are fabricated using a heat-and-pull method [86, 120, 121]. A Corning SMF-28e single mode optical fiber is mechanically stripped of its acryllic coating in a small region (3-4 cm) and cleaned with acetone. It is then clamped into two Newport 466A-710 double-armed V-groove fiber clamps which are mounted on a two-dimensional Zaber stage positioner. The ends of the fiber are cleaved and mechanically spliced to a pair of patch cables (also Corning SMF-28e fiber), which are connected to a 1550 nm laser and a photodiode so that transmission of light through the fiber can be monitored during the pulling process. The pulling apparatus is pictured in Figure 3.1.

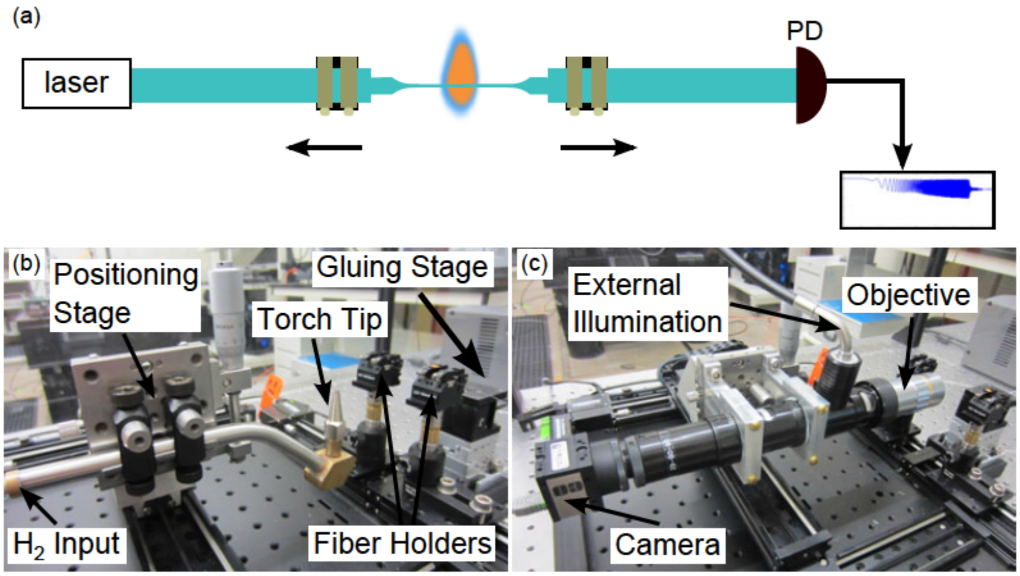

Figure 3.1: (a) Schematic of the taper-pulling process, in which an optical fiber is heated and stretched while monitoring its transmission with a photodiode (PD) (shown in more detail in Figure 3.2). (b) The taper-pulling apparatus, with optical microscope configuration shown in (c). (b-c) adapted from [B. D. Hauer, P. H. Kim, C. Doolin, A. J. R. MacDonald, H. Ramp, and J. P. Davis. On-chip cavity optomechanical coupling. *EPJ Techniques and Instrumentation*, 1:4, 2014] under the Creative Commons Attribution License.

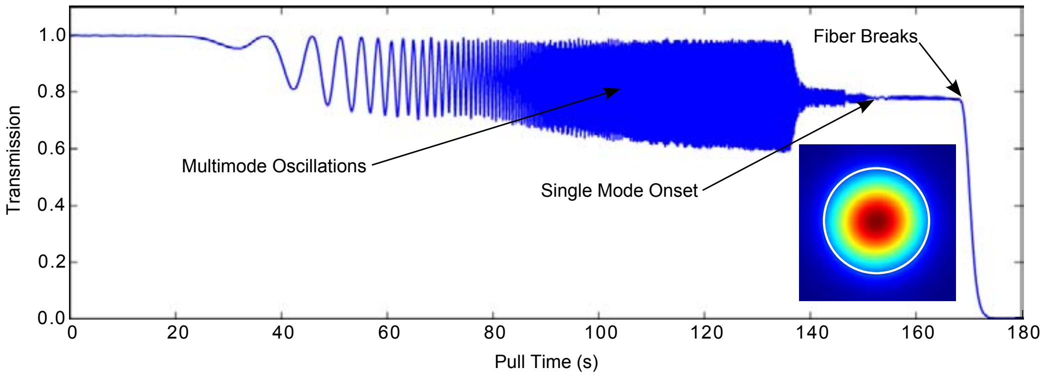

Figure 3.2: Observed transmission during pulling of a single mode tapered fiber. Inset: energy density of the electric field in the taper mode. White circle denotes the boundary of the core. Figure reproduced from [B. D. Hauer, P. H. Kim, C. Doolin, A. J. R. MacDonald, H. Ramp, and J. P. Davis. On-chip cavity optomechanical coupling. *EPJ Techniques and Instrumentation*, 1:4, 2014] under the Creative Commons Attribution License.

A hydrogen torch is used to produce a small, stable flame and the Zaber stages are used to approach the flame to the stripped region of the fiber. The flame is positioned to obtain the largest hot zone (determined by the width of the glowing region on the stripped fiber) and a stable flame as a uniform heating profile increases the adiabaticity and minimizes losses in the taper [86, 88]. This usually means that the flame is positioned so that the fiber is near the bottom of the flame.

Once the flame is positioned, the fiber clamps (mounted on the computer-controlled Zaber stages) move apart at a constant speed of 40 μm/s, stretching the fiber as it is heated. By conservation of volume, the diameter of the fiber is reduced as the core and cladding are melted together and the fiber ceases to be single mode. The changing diameter of the fiber gives rise to parasitic modes which have a fiber dimension-dependent loss. This takes the form of regular oscillations in the transmission as a function of time, as shown in Figure 3.2. The frequency of these oscillations increases as the pulling proceeds until the point that they cease altogether. At this point, all parasitic modes have died off and the tapered region of the fiber consists of a glass core of $\sim$1 μm diameter clad by air. The taper is a single mode fiber, but with a large portion of the guided mode propagating in the evanescent field in the air outside the core.

The entire tapering procedure occurs inside a closed acrylic box situated on an optical table. Since the cleanliness of both the fiber and the environment are very important to the overall quality of the final taper [122], the box serves to protect the taper from airborne contaminants such as dust. It additionally reduces the effects of air currents that introduce

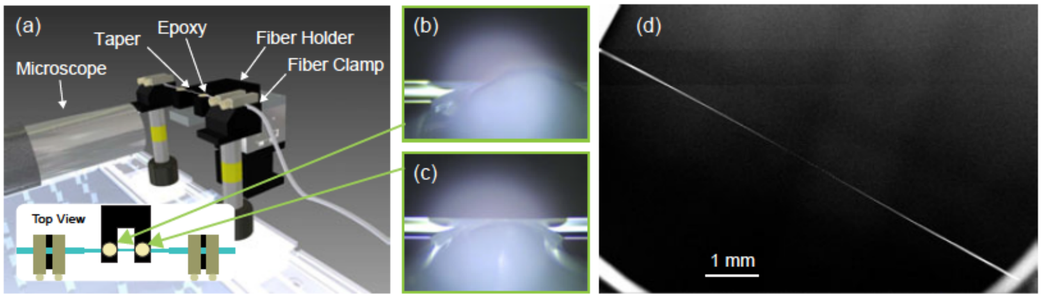

Figure 3.3: (a) Schematic of the room-temperature taper-gluing process, with photographs of the initial gluing points shown in (b) and (c). (d) Scanning electron microscope image of a mounted tapered fiber, with a 1.2 μm minimum diameter. (a-c) adapted from [B. D. Hauer, P. H. Kim, C. Doolin, A. J. R. MacDonald, H. Ramp, and J. P. Davis. On-chip cavity optomechanical coupling. *EPJ Techniques and Instrumentation*, 1:4, 2014] under the Creative Commons Attribution License.

turbulence to the flame, destroying the uniformity of the heating profile and resulting in non-adiabatic tapering. This procedure results in tapers with losses (from start to end of the pull) as low as 1%.

After a successful taper is produced, an optical microscope is mounted to the tapering apparatus, as shown in Figure 3.1(c), and used to view the taper. Immediately following the pull, the thinnest region of the taper usually has a small bump in its centre, arising from the upward flow of hydrogen gas during the pulling procedure. We tension the fiber, moving the fiber clamps apart in 5 μm steps, until it is once again straight or until the transmission begins to drop. We then glue the taper to a homemade aluminum fork-shaped fiber holder with Devcon 14240 five-minute epoxy. We place a small drop of glue on each side of the fiber holder, place the fiber holder under the taper and then raise it until contact is made between the glue and the untapered regions of the fiber. The fiber holder is positioned in three dimensions using the stack of translational positioners (gluing stage) shown in Figure 3.1(b). The glue is then allowed to set for about half an hour before more glue is applied by draping thin strings perpendicular to the fiber, strengthening the bond between the glued region of the fiber and the mount.

After gluing, the taper is gently moved out of the acrylic box and into the coupling chamber where it is fusion spliced to two lengths of fiber installed inside the chamber. The fiber holder itself is flipped upside down and mounted to a stationary block such that the taper is lower than its holder. This facilitates access of the taper to an optical resonator situated below it.

3.2 Bottle Fabrication

Bottle resonators [48, 49, 50, 51, 123, 124] are WGM resonators similar to microspheres, but can range in shape from parabolic as in Ref. 49 to nearly spherical [52], as in this work. The fiber stems on either side enable the introduction of a mehcanical strain to the bottle, allowing tuning of the optical resonances over a full free spectral range [49, 52]. The high optical quality factors of the bottle modes, high mechanical frequencies and transparency to many wavelengths make the bottles interesting candidates in pulse storage [39, 125] and wavelength conversion [42] applications. Bottle resonators are also of interest in creating all-optical switches and add-drop filters [123, 124], as well as in optofluidic sensing [50, 51].

We fabricate our bottle resonators by heating SMF-28e silica fibers using a commercial CO_2 laser (Synrad 48-2KAM). The glass absorbs photons of $\sim$10 μm wavelength and is heated in proportion to the beam intensity and the diameter of the fiber. A short piece ($\sim$5 cm) of SMF-28e fiber is stripped of its coating and clamped in the fiber clamps in the fiber pulling setup described above (shown in Figures 3.1 and 3.4). A CO_2 laser is then focused to an $\sim$25 μm spot by a 25.4 mm focal-length ZnSe lens. The lens and a 45° mirror are cage-mounted to the Zaber stages, as shown in Figure 3.4. A red guiding laser is used to align the optics, including two steering mirrors, so that the laser spot is focused on the centre of the clamped and stripped fiber.

The CO_2 laser is then turned on and the power increased until a bright white spot is visible at the centre of the stripped fiber, which usually occurs at an incident power of 2-3 W when the apparatus is properly aligned. The Zaber stages pull the fiber apart at a constant speed of 40 μm/s while the laser spot is translated back and forth across a 5 mm section of the fiber at a maximum speed of 5 mm/s. As the pulling proceeds, the laser power is increased (to a maximum of 16 W) so that the white spot remains visible even as the fiber is stretched and made thinner. As the fiber is melted and stretched, the scanning laser creates areas of local heating which make the fiber look bumpy with smooth transitions between areas of large and small fiber diameters, as depicted in Figure 3.4(c). Towards the end of the pulling procedure, these spots of local heating are perceived as areas of the fiber where the laser spot is brighter. These spots eventually become bottle resonators which give off very bright flashes as the laser spot traverses them. By continuing to heat and pull for a short time after these flashes appear, we can continue to melt and stretch the fiber connecting the bottles so that it becomes thinner, weakening the bottles' connection to each other and increasing their mechanical quality factors. The pulling motion of the Zaber stages and the power to the CO_2 laser are stopped simultaneously as pulling without heating will break the fiber, whereas the focussed laser spot will burn through the fiber if left in one place for too long. This results in an observed success rate of <10%. By using a brighter (more powerful) laser

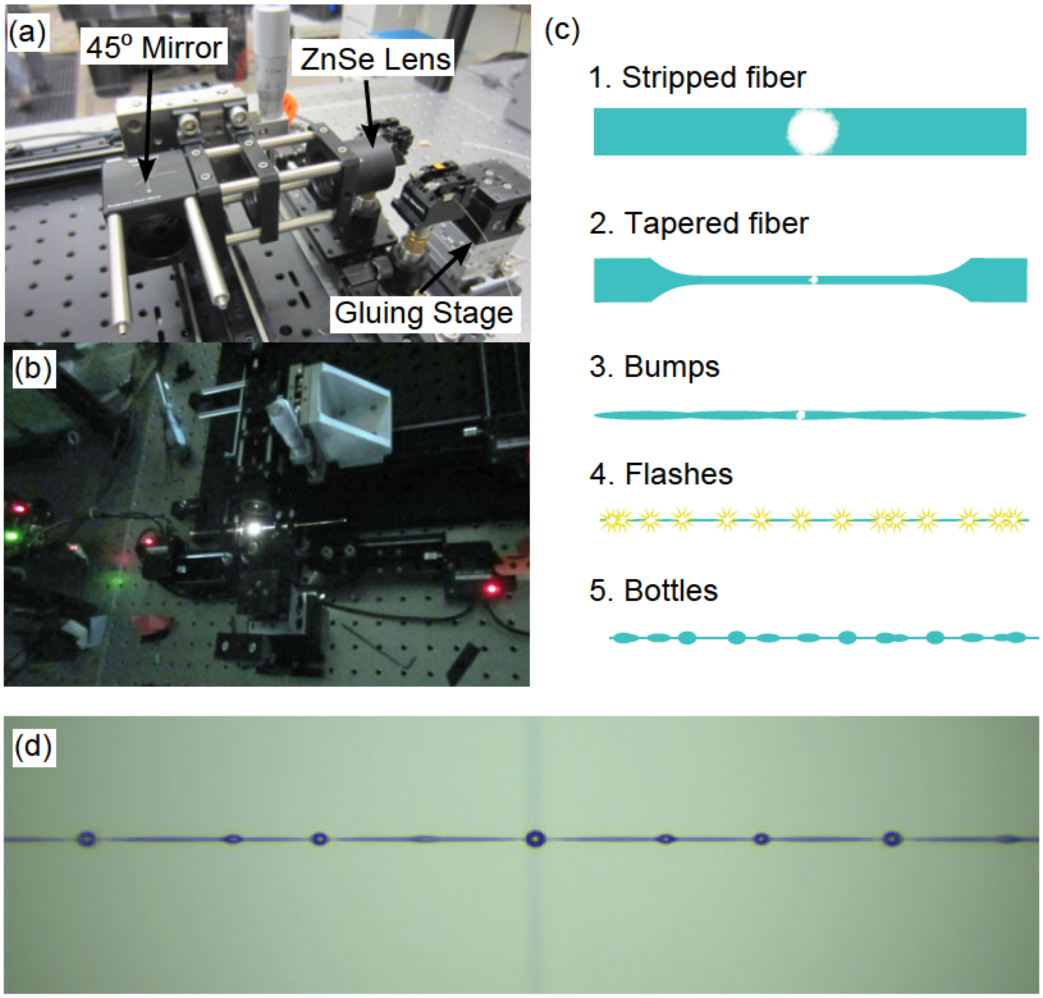

Figure 3.4: (a) The bottle fabrication apparatus. (b) The location of the CO_2 laser spot as it melts the fiber is observed as a bright white spot. (c) Schematic of changes that occur to the fiber during the bottle-pulling process. (d) optical photograph of a string of bottles, with tapered fiber (defocussed line perpendicular to the string) visible in the background. (a) adapted from [B. D. Hauer, P. H. Kim, C. Doolin, A. J. R. MacDonald, H. Ramp, and J. P. Davis. On-chip cavity optomechanical coupling. *EPJ Techniques and Instrumentation*, 1:4, 2014] under the Creative Commons Attribution License.

spot throughout the entire procedure, larger bottles (diameters >50 μm) can be created. For the resonators studied in this thesis, we have continued pulling the fiber to very close to the point of breaking and have obtained bottles of varying dimensions (diameters $\sim$20-50 μm) and shapes.

Once a set of bottles is pulled, the microscope is mounted as shown in Figure 3.1 to examine the bottles. The bottle pulling procedure generally results in a string of many ($\sim$50-75) bottles (as seen in Figure 3.4(d)), most of which are not suitable for optomechanics experiments. We choose bottles which have a relatively large diameter (>20 μm), thin connecting stems and a symmetric profile. We generally choose spheroidally-shaped bottles for optomechanics as they have the thinnest connecting stems. Thin connecting stems constrain the bottle's motion less, and result in higher quality mechanical breathing modes. The process used to create these spheroidal bottles often results in many other bottle shapes, including double-bottles, in which two bottles look fused together or barely separated, and asymmetric-stemmed bottles, where one stem is much thicker than the other. We keep a string of bottles if it has 3-4 spheroidal, thin-stemmed bottles on it.

The bottle string is tensioned and glued to either side of a small (6 mm) channel in a bottle mount (room temperature mount shown in the inset of Figure 3.5) using the same process as for the tapered fibers. The bottles are very delicate at this stage and tensioning even a small amount may break the bottle string, while insufficient tension introduces difficulties in coupling the bottle to a tapered fiber without contacting the taper and degrading the mechanical motion. We determine if any additional tension is required by gently blowing on the bottle string and watching the resulting motion with the optical microscope. If the bottles return to their position almost immediately, no additional tension is necessary. By contrast, if the bottles show large vibrations we tension them until this vibration disappears.

3.2.1 Larger Bottles

Much larger bottles (diameters of $\sim$200 μm) can be fabricated with a fusion splicer. In this scenario, the centre of a fiber is melted and broken into two using the arc from the electrodes in a fusion splicer. This forms a small microsphere on each end. The two microspheres are then fused together in the fusion splicer by pushing together the fibers and heating the centre of the microspheres. The resulting structure is re-fused several times until a symmetric bottle is formed. Bottles fabricated in this way are much less fragile than those made with the CO_2 laser due to their large fiber handles and thus can simply be taped to the bottle mount. We have used these bottles as test optical resonators but have not been able to observe any mechanical resonances, likely due to their large stems which lead to increased clamping losses.

3.3 Room Temperature Coupling Chamber

Once a suitable sample and tapered fiber have been fabricated, they are installed in a dedicated room temperature, vacuum-compatible coupling chamber. The chamber, shown in Figure 3.5, is home-built and described in more detail in Ref. 86 and Ref. 87. The top of the chamber includes a glass window that allows imaging of the taper and bottle with an optical microscope, consisting of a 10× objective and a zoom barrel enabling a further 7× magnification. The base of the vacuum chamber contains several input/output ports for a pumping station, electrical leads to control positioning stages and fiber optic feedthroughs to connect the tapered fiber to the outside optics, including a laser and detector. Before sealing the fiber optic feedthroughs, two long lengths of fiber are fed into the chamber. Each time a new tapered fiber is installed in the chamber, it is fusion-spliced to these lengths of fiber. Outside the chamber, the fibers are fusion-spliced to patch cables, facilitating connections to the controlling optics.

The tapered fiber is mounted in the chamber by flipping the fork-shaped fiber holder upside-down and securing it to a stationary aluminum support. To minimize vibrations of the fiber which can cause noise in the desired signal as well as to protect the fiber, it is secured with vacuum-compatible Kapton tape in a number of places inside the chamber. The bottle holder is mounted to the side of a set of three Agilis (AG-LS25V6) linear nanopositioning stages, as shown in Figure 3.5(b-c). These stages offer full three-dimensional control over the position of the bottles and have a resolution of 50 nm over a total travel range of 12 mm. The choice to leave the fiber stationary while moving the bottles underneath is made to minimize low frequency vibrations of the fiber and enable compatibility with on-chip coupling as described in Ref. 86.

It is worth noting that although the experimental chamber in this section is vacuum-compatible, most room temperature measurements were made at ambient pressure. This was done because even though the tapered fiber is nominally stationary, we have found it is difficult to approach the bottle to it under vacuum. Vibrations of the fiber and/or the bottle string cause the bottles to touch and become stuck to the fiber as they are approached. Air in the chamber damps these low-frequency vibrations significantly and allows coupling to the bottles without contact, which is important to avoid degradation to the quality of both optical and mechanical resonances.

3.4 Low Temperature Methods

A large portion of the experimental work described in this thesis was performed inside a commercial Oxford Instruments Kelvinox 400HA dilution fridge. Significant efforts are

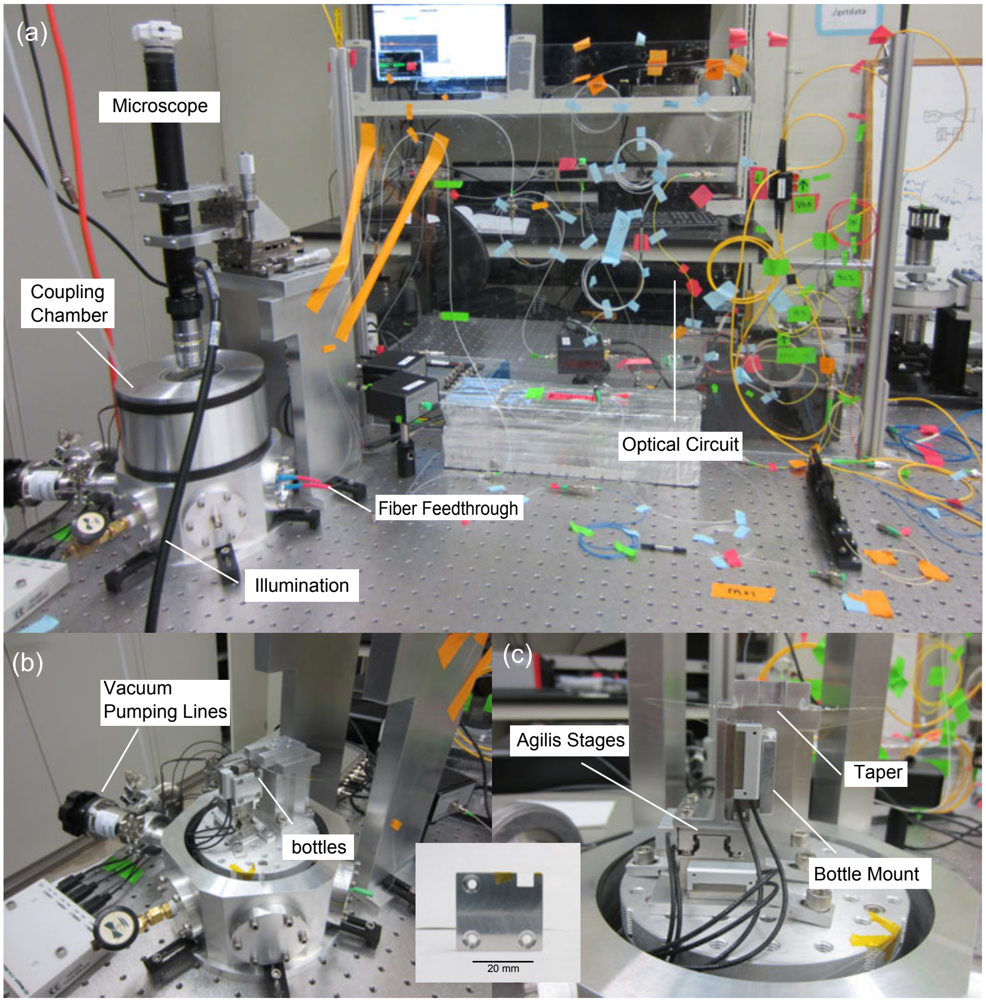

Figure 3.5: Photographs of the coupling setup used for room temperature measurements. (a) The coupling chamber, microscope and fiber optic circuit. (b) and (c) The interior of the coupling chamber, including stages and mounts. Inset: the aluminum bottle mount used for room temperature experiments.

made to minimize the effect of outside vibrations which can both cause heating to the fridge and a deterioration of the small signals we wish to measure. The entire fridge is housed on a floating optical table, which is in turn situated on a separate foundation from the rest of the building. Additionally, significant impedances caused by junctions of very different materials (lead, PVC, stainless steel, etc.) inhibit acoustic waves from travelling though the pumping lines into the fridge.

Described here is first the theory and operation of the dilution fridge, followed by the custom-designed coupling apparatus and specific adaptations made to the room-temperature methods discussed in Sections 3.1-3.3.

3.4.1 Dilution Fridge Operation

As shown in Figure 3.6, the interior of a dilution fridge consists of a number of platforms, each of which serves a specific purpose in the cooling process. The 4 K flange is the topmost stage and isolates the interior vacuum space of the fridge from the surrounding helium bath via the inner vacuum can (IVC) , which is sealed to the 4 K flange using an indium O-ring and evacuated to prevent any convection between the inner workings of the fridge and the helium bath. Situated below the 4 K flange is the 1 K pot, followed by the still plate and the cold plate. At the very bottom is the mixing chamber plate, which also houses the experiment. Mounted on the cold plate (and within the IVC) is the radiation shield, a polished brass and copper shield which reflects electromagnetic, and therefore thermal, radiation away from its interior. Between the IVC and the main dewar is a layer of G-10 called the sliding seal. The main dewar consists of another evacuated volume, the outer vacuum can (OVC), and a volume which is filled with liquid cryogens (the helium bath).

The first two stages of cooling proceed by filling the outer dewar of the fridge with liquid cryogens. First, the dewar is filled with liquid nitrogen (LN_2) and the interior of the fridge is allowed to thermalize to 77 K. Once this has occurred, the nitrogen is pushed out of the dewar with ^{4}He gas and the dewar is filled with liquid ^{4}He, cooling the fridge to 4.2 K. For the remainder of the experiment, the dewar remains filled with liquid helium. As the helium boils off, the gas is recovered and recompressed into a liquid and more liquid helium is transferred into the dewar every three to four days. Liquid nitrogen (and not helium) is used in the first step because its higher latent heat of vaporization and relative affordability make cooling from room temperature to 77 K (where the largest changes in heat capacities and thermal contraction occur) much more efficient and cost-effective.

Once the fridge has thermalized to 4.2 K, further cooling occurs by evaporative cooling of a volume of liquid ^{4}He contained in the 1 K pot. Large pumping lines are used to reduce the pressure in the 1 K pot, which in turn reduces the boiling point of the helium. As the

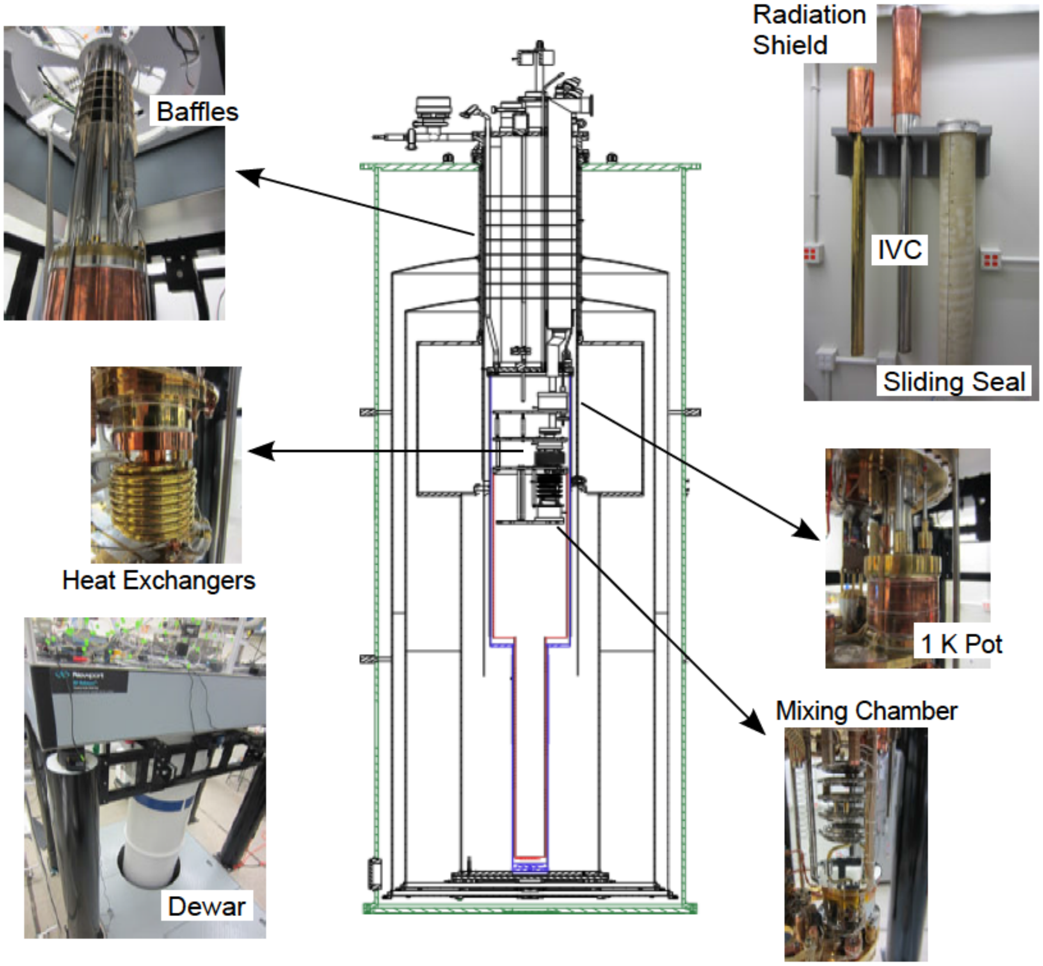

Figure 3.6: Blueprint of our dilution fridge, with photographs of (clockwise from top right): the shields (radiation shield, IVC and sliding seal), the 1 K pot, the mixing chamber, the outer dewar hanging from the optical table, the still and heat exchangers and the baffles above the 4 K flange.

hottest ^{4}He atoms are evaporated and pumped away, the remaining liquid is further cooled. This method provides cooling to temperatures as low as 1 K.

The final stage of cooling, resulting in temperatures as low as 2 mK (7 mK in our system), is dilution refrigeration. Here, we make use of the latent heat of mixing of the ^{3}He and ^{4}He isotopes. Because of the fundamentally different character of the two stable isotopes of helium (one is a boson while the other is a fermion), mixtures of ^{3}He and ^{4}He at low temperatures exist as illustrated in the phase diagram of Figure 3.7. For mixtures of the two isotopes, two stable phases emerge - a ^{3}He-rich (pure) phase and a ^{3}He-poor (dilute) phase. Below temperatures of about 0.1 K, the ^{3}He-rich phase is essentially pure ^{3}He while the ^{3}He-poor phase contains $\sim$6.6% ^{3}He, which is possible because a ^{3}He atom actually has a lower energy when surrounded by ^{4}He atoms than ^{3}He atoms [126]. ^{3}He is a fermion so that when it is in the pure phase, the atoms are forced into higher energy states to satisfy the Pauli exclusion prinicple. As more ^{3}He atoms occupy the dilute phase, they attract each other, further lowering the energy. However, at some point the Pauli exclusion principle forces additional atoms to occupy higher-energy states, limiting the concentration of ^{3}He in the dilute phase to 6.6%. The pure phase consists of only ^{3}He because the bosonic nature of ^{4}He means it is never energetically favourable for these atoms to exist with more ^{3}He than ^{4}He.

Due to the lower density of the pure phase (^{3}He atoms are lighter than ^{4}He atoms), it floats on top of the dilute phase, with a phase boundary between them. To cool the experiment ^{3}He atoms are transferred from the pure phase into the dilute phase. This endothermic process removes the heat of mixing from the mixing chamber surroundings. In practice, the incoming ^{3}He gas is pre-cooled by the liquid helium bath to 4.2 K, before passing through the 1 K pot where it is liquified and cooled to 1 K. The liquid ^{3}He then enters a thin capillary, and is cooled by the still before passing through heat exchangers where it is cooled by outgoing ^{3}He. Once the ^{3}He atoms enter the mixing chamber, they begin in the pure phase before crossing the phase boundary into the dilute phase. Large pumping lines deplete the dilute phase of ^{3}He by pumping away some of the mix through the heat exchangers to the still. Inside the still, the ^{3}He atoms are pumped through stationary superfluid ^{4}He to complete the cycle.

Further cooling can be achieved through adiabatic nuclear demagnetization [126, 127] of a large mass of copper. Our fridge has been designed for compatibility with a demagnetization stage but this has not yet been implemented. Future experiments will make use of this ability.

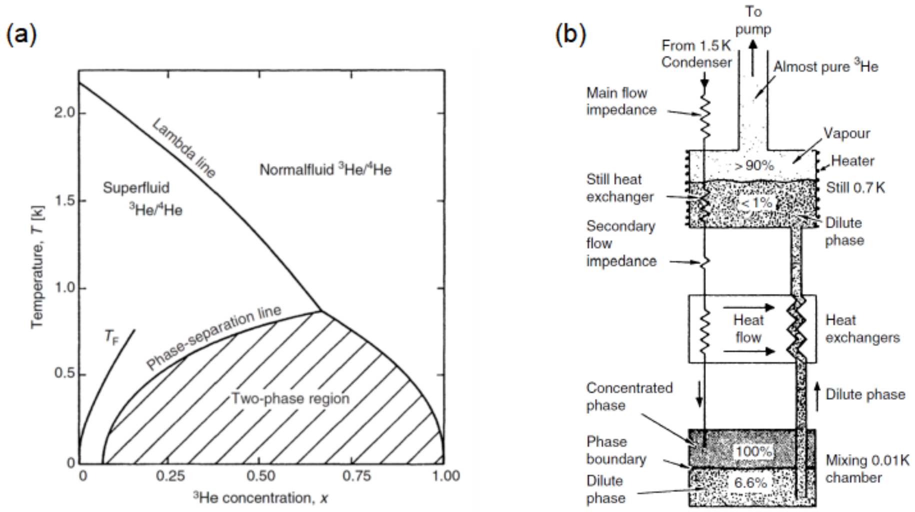

Figure 3.7: (a) Phase diagram of ^{3}He-^{4}He mixtures. Note that the shaded region is a forbidden region, such that below the phase separation line, the mixtures undergo spontaneous separation into ^{3}He-rich and ^{3}He-poor phases. (b) Schematic of dilution fridge operation. Incoming liquid ^{3}He is cooled before entering the mixing chamber. There it crosses the phase boundary to extract the latent heat of mixing from the surroundings before being pumped out through the still. (a) and (b) reproduced from [F. Pobell. *Matter and Methods at Low Temperatures.* Springer-Verlag, third edition, 2007] with permission of Springer Science+Business Media.

3.4.1.1 Thermometry on the Fridge

The fridge is equipped with several thermometers to measure the temperature of various stages of the experiment. Two classes of thermometers are used: primary and secondary. Primary thermometers are based on intrinsic, temperature-dependent physical processes that have become part of the defined temperature scale. Examples of primary thermometers include melting curve thermometers, in which the temperature is read from the pressure along the melting curve of ^{3}He [128], and nuclear orientation thermometers, in which gamma rays from the decay of a radioactive substance are detected [129]. At high temperatures, the emission of the rays is essentially isotropic, whereas at low temperatures, the rays are emitted preferentially in one direction.

Secondary thermometers vary in their temperature readings depending on the exact sample and geometry used and are calibrated using a primary thermometer. Examples of such thermometers include resistive thermometers, in which the resistance of a particular sample varies as a function of the temperature.

In this thesis, we will concern ourselves mostly with the temperature of the mixing chamber stage, which can be read off using both a secondary RuO_2 resistive thermometer and a primary nuclear orientation thermometer. The two thermometers are complimentary and used together as the nuclear orientation thermometer is sensitive only in the range $T < 50$ mK, whereas the RuO_2 is less accurate in the region $T < 20$ mK. Since the function of the nuclear orientation thermometer depends on a counting process, many averages and long periods of time are necessary to obtain an accurate reading. The resistive thermometer responds much faster and more sensitively to small changes in temperature. It is thus used as an indicator of relative changes in temperature, whereas the nuclear orientation thermometer is used to read off the absolute temperature over a long period of time.

It is also important to note that while these thermometers provide a good indication of the temperature of the mixing chamber stage, neither will necessarily give a good indication of the temperature of the sample we are studying. This is a particular challenge in the experiments presented in this thesis as the samples under study are silica, an excellent thermal insulator. Although significant efforts have been made to anchor the sample to the mixing chamber stage, the limited contact between the bottle string and the bottle mount, the thin stems connecting the bottle under study to the mount and heating of the resonator by the probe laser all prevent cooling of the resonator to the base temperature of the fridge. For this reason, we use thermal noise of the mechanical mode to infer the temperature of the resonator, as described in Section 4.3.3.

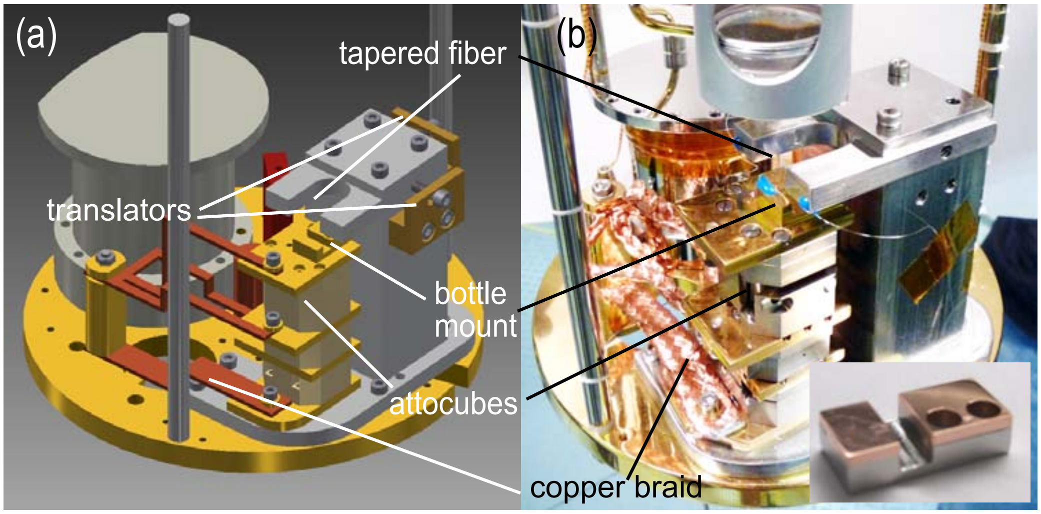

Figure 3.8: (a) Rendering and (b) photograph of the coupling apparatus used on the dilution fridge. Inset: copper-and-Invar bottle mount (before gold-plating) used at low temperatures. Reprinted with permission from [A. J. R. MacDonald, G. G. Popowich, B. D. Hauer, P. H. Kim, A. Fredrick, X. Rojas, P. Doolin, and J. P. Davis. Optical microscope and tapered fiber coupling apparatus for a dilution refrigerator. *Review of Scientific Instruments*, 86(1):013107, 2015]. Copyright 2015, AIP Publishing LLC.

3.4.2 Dilution Fridge Coupling Apparatus

The dilution fridge coupling apparatus was designed around the use of three mutually orthogonal linear nanopositioning stages (attocube LT-UHV ANPx101, ANPz101). These stages have a full travel range of 5 mm with a minimum step size of 50 nm (10 nm) and a continuous piezo-controlled fine tuning range of 5 μm (800 nm) at room temperture (4.2 K). The sample (bottle resonators in our case, but the apparatus is fully compatiable with chip-based resonators) is mounted to these attocube stages, allowing full three-dimensional control over its position while the tapered fiber remains stationary, as in the room temperature setup. This apparatus facilitates coupling to multiple devices during the same experimental run.

As shown in Figure 3.8, the attocube stages and a large Invar block are mounted on a large Invar plate to the mixing chamber stage of the fridge. Invar is an iron-nickel alloy which is designed to undergo very little thermal contraction ($\sim$0.05% from 300 K to 4K), as shown in Figure 3.9. The Invar baseplate is used in an attempt to minimize drifts in the relative alignment of the sample to the tapered fiber, which is mounted to the Invar block.

To maximize thermal anchoring of the sample to the lowest temperatures of the fridge, thin

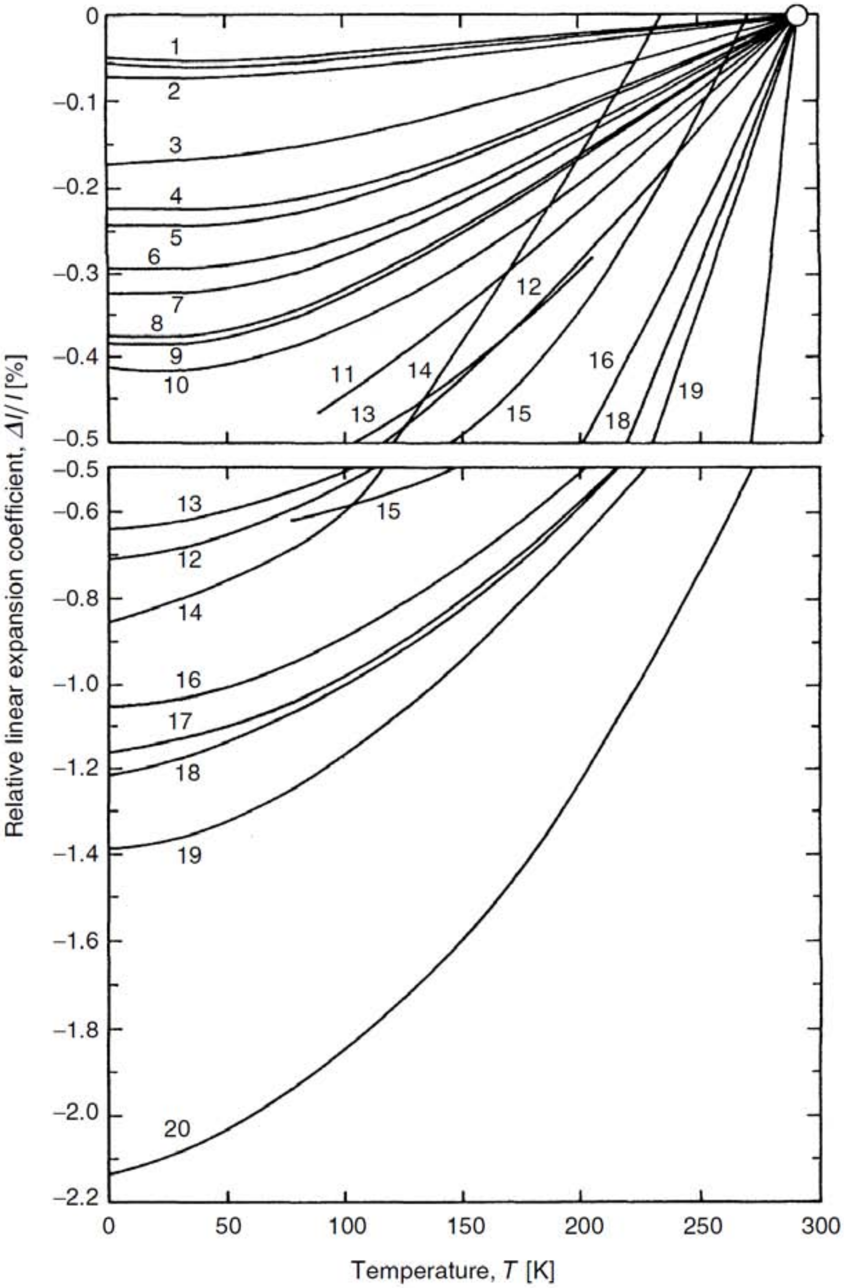

Figure 3.9: Coefficient of thermal expansion of various materials. Materials used in our experiment include: (1) Invar (upper) and glass (lower), (7) copper, (9) brass, (10) aluminum, (13) Vespel, and (20) teflon. Tra-Bond, an epoxy used in gluing the fiber and bottles, is similar to Stycast 2850 GT which has a thermal expansion coefficient slightly larger than (10). Reproduced from [F. Pobell. *Matter and Methods at Low Temperatures*. Springer-Verlag, third edition, 2007] with permission of Springer Science+Business Media.

plates of oxygen-free high conductivity (OFHC) copper are gold-plated and sandwiched between each attocube. The attocubes are made of titanium and ceramic and are not expected to conduct heat very well, so these copper plates are used to shunt any heat generated by their motion to the mixing chamber plate and away from the sample. They are themselves thermally anchored to the mixing chamber plate via a set of copper braids, shown in Figure 3.8.

The bottles are glued to one of the custom-machined bottle mounts shown in Figure 3.10, which is in turn mounted with two screws to the top copper plate. These mounts were designed to be cross-compatible with the room temperature chamber described in Section 3.3, and can be mounted to the Agilis stages using an aluminum adapter (see Figure 3.10(e)). The first bottle mount we tested was made entirely of OFHC copper, with a small (5 mm) channel cut away. Like the copper plates, this mount was also gold-plated to optimize thermal contact and prevent oxidation, which can lead to increased emissivity. However, the significant thermal contraction of the copper ($\sim$0.325%, see Figure 3.9) caused a total length change of 55 μm in the mount, enough to cause the bottles to loosen and vibrate as the attocubes were moved at low temperatures. This made coupling light from the taper without contacting the bottles nearly impossible.

To counteract the negative effects of this thermal contraction, we designed a second bottle mount, made of two pieces of OFHC copper pushed through an Invar base on either side of the channel, as illustrated in Figure 3.10(b-d). The separation of the copper into two separate pieces means that as the bottles are glued in the centre of the copper pieces, differential thermal contraction will cause tensioning of the bottles instead of detensioning as cooling proceeds. As with the other pieces of copper in the apparatus, this bottle mount is also gold-plated.

We also had to adapt the taper- and bottle-gluing process described in Section 3.1 since the Devcon five-minute epoxy does not remain adhered to the bottle or taper mounts at cryogenic temperatures. We tested several epoxies, including a UV-curing epoxy and Tra-Bond epoxy by gluing tapered fibers to pieces of Invar and copper, and immersing them in liquid nitrogen. Only the Tra-Bond secured fibers survived the tests. Unfortunately, we also found that the Tra-Bond lacked the tensioning properties of the Devcon epoxy, which prevented us from observing the mechanical motion of the bottles. We therefore developed the gluing procedure illustrated in Figure 3.10(f), where the bottles are first glued with the Devcon epoxy, and then with Tra-Bond. This combination allows the bottle string to be tensioned as the five-minute epoxy dries; this tensioned state is maintained at low temperatures by the Tra-Bond after the five-minute epoxy ceases to adhere.

The tapered fiber is glued in the same way to the Invar fork-shaped fiber holder, shown in Figure 3.11(a). It is fusion-spliced to two long lengths ($\sim$20 m) of fiber which have been

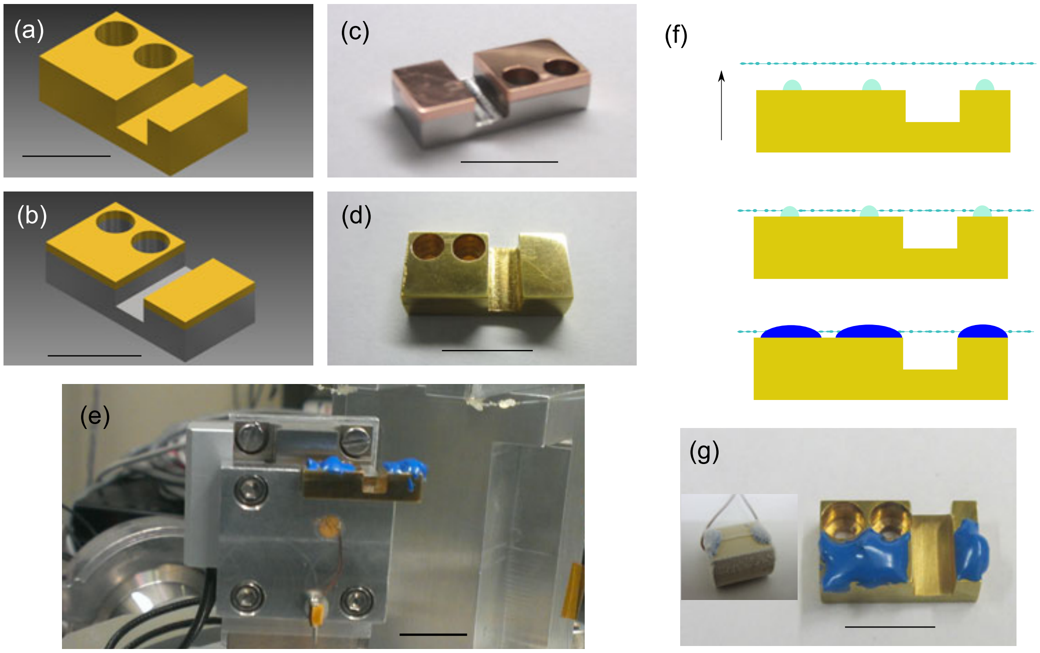

Figure 3.10: Rendering of (a) copper and (b) copper-and-Invar bottle mount. Photographs of the copper-and-Invar mount before (c) and after (d) gold-plating. (e) Copper bottle mount and aluminum adapter inside the room temperature chamber. (f) Illustration of the gluing procedure used for dilution fridge experiments, where both five-minute (light blue) and Tra-Bond (dark blue) epoxies are used. (g) Photograph of the bottles and mount after gluing. Inset: A tapered fiber glued to a gold-plated OFHC copper piece after being immersed in liquid nitrogen. All scale bars are 10 mm.

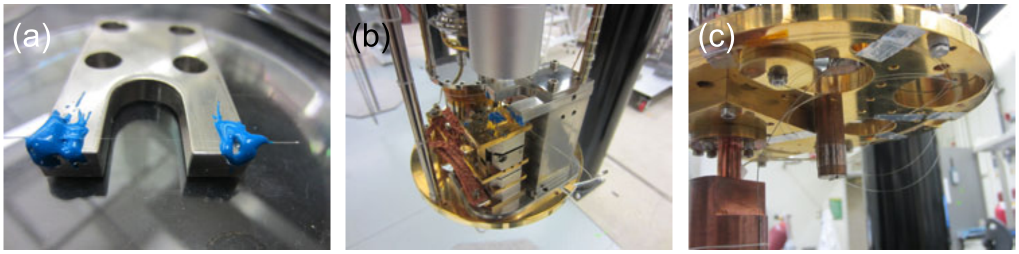

Figure 3.11: (a) Invar fiber-holder, with a taper glued using both five-minute epoxy and Tra-Bond. (b) The tapered fiber is mounted to the Invar block on the mixing chamber plate of the fridge. (c) Fibers are taped to the underside of the mixing chamber plate with Kapton and aluminum tape to prevent accidental thermal contact between the mixing chamber and the radiation shield.

thermally anchored to the still plate of the fridge. The fiber holder is then inverted and mounted to the Invar block (Figure 3.11(b)). Two brass push-pull translators, shown in Figure 3.8 are used to align the taper relative to the optical axis of an imaging system, described in further detail in Section 3.4.3 and Ref. 47. The extra length of fiber is then secured with Kapton and aluminum tape to the Invar block and the underside of the mixing chamber stage, as shown in Figure 3.11(c).

3.4.2.1 System Efficiency

As the taper is being installed in the fridge, we see a rapid decrease in the transmission, as shown in Figure 3.12(a). We believe that this occurs due to the adsorption of water molecules and other contaminants onto the fiber, which then facilitates scattering of light out of the tapered region. When we evacuate the IVC, we see a marked increase in the transmission (Figure 3.12(b)) as contaminants are pumped away. The difference in the maximum transmission between Figure 3.12(a) and (b) arises because we can only measure the transmission through the taper once both ends are spliced, which likely occurs after significant adsorption has already taken place.

Starting with a highly efficient fiber taper (90-95% after pulling), we can reach a total optical efficiency through the fridge of ∼70% at room temperature. However, as the fridge is cooled, we see the efficiency drop drastically to $\lesssim$50%. In Figure 3.12(c), we show the transmission through a non-tapered fiber which has two fusion splices as the fridge is first cooled from room temperature to 77 K, and then warmed up again. The transmission through the fiber drops to ∼80% of its original transmission at 77 K, but makes a complete recovery at room temperature. We repeated this test for a single splice, in which the transmission was reduced to ∼90% of its initial value, leading us to conclude that the splices are responsible for a significant fraction of the temperature-dependent loss in the system, with the taper itself contributing the remaining portion.

3.4.3 Low Temperature Imaging[1]

The final requirement for performing optomechanical experiments inside our dilution fridge is the ability to align the taper and resonator with respect to one another. Differential thermal contraction between the various materials used in our setup (see Figure 3.9) causes significant shifts in the relative position of the taper and resonator between room temperature and 4.2 K. To remedy this, we have designed and implemented an imaging system which facilitates the use of the attocube stages to counteract any changes in alignment.

---

[1] Material in this section has been previously published in Ref. [47].

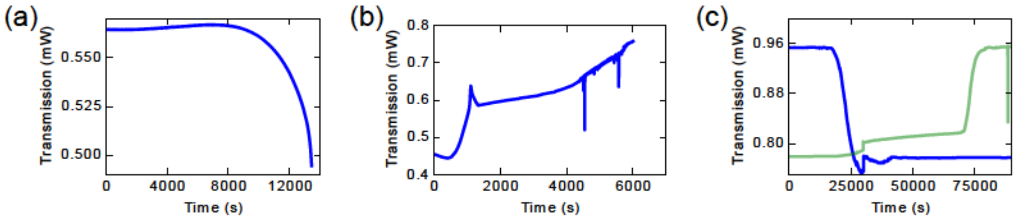

Figure 3.12: (a) The fiber transmission decreases during the installation process but (b) increases rapidly when the IVC is evacuated. (c) Testing transmission through a fiber with two splices but no taper as the fridge is cooled (blue) to 77 K and then warmed up to room temperature (green).

Performing optical measurements in cryogenic environments has conventionally been done through the use of a series of optical access windows. These are fairly easily implemented in helium flow cryostats, which reach minimum temperatures of ~1 K. However, in a dilution fridge environment, such windows impose an upper limit on the achievable base temperature of the fridge. Their presence results in increased heat loads, such that significant optimization of these windows for shielding infrared and radio frequency (RF) radiation is necessary. With such optimization, temperatures as low as 10 mK can be reached[2], and such systems have successfully been used to image helium crystal surfaces [131, 132, 133] and orientations [134], as well as acoustic waves in helium [135].

Beginning in the early 1990s, there was significant interest in imaging ^{3}He and ^{4}He at sub-mK temperatures. This led to the development of cryogenic imaging systems which could be completely contained within the dilution fridge. The first of these systems, developed at the Helsinki University of Technology, used a Helium-Neon (HeNe) laser to interferometrically image for the first time the superfluid ^{3}He surface at temperatures as low as 0.7 mK [136]. The experiment used a bundle of 30000 optical fibers to transport the image to a camera housed at room temperature. A more popular technique, developed at both Helsinki [137] and the University of Leiden [138], used a charge-coupled device (CCD) camera housed at 4.2 K inside the fridge to image the helium surface, eliminating the fiber bundle and increasing the resolution of the image. Housing the camera inside the fridge does however cause several complications, including heating from both thermal and RF radiation of the CCD, and time delays between the CCD and its room-temperature control electronics [137, 138, 139]. This necessitates further shielding and custom timing electronics.

We have adopted an approach similar to that of the first Helsinki system, described in Ref. 136, to assist in the alignment of our optomechanical apparatus. We use a 530 nm

---

[2] Temperatures as low as 10 mK have been reached in unpublished work by the Balibar group, while 15 mK has been demonstrated in, for example, [A. Haziot, X. Rojas, A. Fefferman, J. Beamish, and S. Balibar. Giant Plasticity of a Quantum Crystal. *Physical Review Letters*, 110(3):035301, 2013].

light-emitting diode (LED, Thorlabs M530F1) as an illumination source and a coherent bundle of 37000 fibers (Fujikura FIGH-40) to transport an image to a room temperature camera consisting of the complementary metal-oxide-semiconductor (CMOS) chip from a commercial webcam (Logitech C200). Schematics and photographs of the imaging system are shown in Figure 3.13.

LED light is brought into the fridge via a cleaved multimode fiber (Thorlabs AFS105/125Y) and then collimated using a combination consisting of a strong condenser lens and a weak meniscus lens (Thorlabs ACL1210-A and LE1104-A, respectively), shown in Figure 3.13(b) as L1 and L2. The beam proved difficult to collimate, due both to its relatively broadband nature (spectral linewidth of $\sim$30 nm) and the large spatial mode exiting the multimode fiber. A number of lenses and combinations of lenses, including aspherics, plano-convex lenses and achromatic doublets were thus tested for collimating the light, with the above combination (condenser and meniscus) proving to be most successful.

After collimation, the beam impinges on a beam splitter, such that 90% of the light is transmitted and dumped onto a black metal velvet absorber (Acktar Advanced Coatings) affixed to the interior of the IVC. Since very little light is required for imaging the optomechanical devices, this ensures that most of the heat load is transferred to the helium bath at 4.2 K, as opposed to the sample. The remaining 10% of the light is focussed to a $\sim$1 mm spot on the sample using an achromatic doublet with a focal length $f = 30$ mm (Thorlabs AC254-030-A, AD1 in Figure 3.13). The reflected light is then collected into the fiber bundle with a second achromatic doublet AD2, which for most of the experiments in this thesis had a focal length of 100 mm (Thorlabs AC254-100-A). However, we also tested achromatic doublets with focal lengths of 35 mm (Thorlabs AC254-035-A) and 75 mm (Thorlabs AC254-075-A). At the output of the fiber bundle, the light is re-collimated by an $f = 35$ mm achromatic doublet (AD3) and focussed onto the camera using an $f = 75$ mm plano-convex lens (L3). All optics are mounted in 1-inch diameter aluminum lens tubes (Thorlabs SM1 series), which are stripped of their anodization to prevent outgassing.

Alignment of the lenses is accomplished with the aid of slots which are milled into either side of each lens tube. Each lens is held in place by two retaining rings, which can then be adjusted by hand. Thin pieces of paper are inserted between the lenses and retaining rings to prevent any adverse effects of the larger thermal contraction of the aluminum on the glass. Both the input multimode fiber and fiber bundle are aligned using home-built brass xy tilt manipulators (as shown in the inset of Figure 3.13(c)), which have small centred holes (diameters 0.01" and 0.04" for the injection fiber and fiber bundle, respectively) and use small set-screws to make adjustments to the position and angling of the fiber.

The second achromatic doublet (AD2) was chosen to optimize the area of the resulting image, such that the field of view was large enough to identify a particular optomechanical

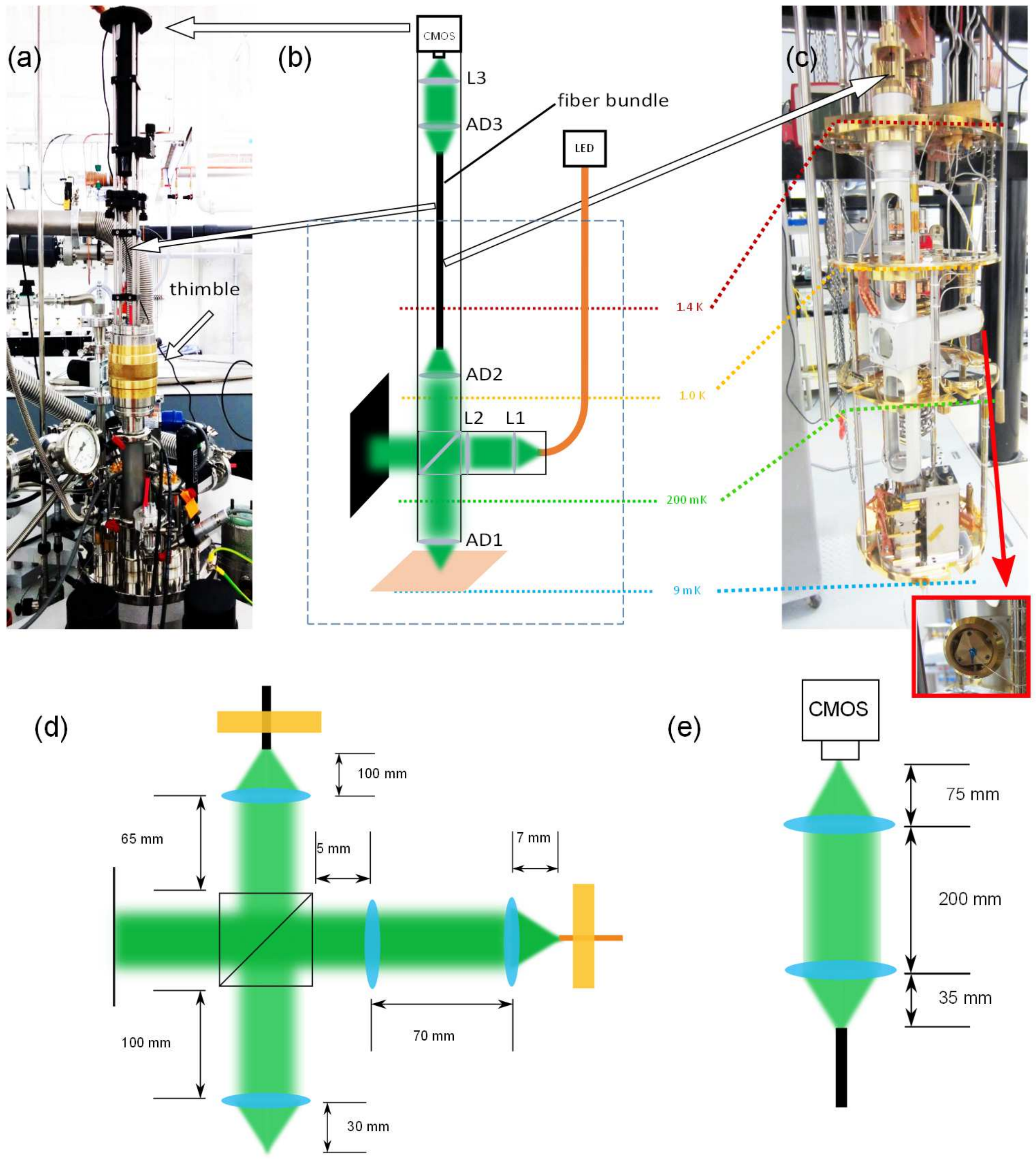

Figure 3.13: (a-c) Schematic and photographs of the microscope setup, showing the optics, thimble, fiber bundle and camera used. Inset: brass xy tilt manipulator used for fiber alignment. (d-e) Detailed schematic of the optics used in the microscope, with approximate distances between lenses. (a-c) adapted with permission from [A. J. R. MacDonald, G. G. Popowich, B. D. Hauer, P. H. Kim, A. Fredrick, X. Rojas, P. Doolin, and J. P. Davis. Optical microscope and tapered fiber coupling apparatus for a dilution refrigerator. *Review of Scientific Instruments*, 86(1):013107, 2015]. Copyright 2015, AIP Publishing LLC.

device while keeping the resolution fine enough to position a tapered fiber (which has a diameter of $\sim$1 μm) accurately. Since the $f = 30$ mm achromatic doublet was the smallest focal length lens available, we were not able to focus to a smaller spot on the chip. Instead, we achieved an appropriate magnification of the image by using the long focal-length AD2 to focus the image to an $\sim$4 mm spot at the fiber bundle - much larger than the bundle's image circle diameter of $\sim$850 μm. As each fiber in the bundle acts as a single pixel, we can examine smaller features by excluding a portion of the reflected image's area from the fiber bundle. The resulting magnification of $\sim$3.3 corresponds to a resolution of $\sim$1 μm. Images taken using the microscope are shown in Figure 3.14, at room and base temperature.

The fiber bundle is brought to room temperature through a direct line-of-sight port from the top of the fridge. A combination of thin-walled stainless steel tubing and baffles inside this port minimize heat transfer from room temperature. Radiation is further inhibited by offsetting the holes in the baffles through which the bundle passes. The only line of sight into the fridge is thus through the bundle itself, which is thermally insulating.

A thimble (Huntington VF-178-275) on top of the fridge permits vertical translation of the entire microscope apparatus along the optical axis with a resolution of 50 μm over a total range of 50 mm. This allows adjustment of the focal plane of the image without changing the alignment of the optics. To facilitate this motion, a teflon ring is used at each stage to guide the lens tubes, preventing any tilting or vibrations. The teflon also serves to minimize heat leaks between stages.

As described above, the sample can be moved independently using the three attocube stages. The tapered fiber cannot be moved in such a way, so it is important to align it with the imaging apparatus before cooling down. To accomplish this, we use the set of brass push-pull translators shown in Figure 3.8, which are mounted on the Invar block at room temperature and removed before cooling down. These allow adjustment in the two dimensional plane perpendicular to the optical axis. The tapered fiber is positioned $\sim$200 μm outside the microscope's field of view, to account for reproducible drifts in the relative alignment that occur as the fridge is cooled down, as shown in Figure 3.15. The fiber holder is then tightened to the Invar block and the push-pull translators are removed.

To assist in locating the tapered region, which is difficult to see due to the limited resolution of the microscope, we inject red light from a HeNe laser into the measurement fiber. The red light scatters preferentially from the thinnest part of the taper, making it more visible in the image, as shown in Figure 3.14(d). This will be especially helpful for future experiments using on-chip devices, which require locating the lowest point of a dimpled tapered fiber [86, 87].

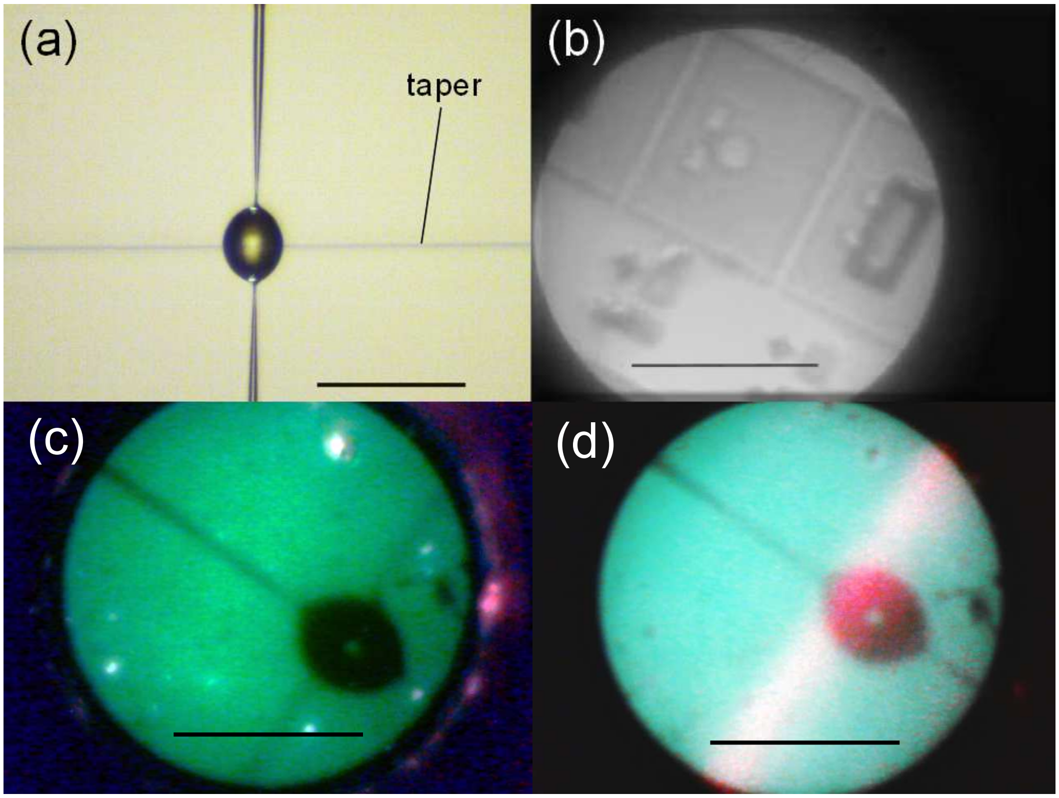

Figure 3.14: (a) Image of the bottle and taper taken using the microscope in the room temperature setup. (b) An on-chip torsional optomechanical resonator [22, 87] as seen through the low temperature microscope at room temperature. Low-temperature microscope images of the bottle resonator and taper at 9 mK (c) and at room temperature with HeNe illumination of the taper (d). Figure reprinted with permission from [A. J. R. MacDonald, G. G. Popowich, B. D. Hauer, P. H. Kim, A. Fredrick, X. Rojas, P. Doolin, and J. P. Davis. Optical microscope and tapered fiber coupling apparatus for a dilution refrigerator. *Review of Scientific Instruments*, 86(1):013107, 2015]. Copyright 2015, AIP Publishing LLC.

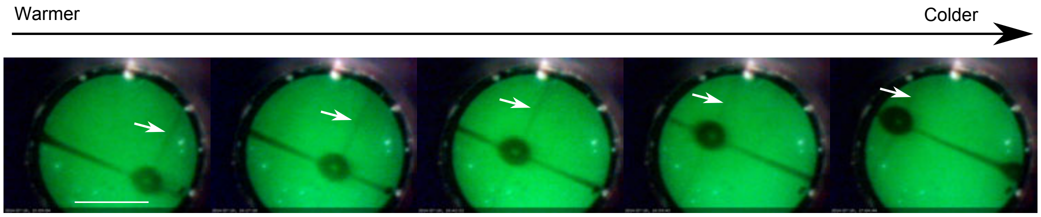

Figure 3.15: Thermal contractions cause the tapered fiber (denoted by the arrow) to drift from the bottom right to the top left corner of the image as LN_2 is transferred into the fridge. These drifts were reproducible and compensated for by positioning the fiber outside the field of view at room temperature. Scalebar 100 μm.

3.4.4 Heating to the Cryogenic Environment

We find that the most significant source of heating to the cryogenic environment results from the scattering of laser light in the tapered region of the fiber, although the green LED light and continuous motion of the attocubes can also heat the mixing chamber. Continuous motion of the attocubes causes significant heating to the environment, but under normal experimental conditions, we use only a few discrete steps along with the continuous voltage offset of the attocube piezo. These actions do not result in any observable heating.

We can quantify the effects of both laser power and LED light by determining the cooling power of the fridge as shown in Figure 3.16(a). We apply a predetermined heat load to the mixing chamber using a resistive heater and measure the resulting base temperature. To obtain accurate results, this measurement is done with the nuclear orientation thermometer over the course of several hours after the temperature has stabilized. We then fit the data with the equation [126]

$$\dot{Q}_{MC} = pT^2 - \dot{Q}_{HL}, \tag{3.1}$$

where $\dot{Q}_{MC}$ is the applied heat load, p is a phenomenological constant describing the molar flow rate of ^{3}He, and T is the resulting base temperature of the fridge. We find a static heat leak $\dot{Q}_{HL} \sim 900$ nW, which imposes the ultimate limit on the fridge's base temperature (9.02±0.18 mK), as shown in the inset of Figure 3.16(a). This represents only a slight increase over the unloaded fridge base temperature of ∼7 mK.

We then measure the base temperature of the fridge in the same manner as the optical power in the tapered region of the fiber is increased. Using Figure 3.16(a), we determine the resulting heat load from the measured temperature, which is shown in Figure 3.16(b). For the fiber measured, we find that ∼36% of the total power in the taper contributes to heating the fridge, which corresponds to most of the taper losses. However, for very low optical powers (<250 nW in the taper), it is possible to measure the optical resonances without any heating to the fridge, as shown in Figure 3.17.

We measure the heat load from the microscope's green illumination in a similar manner, turning up the power and measuring the base temperature of the fridge. The results are shown in Table 3.1. Also shown are measurements performed at room temperature indicating the total free-space intensity of the LED, and the intensity of the green light focussed onto the sample and dumped onto the IVC. Since coupling light from the LED into the fiber is very inefficient, only a small fraction of (∼0.18%) of the total light is dumped onto the IVC, with even less light (∼0.014%) reaching the sample. Under normal experimental conditions, very little ($\lesssim$100 nW) light is required to image the sample, resulting in a heat

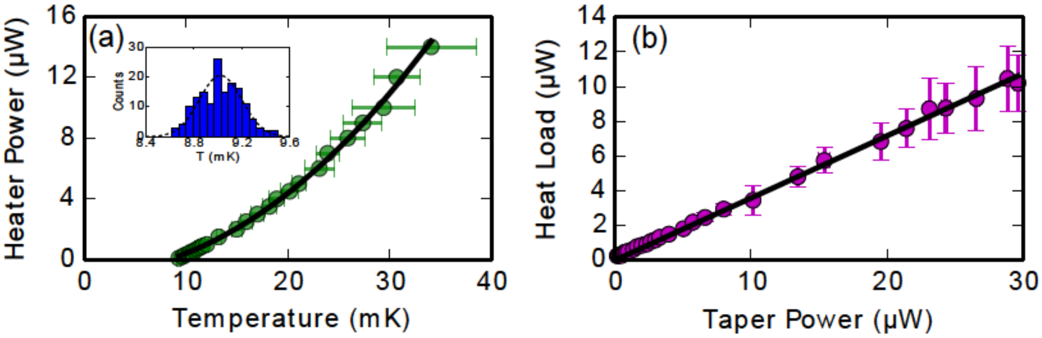

Figure 3.16: (a) Cooling power of the fridge measured by applying a known heat load to the mixing chamber and measuring the resulting base temperature of the fridge with the nuclear orientation thermometer. The inset shows the base temperature of the fridge with no applied heat load. (b) Heat load on the fridge resulting from laser light lost from the taper. Figure adapted with permission from [A. J. R. MacDonald, G. G. Popowich, B. D. Hauer, P. H. Kim, A. Fredrick, X. Rojas, P. Doolin, and J. P. Davis. Optical microscope and tapered fiber coupling apparatus for a dilution refrigerator. *Review of Scientific Instruments*, 86(1):013107, 2015]. Copyright 2015, AIP Publishing LLC.

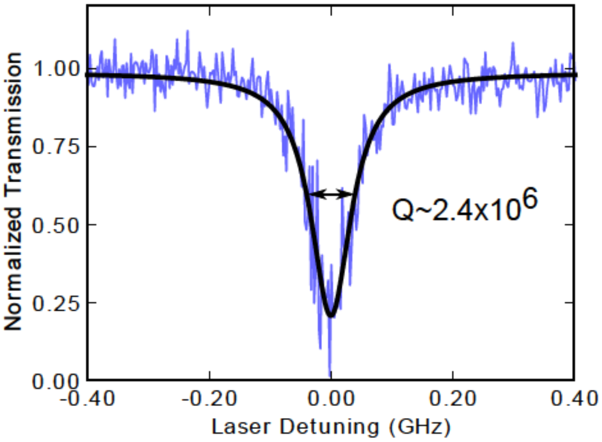

Figure 3.17: Optical resonance of a bottle resonator around 1598 nm, measured at a fridge temperature of 9 mK with 250 nW of optical power. Reprinted with permission from [A. J. R. MacDonald, G. G. Popowich, B. D. Hauer, P. H. Kim, A. Fredrick, X. Rojas, P. Doolin, and J. P. Davis. Optical microscope and tapered fiber coupling apparatus for a dilution refrigerator. *Review of Scientific Instruments*, 86(1):013107, 2015]. Copyright 2015, AIP Publishing LLC.

Table 3.1: The intensity of LED light incident on the sample and IVC, along with the base temperature of the fridge and inferred heat load. Reprinted with permission from [A. J. R. MacDonald, G. G. Popowich, B. D. Hauer, P. H. Kim, A. Fredrick, X. Rojas, P. Doolin, and J. P. Davis. Optical microscope and tapered fiber coupling apparatus for a dilution refrigerator. *Review of Scientific Instruments*, 86(1):013107, 2015]. Copyright 2015, AIP Publishing LLC.

LED (mW)	Sample (μW)	IVC (μW)	T (mK)	$\dot{Q}$ (μW)
0.9	0.12	1.5	9.01	0.17
2.0	0.31	4.6	9.53	0.30
4.0	0.50	6.7	10.21	0.47
9.0	1.10	15.2	11.56	0.86
15.0	2.00	28.0	13.51	1.51
17.5	2.50	34.5	14.45	1.85

load of <170 nW, much less than the static heat leak of the fridge. We therefore observe no increase in temperature. We do, however, notice a very slight increase in the base temperature when the lab lights are on (0.1 mK as measured with the resistive thermometer). We believe this is due to white light coupling into the measurement fibers above the fridge.

3.5 Measurement Details

3.5.1 Optical Spectroscopy

Measurements of optical cavities are performed by scanning the wavelength of a tunable diode laser across the optical resonances. Most of the measurements discussed in this thesis are made using a Santec TSL-510C external cavity diode laser, which has a mode-hop free tunable range of 1500-1630 nm and an internal wavelength meter. The Santec was chosen for its wavelength stability, repeatability and fine tuning resolution, as shown in Table 3.2. Other lasers that were used included New Focus Velocity TLB-6330, Velocity TLB-6712 and Vidia Discrete 6427.

Coarse wavelength scans are performed by stepping the laser's wavelength over its tunable range and monitoring the transmission of the laser light through the tapered fiber using a photodiode (usually a New Focus 1611FC-AC 1 GHz detector). The transmission is recorded with a National Instruments NI USB-6341 data acquisition (DAQ) card. The internal wavelength meter in the Santec laser allows us to extract the absolute wavelength during these scans by simultaneously recording the transmission and a fast trigger signal from the laser with the DAQ card. Wavelengths which coincide with these triggers are stored inside the laser and can be recalled later and matched in software to the trigger signal, as shown in Figure 3.18.

Table 3.2: Specifications for lasers used in this thesis.

Laser	Santec TSL-510C	New Focus 6300	New Focus 6712	New Focus 6427
Tunable Range (nm)	1500-1630	1550-1630	765-781	1520-1570
Coarse Resolution (pm)	1	20	10	1
Fine Tuning Range (pm)	80	260	-	-
Fine Resolution (fm)	4	300	-	-
Stability (pm)	< 1	-	1	5
Repeatability	2.5	100	30	30
Output Power (mW)	20	10	25	4
Linewidth (kHz)	200	300	< 200	-

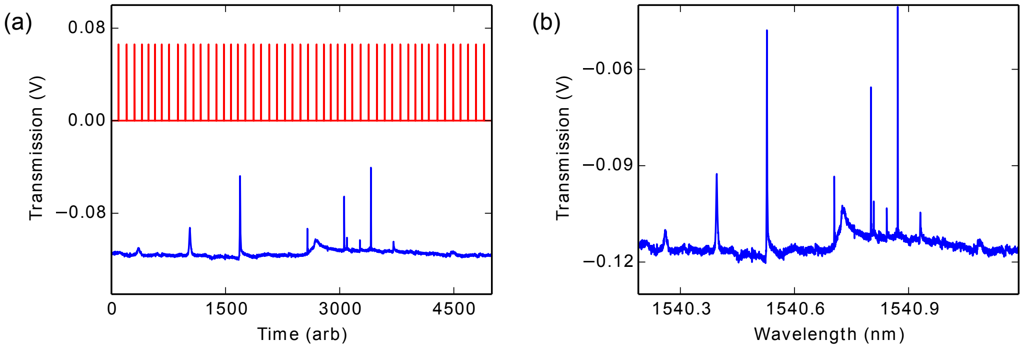

Figure 3.18: Coarse optical scans showing several bottle optical resonances. (a) The recorded transmission (blue) and trigger signals from the laser (red), corresponding to wavelength readings stored inside the laser. These readings are later recalled and matched to the trigger signals in software to determine the wavelengths shown in (b).

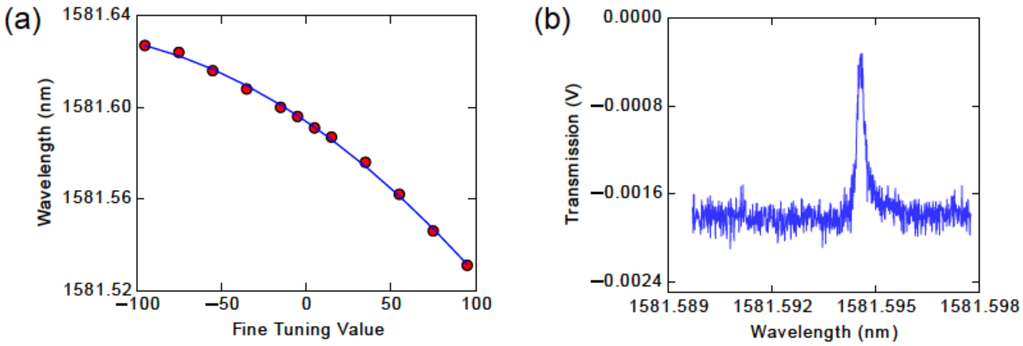

Figure 3.19: (a) Measured wavelengths (red circles) at various FT values. The blue curve is a fit to the data with a second degree polynomial. (b) Fine scan across a bottle resonance plotted versus the wavelength calibrated from (a).

Fine scans of an optical resonance are performed by moving one of the mirrors of the laser cavity continuously using a piezoelectric element. The Santec's internal wavelength meter doesn't function during these fine scans, so we calibrate the wavelength of a fine scan by measuring the wavelength at several points over the entire fine tuning range (denoted as fine tuning (FT) values from -100 to 100 in increments as small as 0.01) with an external wavelength meter (Hewlett-Packard 8612OB). These wavelength measurements are then fit with a second degree polynomial to determine the correspondence between the FT value and the wavelength. Figure 3.19 shows an example of this calibration and a wavelength-calibrated fine scan.

3.5.2 Mechanical Spectroscopy

There are two ways of measuring the motion of the mechanical resonator via the optical cavity. The first, and simplest to implement, is the so-called direct-detection scheme [11, 22, 86] where the probe laser is detuned slightly from the cavity resonance such that shifts in the cavity's resonance frequency are transduced as fluctuations in the laser transmission through the cavity. Most of the measurements discussed in this thesis were made using variations on this technique. However, we also investigated an interference technique called optical homodyne detection [140] which is sensitive to changes in the phase of the intracavity light field.

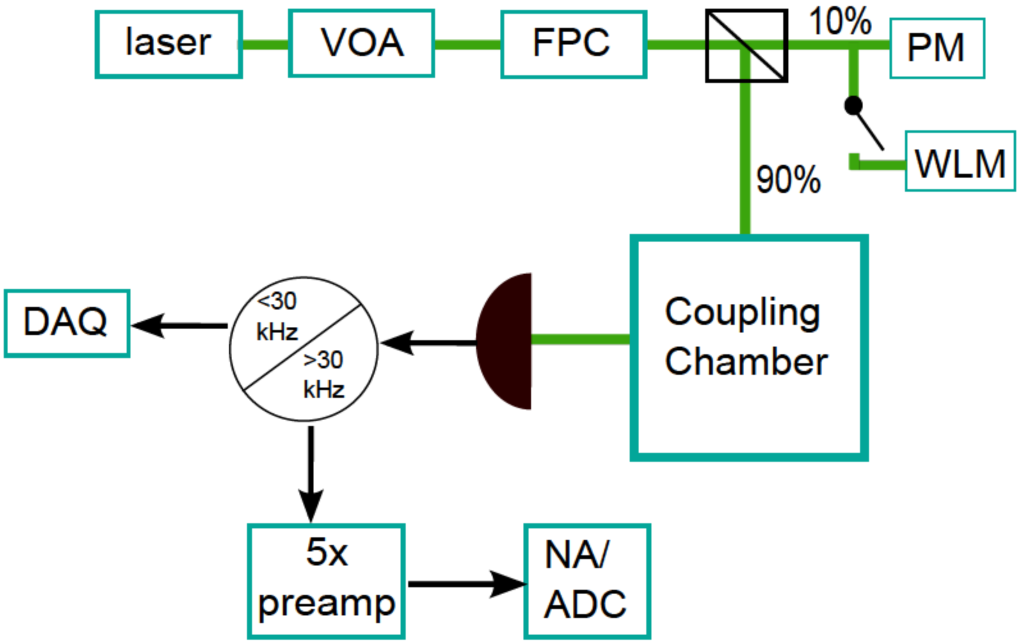

Figure 3.20: Schematic of the detection system used for room temeperature measurements. Abbreviations are VOA - variable optical attenuator, FPC - fiber polarization controller, PM - power meter, WLM - wavelength meter, DAQ - data acquisition card, ADC - analog-to-digital converter, NA - network analyzer

3.5.2.1 Direct Detection Techniques

For room temperature measurements, the setup shown in Figure 3.20 was used to detect mechanical motion of the bottle resonators. A 1 GHz photodetector was used, in which internal high- and low-pass filters (HPF and LPF, respectively) separate the signal into AC (30 kHz-1 GHz) and DC (<30 kHz) components. The DC signal is used to monitor the transmission profile of the optical resonance, as described in Section 3.5.1, while a time-trace of the AC signal is amplified (SRS SR445A 5× preamp) and recorded with a fast analog-to-digital converter (ADC, Ultraview Ultradyne AD12-2000). The ADC works at 2 GHz, permitting detection of signals at frequencies up to 1 GHz, over time periods as long as 2 s. The recorded time-trace can then be Fourier-transformed in software to analyze the frequency-space characteristics of the signal. A network analyzer was used to independently confirm the observation of mechanical oscillations at frequencies <200 MHz.

Since this technique is sensitive to changes in the intracavity amplitude, the signal is generally best transduced at the laser detuning where the slope of the cavity transmission profile is steepest (see for example, Ref. 22). It also scales favourably with increasing laser power as increasing the number of intracavity photons both increases the effective optomechanical coupling rate and reduces the effects of detector shot noise [24].

However, at cryogenic temperatures, the use of more laser power is not always so desirable. Although it still increases the detected signal, larger optical power can also contribute to heating both the resonator and the environment. At the same time, lower temperatures correspond to a smaller thermally-driven motion of the resonator, which is harder to detect. Thus to detect smaller mechanical signals while limiting any increases in the probe laser power, we test several modifications. The first is to simply replace the electronic preamplifier in Figure 3.20 with a lower-noise, higher-gain version (Femto HSA-X-1-40, 100× preamp).

A second modification attempts to amplify the optical signal before it reaches the detector using an erbium-doped fiber amplifier (EDFA, Amonics AEDFA -23-B-FA). The EDFA is doped with rare-earth ions which are excited with a pump laser and can then undergo stimulated emission in the 1550 nm wavelength band to amplify small optical signals in that region. The third modification was to use an avalanche photodiode (APD, New Focus 1647) in place of the 1 GHz detector. The APD is a photodiode operated at a high reverse bias such that carriers generated by incoming photons are quickly accelerated and generate secondary carriers, which effectively amplifies the detector photocurrent. When using either the EDFA or the APD, it is important to note that we used the SRS 5× preamp and not the Femto preamp because the signal that resulted from such a configuration exceeded the input restrictions of the ADC.

With all of these detection schemes, we use variable optical attenuators (VOAs) to control the power through the tapered fiber, fiber polarization controllers (FPCs) to match the polarization of the light to the bottle mode we are interested in and a fiber beamsplitter to simultaneously monitor the optical power through the entire optical circuit with a power meter (PM). The optical circuit used on the dilution fridge (Figure 3.21) is naturally more complicated due to the number of different techniques investigated, and also includes wavelength division multiplexers (WDMs, OZ Optics) for use with red light in the imaging system, and a variable coupler (VC, Evanescent Optics). Several micro-electromechanical system (MEMS) switches (Sercalo SL1x2-9N-FC/APC and SL1x4-9N-FC/APC) and a VOA used on the dilution fridge are electrically controlled by the DAQ card, minimizing the need to touch the fridge (which can cause unwanted vibrations) while it is running.

3.5.2.2 Homodyne Detection

The final detection method investigated in this thesis was an optical homodyne technique. In an optical homodyne detection scheme, the system to be measured is inserted in one arm of a Mach-Zehnder interferometer (MZI). Practically, this amounts to splitting the input

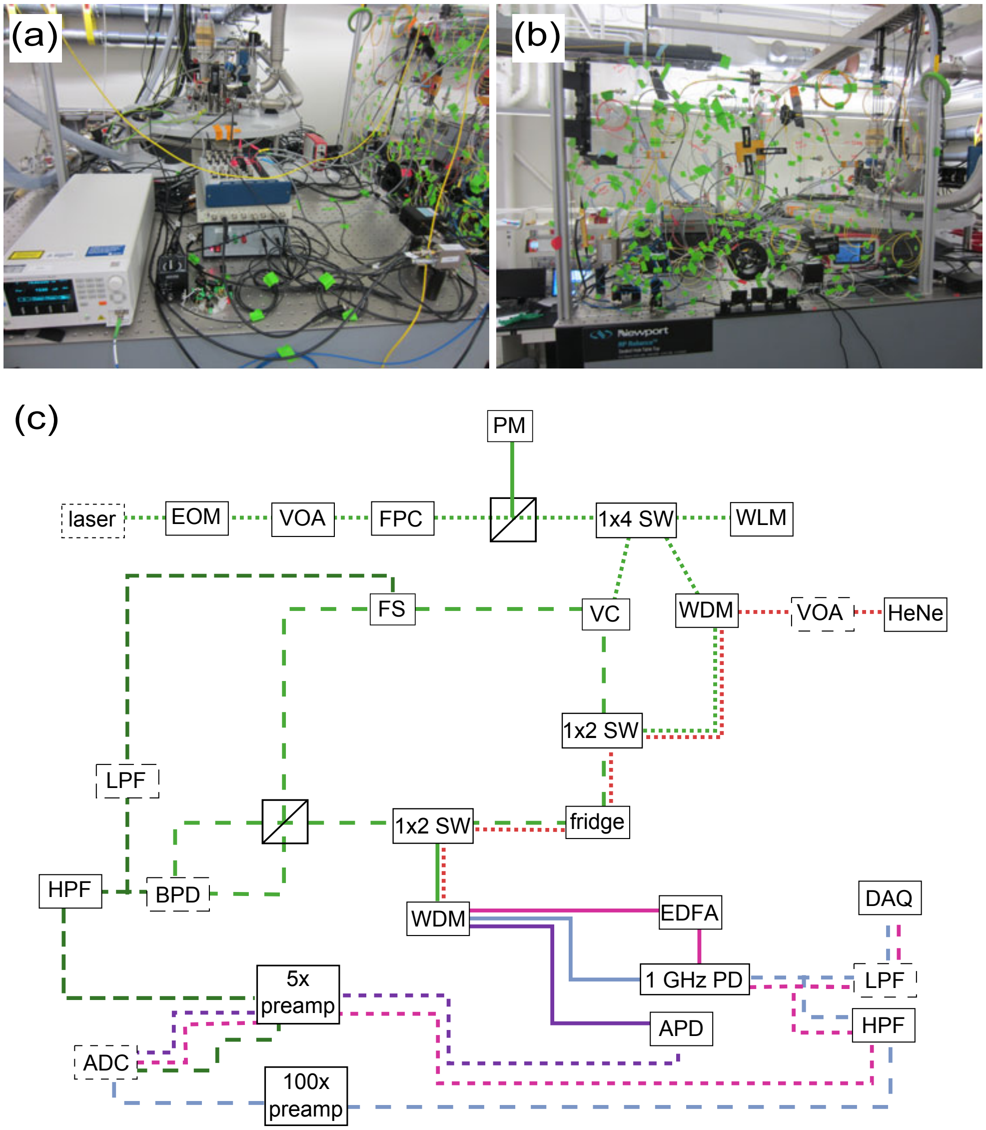

Figure 3.21: Photographs of (a) the laser and electronics and (b) the fiber optics housed on top of the fridge and used in the low temperature experiments. (c) Detailed schematic of the optical circuit surrounding the dilution fridge. Dotted red lines indicate the path of red light from a HeNe laser used in the imaging system described in Section 3.4.3, while solid lines denote possible paths for the 1550 nm light. Dashed lines denote electronic connections. Green, pink, blue and purple lines indicate paths used for homodyne, and direct detection schemes using the erbium-doped fiber amplifier (EDFA), low-noise preamp, and avalanche photodiode (APD), respectively. Note that for the homodyne and APD schemes, the DC optical transmission is monitored with the 1 GHz photodiode. Abbreviations are EOM - electro-optic modulator, SW - switch, WDM - wave division multiplexer, VC - variable coupler, HeNe - Helium Neon laser, BPD - balanced photodiode, HPF/LPF - high-/low-pass filter, FS - fiber stretcher.

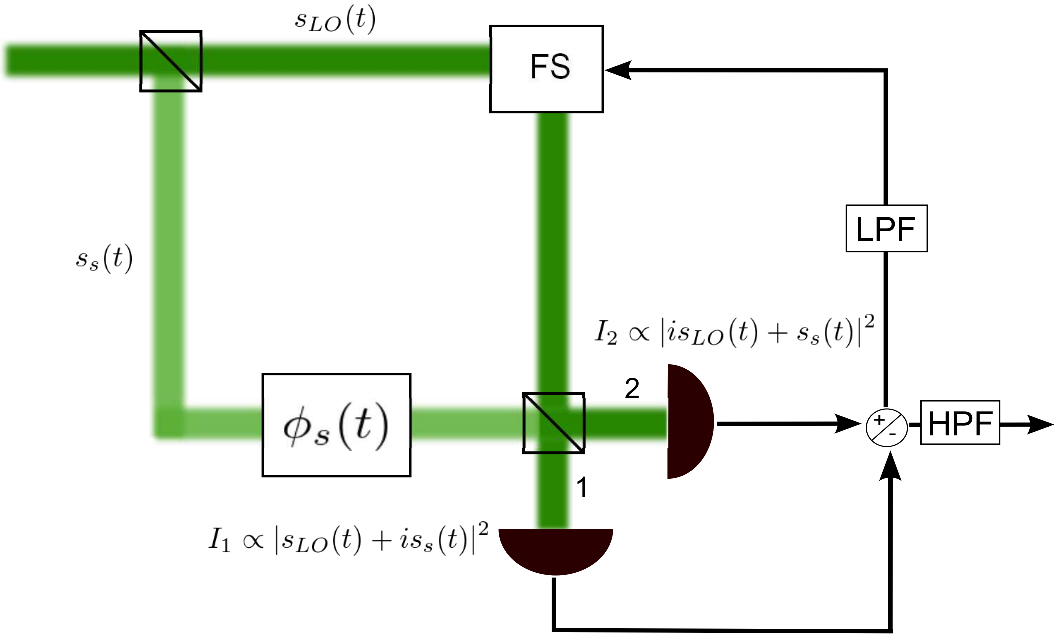

Figure 3.22: Schematic of a Mach-Zehnder interferometer which forms the basis for an optical homodyne detection scheme. A fiber stretcher (FS) is used to stabilize the relative phase between the two arms.

laser light into two paths (as shown in Figure 3.22) which may or may not have equal intensities. The path which contains the system of interest is called the signal arm, while the reference path is called the local oscillator. After passing through the optomechanical system, the signal light is recombined with the local oscillator on a 50/50 beamsplitter.

In the frame rotating at the frequency of the input laser, ω_L, the optical amplitude in the local oscillator arm is given by:

$$s_{\mathrm{LO}}(t) = s_{\mathrm{LO}} e^{i(kx_{\mathrm{LO}} + \phi_{\mathrm{LO}})} \tag{3.2}$$

and the light in the signal arm is described by:

$$s_{\mathrm{s}}(t) = s_{\mathrm{s}} e^{i(kx_{\mathrm{s}} + \phi_{\mathrm{s}}(t))}. \tag{3.3}$$

Here, s_{s} and s_{LO} have units of $\sqrt{\mathrm{photons/s}}$ such that $|s_{\mathrm{s}}|^2$ and $|s_{\mathrm{LO}}|^2$ are the rates of photons passing through the signal and local oscillator arms, respectively, k is the wavevector of the laser light, and $x_{\mathrm{LO}}, x_{\mathrm{s}}$ are the distances travelled inside each arm. We have assumed for simplicity that the field amplitudes s_{LO} and s_{s} are real (*i.e.*, that all complex information is explicity written in the phase of the field). We also assume that any time-dependent phase shifts occur as a result of the system to be measured, so we've written them into the signal field as $\phi_{\mathrm{s}}(t)$, while any time-independent phase shifts have been grouped into ϕ_{LO}. It is only the relative phase differences between the two paths that matter, so this approach is general.

The complex output amplitudes s_1, s_2 in each port of the final beamsplitter are given by

$$\begin{pmatrix} s_1 \\ s_2 \end{pmatrix} = \frac{1}{\sqrt{2}} \begin{pmatrix} 1 & i \\ i & 1 \end{pmatrix} \begin{pmatrix} s_{\mathrm{LO}}(t) \\ s_{\mathrm{s}}(t) \end{pmatrix}. \tag{3.4}$$

Ignoring a constant of proportionality, the detected intensities I at the outputs are then given by the magnitude of the field squared,

$$I_{1,2}(t) = \frac{1}{2}\left[|s_{\mathrm{s}}|^2 + |s_{\mathrm{LO}}|^2 \pm i(s^*_{\mathrm{LO}}(t)s_{\mathrm{s}}(t) - s_{\mathrm{LO}}(t)s^*_{\mathrm{s}}(t))\right]. \tag{3.5}$$

Substituting in the form of s_{LO} and s_{s} from above, we have

$$\begin{aligned} I_{1,2}(t) &= \frac{1}{2}\left[|s_{\mathrm{s}}|^2 + |s_{\mathrm{LO}}|^2 \pm i s_{\mathrm{LO}} s_{\mathrm{s}}(e^{i(k\Delta+\phi_{\mathrm{s}}(t)-\phi_{\mathrm{LO}})} - e^{-i(k\Delta x+\phi_{\mathrm{s}}(t)-\phi_{\mathrm{LO}})})\right] \\ &= \frac{1}{2}\left[|s_{\mathrm{s}}|^2 + |s_{\mathrm{LO}}|^2 \mp 2 s_{\mathrm{LO}} s_{\mathrm{s}} \sin(k\Delta x + \phi_{\mathrm{s}}(t) - \phi_{\mathrm{LO}})\right], \end{aligned} \tag{3.6}$$

where $\Delta x = x_{\mathrm{s}} - x_{\mathrm{LO}}$ is the difference in path length between the arms. The detected intensity then has a large DC component proportional to the sum of the individual intensities in each of the interferometer arms, while any time-dependent phase shifts in the signal arm will be contained in the interference term.

We can take this one step further in balancing the detection by placing detectors at both output ports of the final beamsplitter and taking the difference of their photocurrents ($I_B = I_2 - I_1$). This has the distinct advantage of eliminating the large DC term in Equation (3.6), as well as eliminating any noise which is common to both arms. For the remainder of this analysis, we will consider only the balanced configuration of the homodyne system, with the balanced current given by

$$I_B(t) = i(s^*_{\mathrm{LO}}(t)s_{\mathrm{s}}(t) - s_{\mathrm{LO}}(t)s^*_{\mathrm{s}}(t)). \tag{3.7}$$

Substituting in the form for s_{LO} and s_{s} from above, we find

$$I_B(t) = 2s_{\mathrm{LO}}s_{\mathrm{s}}\sin(\phi_{\mathrm{LO}} - k\Delta x - \phi_{\mathrm{s}}(t)). \tag{3.8}$$

Assuming that the path difference Δx remains fixed, the only time dependence in the above signal arises from phase fluctuations that occur in the system being studied. In our case, these fluctuations arise as a result of the mechanical motion of the resonator modifying the optical cavity's resonance frequency, and thus the phase of the intracavity light field. In practice, changes in the environment such as temperature fluctuations and air currents will modify the path difference Δx, but this can be compensated for by stabilizing the total relative phase $\phi_{\mathrm{LO}} - k\Delta x$ with a feedback loop, as described below.

Using a balanced homodyne detection system offers several advantages over either a direct detection scheme or an unbalanced homodyne detection scheme. The first is the ability to detect a small AC signal which might usually be difficult to detect on a large DC background. This may allow the use of much lower optical powers to probe the mechanics than are used in a direct detection scheme. The second is, for a relative phase difference between the two arms of $\phi_{\mathrm{LO}} - k\Delta x = 0$, the maximum signal (the steepest slope in the phase versus detuning curve) occurs when the laser is on-resonance. At this detuning, there should be no optomechanical backaction effects on the resonator, meaning that the measurements made are a better reflection of the intrinsic mechanical motion. The balanced homodyne scheme also eliminates any noise common to both arms, such as intrinsic laser noise. Finally, assuming that we are able to stabilize $\phi_{\mathrm{LO}} - k\Delta x$ using a feedback loop, and that we are able to tune this phase independently, we can control which quadrature (amplitude or phase) of the light is measured by changing the relative DC phase between the two arms at the output of the beamsplitter. This in turn allows control over the quadrature of the mechanics which is measured (*i.e.*, we can switch from measuring position to momentum or some other quadrature of the mechanical motion) [34].

3.5.2.3 Implementation of Balanced Homodyne Detection

A schematic of our implementation of a balanced homodyne detection system is shown in Figure 3.21(c). In our design, we use a variable coupler to split the input field into the local oscillator and signal arms, with most of the light (∼98%) passing through the local oscillator. The local oscillator arm includes a fiber stretcher (Optiphase PZ1-SMF4-APC-E) and a length of extra fiber. The signal arm contains two MEMS switches that allow us to direct the light through various paths, and the tapered fiber which is coupled to a bottle resonator during measurements. The two arms are then combined at a 50/50 four-port fiber beamsplitter (OEQuest LC-2x2-1550-50/50-FCA) with the two output ports being incident on a balanced photodiode (BPD, New Focus 1617-AC-FC).

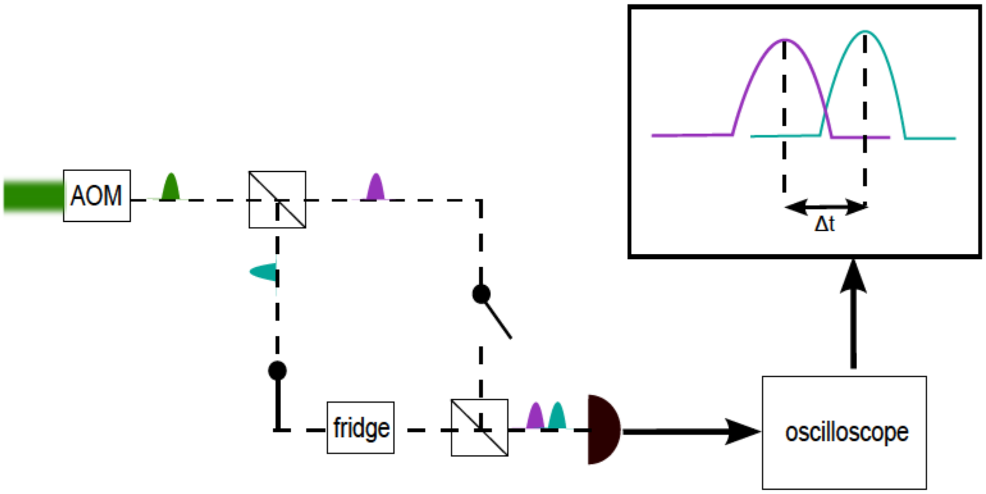

Figure 3.23: Schematic showing the time delay Δt between short optical pulses in each arm of the MZI, which is then used to calculate the path difference Δx.

As mentioned above, changes in local environmental conditions of the MZI prevent perfect matching of the two arms, but it is nonetheless important to match the path lengths of the two paths as closely as possible. To achieve this, we insert a large length of fiber (~30 m) into the local oscillator arm. We match the paths to within a few mm by successively cleaving off small lengths of the fiber until an acceptable length has been reached, at which point the extra length of fiber is fusion spliced into the optical circuit. We use two techniques to track changes in the path length as the fiber is made shorter.

The first, used at the beginning of this path-matching process, consists of creating short (~15 ns) optical pulses using an acousto-optic modulator (AOM, Gooch & Housego R15200-.2-1.59-GaP-FO-GH-FC/APC), sending them through both arms of the MZI and detecting one output of the 50/50 beamsplitter on a 125 MHz photodetector (New Focus 1811-FC). A schematic of this process is illustrated in Figure 3.23. We then observe the output of the detector on an oscilloscope. By successively blocking each arm of the interferometer, we can measure the time delay between the pulses. Using the speed of light and the approximate index of refraction of the fiber ($n_0 = 1.5$), we estimate the difference in length between the two arms, using

$$\Delta x = \frac{c}{n_0}\Delta t. \tag{3.9}$$

Once the pulses begin to overlap significantly (which occurs for $\Delta x < 30$ cm), we switch to the second method for estimating the path length difference. We scan the wavelength of the laser over a range of 1 to 10 nm and observe the resulting interference fringes. Due to the environmental noise, it is important that these scans are done quickly (at slew rates ≥10 nm/s). The frequency with which the fringes appear is directly related to the path length difference Δx through the observed transmission T_{obs}

$$T_{\text{obs}} = B \cos\left(\frac{2\pi n_0 \Delta x}{\lambda} + \phi\right) + C, \tag{3.10}$$

where B, C and ϕ are constants that can be left as free fit parameters and λ is the wavelength of the laser. Instead of fitting Equation (3.10), it is easier to calculate the path difference Δx by counting the number of fringes which occur in a given wavelength range. Assuming a small enough wavelength range that the refractive index n_0 can be approximated as constant, the number of fringes m observed between λ_1 and λ_2 is given by

$$m = n_0 \Delta x \left(\frac{1}{\lambda_1} - \frac{1}{\lambda_2}\right). \tag{3.11}$$

In practice, we start by assuming a refractive index of n_0 ∼1.5 and then proceed to cleave small pieces ($\sim 2 - 10$ cm) off the fiber before performing another wavelength scan. We keep track of both the actual cut length and the change in Δx estimated from the number of fringes to arrive at an effective index of refraction. This n_0 is then used to make the final cut of ∼2 cm, which can be done to a precision of ∼0.5 mm. At the end of the procedure, we have generally matched the path lengths to within at most a few mm, corresponding to at most a few fringes over a 10 nm scan range. Figure 3.24 shows the fringes observed for path differences of ∼4 cm and ∼400 μm.

Once the path lengths have been matched, it is then possible to stabilize the phase of the Mach-Zehnder interferometer using the fiber stretcher and a proportional-integrator (PI) servo (New Focus LB1005). The fiber stretcher consists of a length of fiber wrapped around a tube of piezoelectric material, such that the fiber is stretched or contracted with the piezo tube when a voltage is applied. The fiber stretcher used in these experiments had a voltage range of ±150 V, while the PI servo had a maximum output voltage of ±10 V, necessitating the use of a high voltage amplifier to span the range of the fiber stretcher. We use the PI servo in a feedback loop to the fiber stretcher, so that the relative phase $\phi_{\text{LO}} - k\Delta x$ (extracted from the low-pass filtered signal) remains constant despite any temperature changes or air currents.

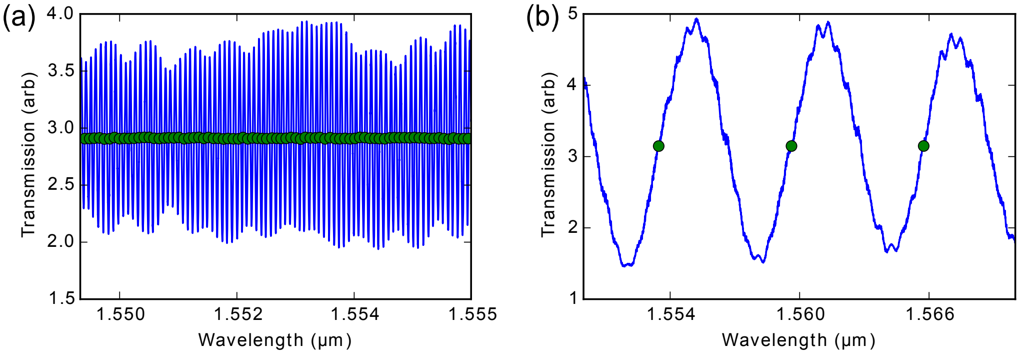

Figure 3.24: Interference fringes in the Mach-Zehnder interferometer as the wavelength of the laser is scanned. As the fiber is made shorter and the optical path difference between the local oscillator and the signal arms is reduced, fewer fringes (counted with the green circles) are seen over a larger wavelength range. (a) An optical path difference of 3.83 cm, corresponding to an actual length difference of 2.6 cm, results in 79 interference fringes over a scan range of 5 nm. (b) An optical path difference of 400 μm (length difference of 270 μm), results in three interference fringes over a scan range of 12 nm.

CHAPTER 4

Results and Discussion

In this chapter, we present the results of room temperature (Section 4.1) and low temperature (Section 4.2) optical measurements of the bottle resonators, including characterization, thermo-optical nonlinearities and an examination of the coupling conditions of the taper-resonator junction. We then describe the behaviour of the mechanical resonator at room temperature (Section 4.3.1) before moving on to measurements made in the dilution fridge (Sections 4.3.2 to 4.3.5). In order to understand these measurements, we first outline the method used to calibrate the temperature of the mechanical modes (Section 4.3.3) and then address the two main goals of this thesis: identifying suitable detection schemes at low temperatures (Section 4.3.4) and examining the behaviour of the silica bottles' breathing modes at cryogenic temperatures (Section 4.3.5).

4.1 Room Temperature Optics

4.1.1 Characterization of Resonances

As described in Chapter 3, light is coupled into bottle resonators via a tapered fiber. We characterize the optical modes of the bottles by measuring the transmission through the tapered fiber and fitting the signal with a normalized form of Equation (2.22). The bottles measured in this thesis have diameters of approximately 20 to 50 μm and exhibit intrinsic Q factors up to 10^7, as measured from fits to the optical resonances.

The Agilis nanopositioning stages in the room-temperature setup allow us to vary the bottle-taper separation and thus the coupling rate κ_{ex}. As shown in Figure 4.1, coarse scans reveal more bottle resonances as the bottle-taper distance is decreased (coupling rate increased).

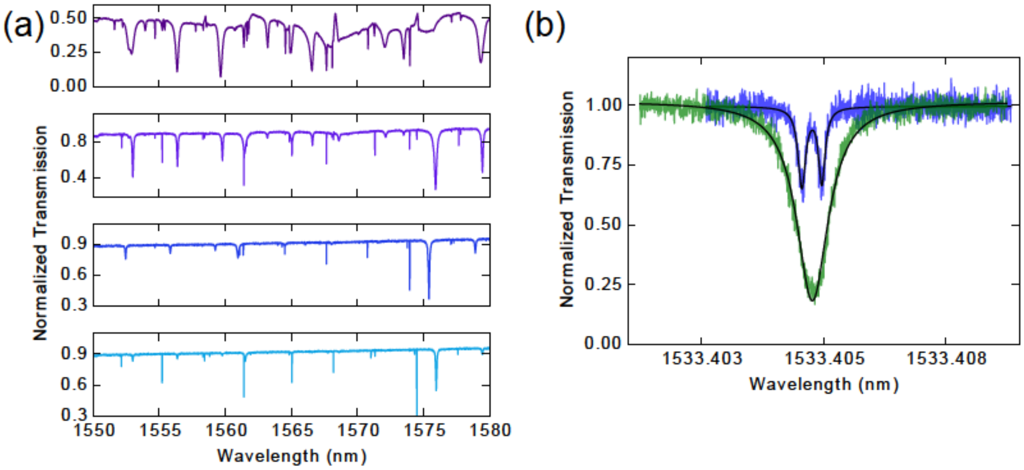

Figure 4.1: (a) Coarse scans of a bottle resonator at room temperature. As the bottle is stepped towards the tapered fiber (from the bottom panel to the top), κ_{ex} increases and more resonances are seen. In the top panel, the bottle touches the taper, significantly distorting the resonance profiles. (b) Fine scans of a bottle resonance as the bottle is moved towards the taper; κ_{ex} increases, obscuring the splitting of the doublet resonance (blue is greater bottle-taper separation, green is smaller).

These coarse scans are normalized to the transmission of laser light through the taper when the bottle is uncoupled to the taper. Off-resonant transmission is slightly lower than unity in Figure 4.1(a) due to scattering of the light from the taper, which is negligible for well phase-matched tapers. As shown in the top panel of Figure 4.1(a), eventually the bottle and taper touch, at which point the off-resonant transmission drastically decreases as scattering out of the taper and away from the bottle becomes significant. The optical mode profiles are also dramatically altered and their Q factors reduced. In our experiments, we prefer the bottle and taper not to make contact since this damps the mechanical oscillations of the bottle, along with degrading the optics.

If we examine individual optical modes of the bottles, we observe a broadening of the resonance corresponding to the increase in κ_{ex}, shown in Figure 4.1(b). Here we normalize the transmission not to the uncoupled value but to the off-resonant transmission, such that we have neglected scattering of light from the taper, which is broadband and does not contribute to the optical linewidth κ. At larger bottle-taper separations, some resonances exhibit a doublet character. This arises from a hybridization of two nominally degenerate, counter-propagating modes in the bottle (corresponding to light circulating clockwise or counter-clockwise). For single-sided optical cavities such as the bottles studied here (their single-sided nature was confirmed by reflection measurements not shown here), the direction of light propagation in the taper would usually select only one of these modes. However, when significant scattering of photons into the other mode takes place, the degeneracy is split, with the magnitude of this splitting determined by the scattering rate between the modes. This effect can be exploited to generate reflection from the normally transmitting resonator [141]. As the bottle is approached to the taper, κ_{ex} becomes much larger than the mode splitting, such that the doublet structure can no longer be resolved (Figure 4.1(b)). In making the above measurements, we optimize the polarization in the tapered fiber for coupling to the optical resonance by adjusting the FPCs. This maximizes κ_{ex} for a particular resonance through polarization mode-matching between the taper and bottle.

In some instances, usually after a tapered fiber has been housed in the room temperature chamber for a long period of time (several months), it becomes much less efficient (dropping from >90% efficiency to <5%). In these instances, we observe not only dips in the transmission, corresponding to coupling of the light to optical resonances, but also peaks and asymmetric profiles. Upon closer inspection, all of these features are optical resonances, with shapes that change according to the polarization of the injected light. Figure 4.2(a) shows the observed resonances as the polarization of light in the taper is varied using the FPCs. Figure 4.2(b) shows the observed coarse transmission for the different polarizations.

If we look also at transmission through the taper when it is uncoupled to a bottle (Figure 4.2(c)), we see that it exhibits polarization-dependent features as well. The transmission through the taper shows polarization-dependent oscillations as a function of wavlength, which appear only after this loss in efficiency. Since the measurement fiber is single-mode and polarization-insensitive on either side of the taper, we believe that the oscillations arise from some sort of polarization-dependent loss mechanism in the tapered region.

These observations can be explained in the context of Fano resonances [142] which were first observed in atomic systems as an interference between the discrete resonance states of the atoms and a continuum of modes. In Figure 4.2, we believe we are seeing the interference between a continuum of polarization-dependent taper modes and the spectrally sharp optical resonances of the bottle. In his 1961 work on atomic He, Fano noticed that the shape of the observed resonances seemed to vary with the relative transition rates to the discrete and continuum states, which he quantified through a parameter q [143]. This is illustrated in Figure 4.2(d), where different values of q give rise to very different shapes of the resonance. In our experiment, the role of q is played by the polarization of the injected light.

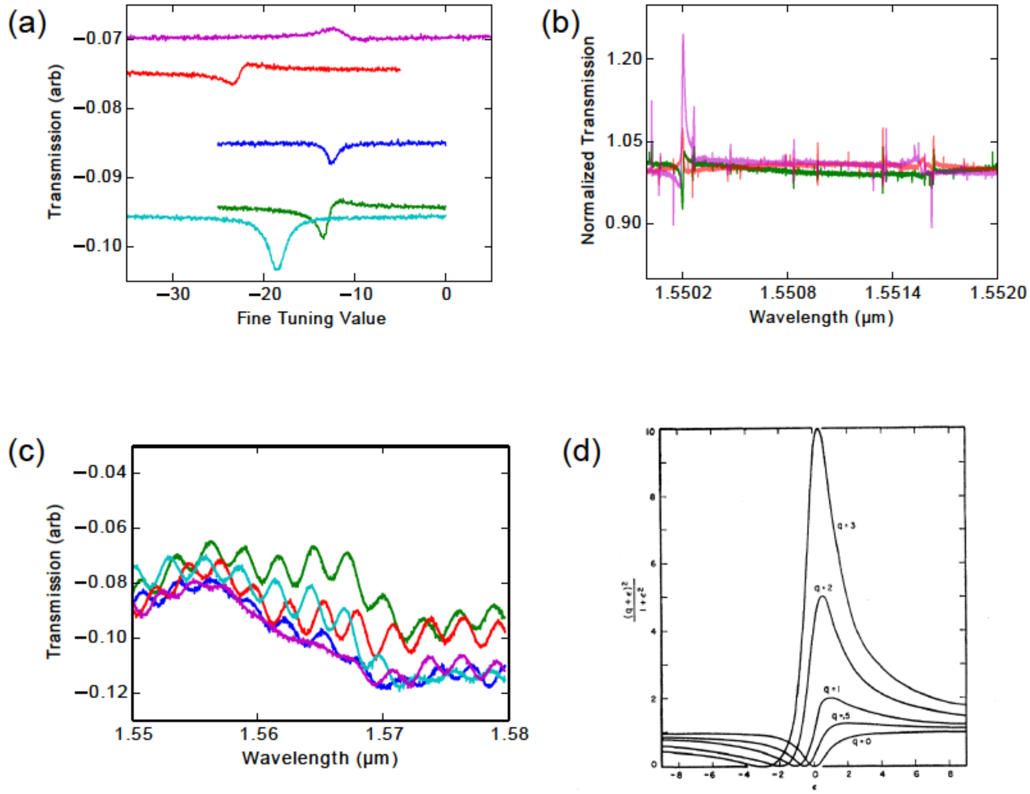

Figure 4.2: (a) Fine scans of a single optical resonance, (b) coarse scans incorporating a number of resonances and (c) coarse scans of the laser transmission through the taper when uncoupled from the bottle resonators at a number of different input polarizations. The transmission in (b) is normalized to that in (c). Each colour represents a different input polarization. The lineshapes of the resonances vary considerably, which we attribute to an interference between polarization-dependent modes in the taper and the discrete bottle modes, similar to Fano resonances. (d) Fano interference in atomic He, with qualitatively different lineshapes for different values of the parameter q, analogous to our observations when varying the polarization. (d) reprinted with permission from [U. Fano. Effects of Configuration and Interaction on Intensities and Phase Shifts. *Physical Review*, 124(6):1866, 1961]. Copyright 1961 by the American Physical Society.

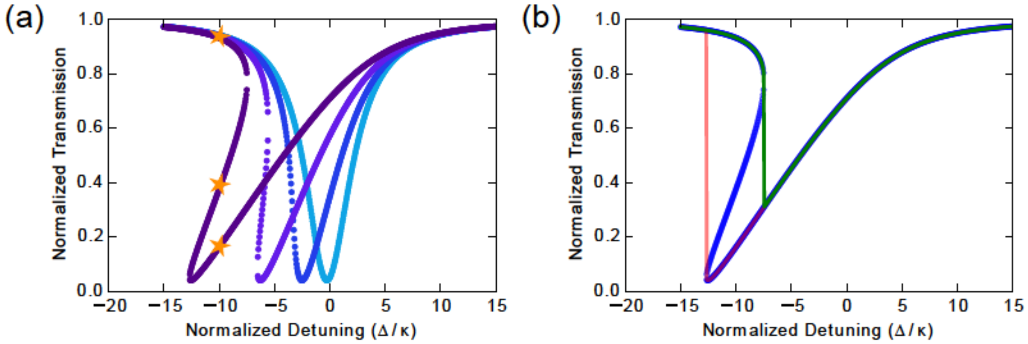

Figure 4.3: (a) Shape of the optical resonance simulated by taking all real solutions of Equation (4.5) for increasing injected powers (0.1, 1, 2.5 and 5 μW) and a nonlinear parameter of $\Delta_{\mathrm{nl}}/2\pi = 8 \times 10^{-6}$ Hz. The stars denote the three real solutions at a detuning $\Delta/\kappa \sim -10$ for $P = 5$ μW. (b) Hysteresis between scanning the laser forward (green) and backwards (red) in detuning across a nonlinear optical resonance.

4.1.2 Thermo-Optical Nonlinearities

As the optical power injected into the resonator is increased, we observe a shift in the resonance frequency due to absorption of laser light into the material. This absorption causes an increase in the temperature of the silica, leading to variations in both the refractive index (through the thermorefractive effect) and the physical dimensions (via the thermal expansion coefficient) of the resonator [57, 75, 81, 144]. These effects manifest themselves in a qualitatively different spectral lineshape (shown in Figure 4.3) of the resonance as a laser is tuned across the cavity. Although the absorption of telecom band light is usually quite low in silica (typical loss rates are on the order of 0.2 dB/km for the SMF-28e fiber used in our experiments at room temperature), the high-quality nature of these resonators means that photons circulate for long periods of time inside the cavity (on the order of 1-100 ns in the bottles studied here) and large optical fields are built up, enhancing the optical absorption. We note that, in principle, the large circulating optical fields would also enhance the effects of the nonlinear optical Kerr effect but thermal effects dominate for the conditions in these experiments. The Kerr effect can be observed if the thermal effects are reduced, for example, by immersing the resonator in a liquid helium bath [82].

To understand the effects of the thermo-optical nonlinearity, recall the resonance condition of Equation (2.12):

$$\lambda_{\mathrm{o}} = \frac{2\pi R c_1 n_0}{l}. \tag{4.1}$$

Here λ_o is the resonant wavelength in the absence of any thermal perturbations to the resonator, and n_0 is the refractive index at the equilibrium temperature. Expanding n_0 as a Taylor series in the temperature difference ΔT to account for the thermorefractive effect and incorporating the thermal expansion coefficient ϵ (which increases R), we can rewrite Equation (4.1) as

$$\begin{aligned}\lambda(\Delta T) &= \frac{2\pi c_1 R(1+\epsilon\Delta T)(n_0 + \frac{dn_0}{dT}\Delta T + \cdots)}{l} \\ &= \lambda_\mathrm{o}(1+\epsilon\Delta T)\left(1 + \frac{1}{n_0}\frac{dn_0}{dT}\Delta T + \cdots\right). \qquad (4.2)\end{aligned}$$

At room temperature, it is sufficient to keep only terms to first order in ΔT [75], resulting in

$$\lambda(\Delta T) \simeq \lambda_\mathrm{o}(1 + b_1(T)\Delta T) \qquad (4.3)$$

where $b_1(T) = \epsilon(T) + \frac{1}{n_0}\frac{dn_0}{dT}$ can be approximated as constant for small ΔT. We can equivalently describe these phenomena in frequency space, resulting in

$$\omega(\Delta T) \simeq \omega_\mathrm{o}(1 - b_1(T)\Delta T). \qquad (4.4)$$

From the above equation, we can define a renormalized detuning $\Delta \rightarrow \Delta + \omega_\mathrm{o} b_1(T)\Delta T = \Delta + \Delta_\mathrm{nl} n_\mathrm{cav}$ which includes thermo-optical nonlinearities to first order and makes the assumption that $n_\mathrm{cav} \propto \Delta T$ [85, 145]. Δ_nl can be interpreted as the shift in the resonance frequency ω_o per photon circulating in the cavity. We can then rewrite Equation (4.1) as

$$n_\mathrm{cav} = \frac{\kappa_\mathrm{ex}}{\frac{\kappa^2}{4} + (\Delta + \Delta_\mathrm{nl} n_\mathrm{cav})^2}|s_\mathrm{in}|^2. \qquad (4.5)$$

Equation (4.5) is cubic in n_cav so at high powers (where n_cav is large and many photons are absorbed), it describes a bistable resonance. At certain detunings, up to three real solutions exist, giving rise to hysteresis in the optical spectrum, between when a laser is scanned forward (from negative to positive Δ) and in reverse (from positive to negative Δ) over the resonance, as illustrated in Figure 4.3(b). Equation (4.5) can be solved analytically or numerically to fit these nonlinear optical resonances using Δ_nl as a fit parameter, as done in Ref. 85 and Ref. 145.

At room temperature, we begin to observe this nonlinear behaviour at relatively low injected optical powers (<1 μW). As shown in Figure 4.4, we fit these nonlinear resonances by

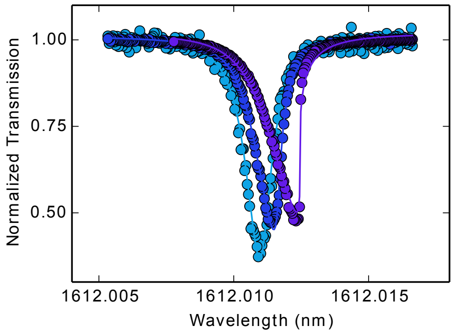

Figure 4.4: Nonlinear behaviour of a bottle optical resonance at room temperature. Solid lines are fits with Equation (4.5), yielding a nonlinear parameter $\Delta_{\mathrm{nl}}/2\pi \simeq 2.4 \times 10^{-6}$ Hz. Injected optical powers are 0.73, 1.9 and 4.0 μW (from light blue to dark purple, corresponding to peak photon numbers of 6.6×10^4, 1.2×10^5 and 2.6×10^5, respectively).

solving Equation (4.5) exactly using the cubic equation and choosing the appropriate real solution, depending on the scanning direction of the laser. In this case, the laser is scanned forwards in detuning (from longer to shorter wavelengths). The fitted nonlinear parameter $\Delta_{\mathrm{nl}}/2\pi \simeq 2.4 \times 10^{-6}$ Hz is positive, and the bistability occurs on the red (longer wavelength) side of the resonance.

4.1.3 Measurements at 780 nm

Since silica is transparent to both near-infrared and visible light, one interesting property of the bottles is that they can be used as optical resonators at many different wavelengths. This can be exploited, for instance, to convert photons from one wavelength to another using optomechanically induced transparency [40, 41, 42]. In particular, the 780 nm band is interesting for biological sensing applications due to the reduced absorption of photons in water when compared to the telecom band [67, 69].

We investigated optical modes of the bottle resonators around 780 nm, first using a standard fiber tapered for single mode use at 1550 nm. We were able to excite some resonances using 780 nm light injected into this taper but found that to do so, the taper contacted the surface of the bottle, degrading the optical resonances. To remedy this issue, we tapered a 1550 nm single mode fiber to a ~500 nm diameter by continuing to pull the fiber past the single-mode onset shown in Figure 3.2. At this diameter, the tapered region should be single mode for 780 nm light clad by air (see Table 2.1), and the larger evanescent field enables coupling to optical modes without touching the bottle. As shown in Figure 4.5, we observed

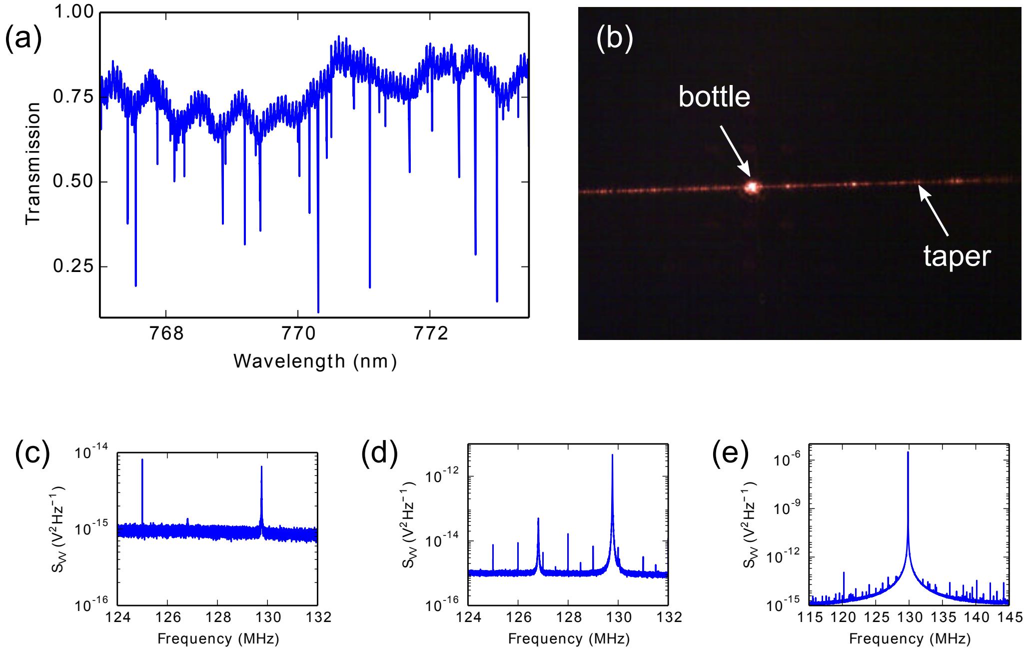

Figure 4.5: (a) Optical resonances of the bottle resonator around 780 nm. (b) The inefficient taper used for probing the bottle scatters light, and the bottle resonances are visibly illuminated. (c-e) Mechanical resonances of the bottle resonator at 126 and 129 MHz, for increasing injected optical powers (0.2, 1.3 and 2.7 mW). In contrast to the 126 MHz mode, we see a significant increase in the amplitude of S_{VV} at 129 MHz, as well as (we suspect) the Q_{m}. The laser noise (seen as additional peaks in the spectrum) prevalent in (e) prevented confirmation of this.

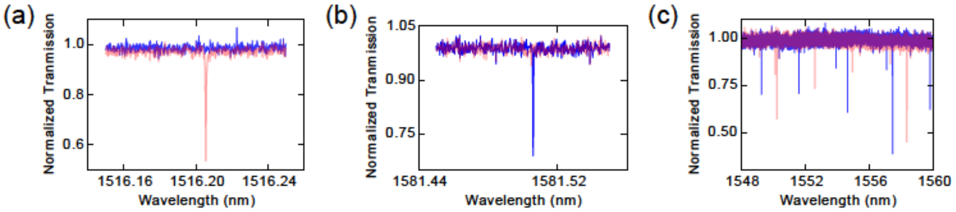

Figure 4.6: When the polarization is optimized for coupling to the 1516 nm resonance (light red), the 1581 nm resonance disappears. The opposite occurs when the polarization is optimized for the 1581 nm resonance (dark blue). The 1516 nm (a) and 1581 nm (b) resonances for the two different polarizations. (c) The coarse spectrum of optical modes exhibits different families of modes for each polarization.

a number of optical modes in the bottle, but found that the fiber was extremely lossy (as can be seen from the red light scattering into the camera). Improvements in pulling tapered fibers for 780 nm light have since been made using optical fiber which is single mode for 780 nm [67]. Regardless, we were able to resolve mechanical modes of the bottle in the high-pass filtered transmission signal. As the optical power is increased (Figure 4.5(c-e)), we suspect that significant negative optomechanical damping takes place (as per Equation (2.64)), leading to a drastic increase in the mechanical Q factor. This is typical of self-sustained oscillations occuring in parametrically coupled systems when the total damping rate reaches zero [11, 107, 146, 147]. We suspect that these are more readily observed at 780 nm than at 1550 nm because the photons carry twice as much energy. Due to significant high-frequency noise in the 780 nm laser system, the mechanical spectra could not be fit and thus we could not confirm this observation.

4.2 Low Temperature Optics

For most of the low temperature mechanical measurements presented in this chapter, the same bottle resonator was used. Within the context of this resonator, we concentrated on two separate high-quality optical modes, at 1516 nm and 1581 nm, which were spectrally separated from one another, and orthogonally polarized, as shown in Figure 4.6. When the polarization was optimized for the 1516 nm resonance (shown in red), the 1581 nm resonance disappeared, and vice-versa (shown in blue). Coarse scans also reveal separate families of resonances for each polarization.

Inside the dilution fridge, we see no obvious changes in the structure of the resonances, with unloaded Q_{opt} of $\sim 10^7$ (*i.e.*, ω_o/κ_0) and loaded Q_{opt} (including κ_{ex}) of 10^5-10^7, depending on the coupling conditions. There is a shift in the resonance frequency of individual modes as

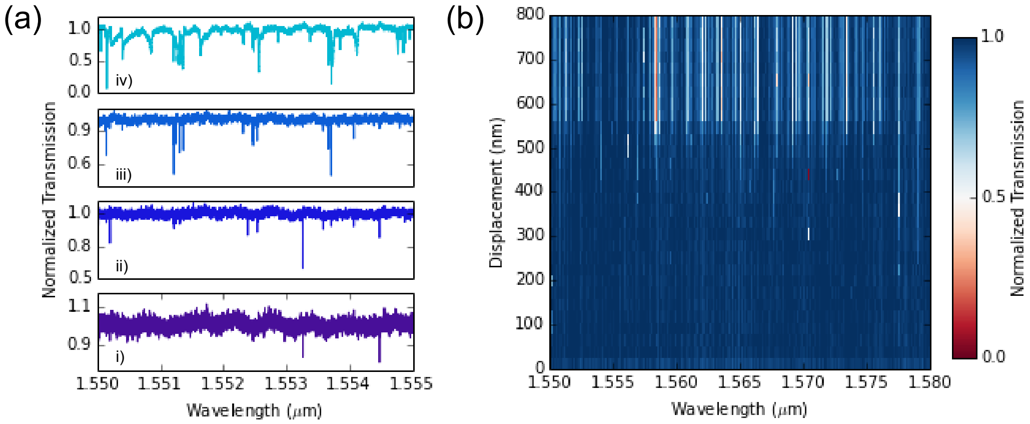

Figure 4.7: Coarse scans of the bottle resonances, as the taper-bottle separation is decreased using the attocube's continuous voltage offset. (a) shows traces from (b) at i) 0, ii) 133, iii) 320 and iv) 750 nm. The discontinuity in (b) at ∼550 nm is indicative of the bottle contacting the taper.

the temperature of the fridge is lowered, but the cooldown process occurs much too quickly to track these changes. The attocubes used in the dilution fridge apparatus do, however, allow us to control the coupling conditions more sensitively than at room temperature, thanks to the reduced minimum step size and the continuous voltage offset. Figure 4.7 shows coarse scans of the bottle resonator as the distance between the taper and bottle is varied using the continuous piezo of the attocube. The discontinuity around 550 nm in Figure 4.7(b) is indicative of the taper touching the bottle resonator.

4.2.1 Taper-Bottle Coupling Conditions

We next demonstrate the versatility of our system in achieving critical coupling, as shown in Figure 4.8. The attocube piezo is extended over its full range of 800 nm (at 4.2 K), moving the bottle from the under-coupled (far away from the taper) to the over-coupled regime. As shown in Figure 4.8(b), critical coupling occurs at a displacement of ∼375 nm when the two solutions to Equation (2.25), $\kappa_\pm$, are equal (or equivalently $\kappa_{\mathrm{ex}} = \kappa_0$). At larger separations, $\kappa_- = \kappa_{\mathrm{ex}}$ and $\kappa_+ = \kappa_0$, while for separations <375 nm, $\kappa_+ = \kappa_{\mathrm{ex}}$ and $\kappa_- = \kappa_0$. Considering this crossover, it is apparent that κ_0 remains constant, while κ_{ex} increases exponentially as the separation is decreased. This exponential trend arises from increasing overlap between the taper mode and the bottle's evanescent field, both of which decay exponentially in space [73]. We can quantify the quality of mode-, polarization- and phase-matching in the system through the on-resonance extinction of the transmission [84]. As shown in Figure 4.8(c),

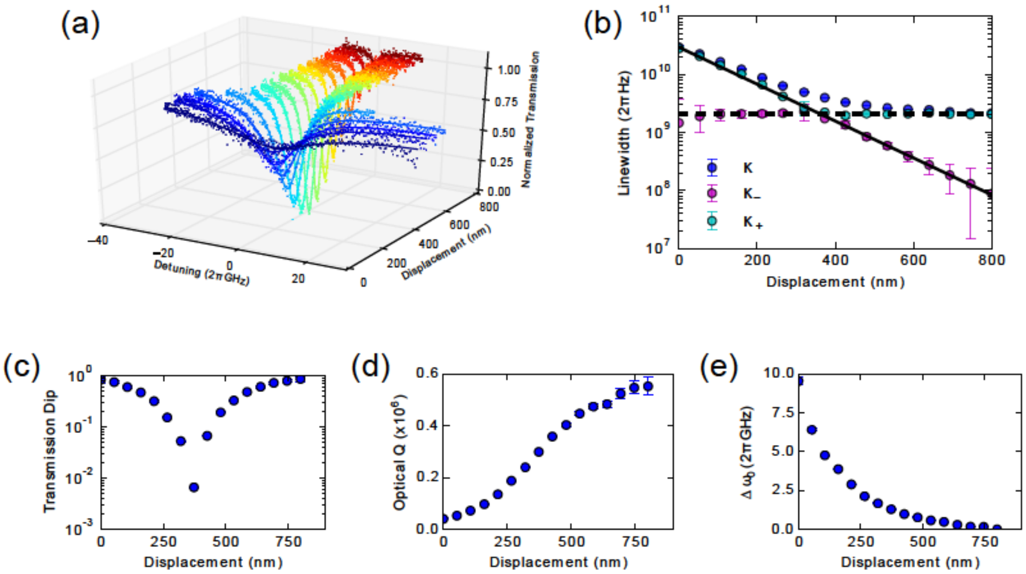

Figure 4.8: (a) Taper transmission across the optical resonance as the bottle-taper separation is decreased at 4.2 K. Solid lines are fits of the data to the Lorentzian profile of Equation (2.22). (b) Decay rates are measured from fits to (a). $\kappa_{\pm}$ are the two solutions to Equation (2.25) and κ is the total measured decay rate. The solid line denotes κ_{ex} while the dashed line shows κ_0. On-resonance transmission minimum (c), Q_{opt} (d) and change in resonance frequency ω_{o} (e). Panels (a) and (c) reprinted with permission from [A. J. R. MacDonald, G. G. Popowich, B. D. Hauer, P. H. Kim, A. Fredrick, X. Rojas, P. Doolin, and J. P. Davis. Optical microscope and tapered fiber coupling apparatus for a dilution refrigerator. *Review of Scientific Instruments*, 86(1):013107, 2015]. Copyright 2015, AIP Publishing LLC.

we reach an on-resonance transmission minimum of -22 dB at critical coupling [47], which is comparable with similar room temperature systems [84] and exceeds low temperature coupling systems [92]. Figure 4.8(d) and (e) show the decrease in the resonance quality factor and increase in the optical resonance frequency, respectively. The change in Q_{opt} is simply a consequence of the increase in κ_{ex}, while ω_{o} reflects a change in the effective index of refraction of the bottle mode as the silica of the taper is increasingly sensed by the evanescent field of the bottle (which modifies the constant c_1 in Equation (2.12)).

For these measurements, the polarization of the injected light was optimized for overlap with the measured optical mode. If the polarization of the taper mode is not perfectly matched with that of the bottle mode, we observe an avoided crossing in κ_- and κ_+, shown in Figure 4.9. Although the resonator still progresses from the under- to the over-coupled regime as the separation is decreased, there is no point of critical coupling where the two decay rates

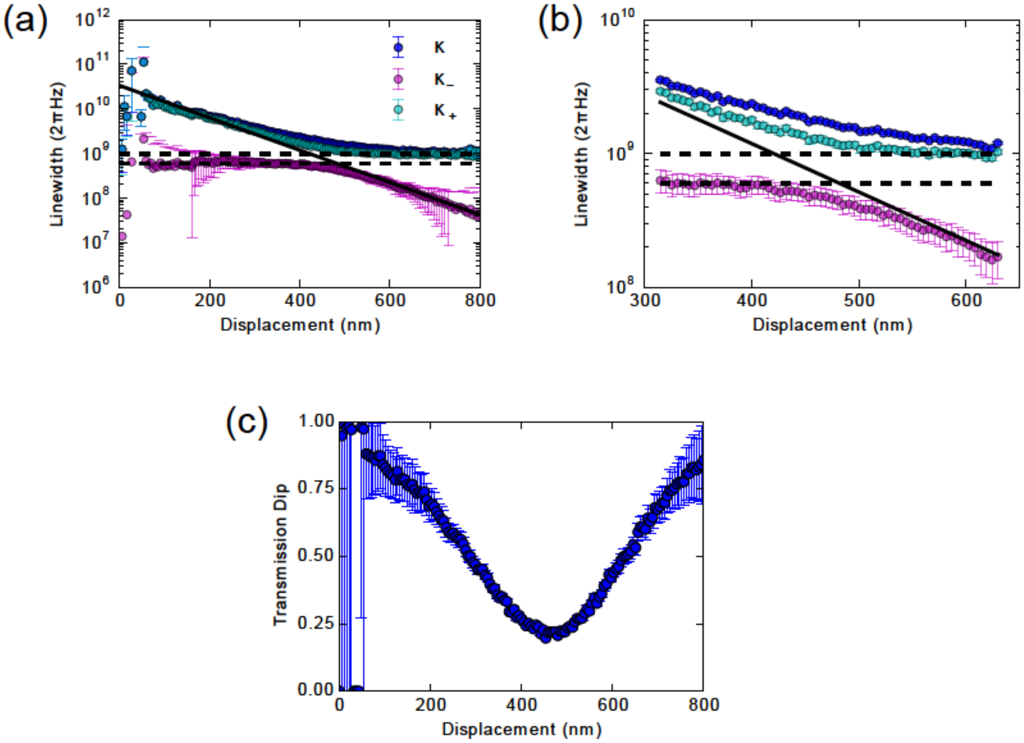

Figure 4.9: (a) Avoided crossing in $\kappa_\pm$ due to imperfect polarization-matching of the taper and bottle modes. Solid line indicates κ_{ex} while the dashed lines are estimates of κ_0 in the under- (upper dashed line) and over-coupled (lower) regimes. (b) Zoomed-in view of the avoided crossing, showing that κ_0 is decreased in the over-coupled regime. (c) The on-resonance transmission dip reaches only ~0.2 at the point closest to critical coupling.

are matched. In fact, κ_0 decreases slightly between the under- and over-coupled regimes, indicating that the bottle becomes less lossy internally. In Figure 4.9(b), we see that even at the point where κ_{ex} and κ_0 are most closely matched, the normalized transmission reaches a minimum of only ~0.2.

The measurements shown in Figures 4.8 and 4.9 were conducted during an earlier experimental run with a different fiber and bottle. When we repeated these coupling measurements with the new fiber-bottle system, we observe different trends, as depicted in Figure 4.10. We were not able to achieve critical coupling and in fact, did not even see the characteristic avoided crossing pictured in Figure 4.9. Instead we note that both κ_{ex} and κ_0 increase as the taper-bottle separation is reduced. We hypothesize that this happens because the bottle couples to the taper at a point on the fiber which is thicker than the taper waist, as differential thermal contractions in the fridge shifted the taper away from the bottle during cooldown (a fourth attocube has since been added to the system to remedy this issue). Light circulating in the bottle mode can scatter off the surface of the fiber without coupling back into the outgoing optical field, making this an intrinsic decay mechanism. Figure 4.10 shows that κ_0 (κ_+ in the legend, since the resonator begins in the under-coupled state) is constant at large taper-bottle separations but increases along with κ_{ex} as the bottle is brought closer to the taper. At low temperatures (Figure 4.10(a) and (b)), it seems that the resonator remains in the undercoupled regime. Once the fridge is warmed up (Figure 4.10(c) and (d)), it is unclear whether the resonator transitions to the over-coupled regime (around 450 nm) before the scattering causes κ_0 and κ_{ex} to increase, as there may be an avoided crossing similar to that in Figure 4.9.

We also observe an interesting trend in the resonance frequency of the optical mode in Figure 4.10(b) and (d). At low temperature, the frequency decreases monotonically, in contrast with Figure 4.8(e), while at room temperature, the frequency first increases and then decreases. We do not understand this effect yet, but it seems intimately related to the coupling conditions of the resonator, since the turnaround point occurs at the same separation as the possible transition to over-coupling in (c).

4.2.2 Thermo-Optical Nonlinearities

At low temperatures, it is no longer sufficient to consider only terms of $\mathcal{O}(\Delta T)$ in Equation (4.2). Below ~15 K, the sign of the first order thermorefractive effect ($\frac{dn_0}{dT}$) changes [81, 110]. Thus the curvature, and hence the second derivative, of the refractive index becomes non-negligible. We account for this by including the $\frac{d^2n_0}{dT^2}$ term in the Taylor series expansion of n_0, and keep all terms of $\mathcal{O}(\Delta T^2)$. At very low temperatures, the thermal expansion coefficient of silica can also no longer be approximated as linear in temperature [148], so we include a term of the form $\epsilon^{(2)}\Delta T^2$. The resonance condition then becomes

$$\lambda(\Delta T) = \lambda_{\mathrm{o}}(1+\epsilon\Delta T+\epsilon^{(2)}\Delta T^2)\left(1+\frac{1}{n_0}\frac{dn_0}{dT}\Delta T+\frac{1}{2n_0}\frac{d^2n_0}{dT^2}\Delta T^2\right), \tag{4.6}$$

which when translated into frequency and expanded is

$$\begin{aligned}\omega(\Delta T) &\simeq \omega_{\mathrm{o}}\left(1-\left[\epsilon+\frac{1}{n_0}\frac{dn_0}{dT}\right]\Delta T+\left[\frac{\epsilon}{n_0}\frac{dn_0}{dT}+\epsilon^2+\epsilon^{(2)}+\frac{1}{n_0^2}\left(\frac{dn_0}{dT}\right)^2-\frac{1}{2n_0}\frac{d^2n_0}{dT^2}\right]\Delta T^2\right)\\ &\equiv \omega_{\mathrm{o}}(1-b_1(T)\Delta T+b_2(T)\Delta T^2).\end{aligned} \tag{4.7}$$

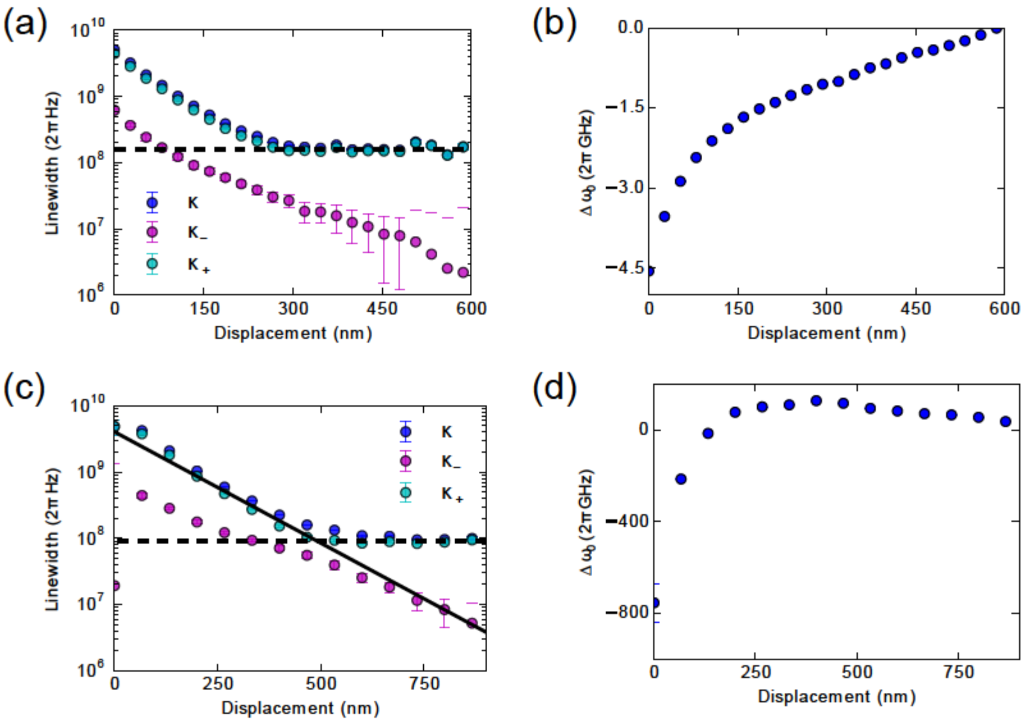

Figure 4.10: (a) Both κ_{ex} and κ_0 increase as the bottle-taper separation is decreased at 9 mK. The bottle appears to remain under-coupled throughout the measurement. Dashed line shows the initial value for κ_0. (b) In contrast to Figure 4.8(e), the optical resonance frequency decreases with decreasing bottle-taper separation. (c) Even after the fridge is warmed up to room temperature, we do not observe the clear avoided crossing between κ_+ and κ_- as in Figure 4.9, but there is evidence of a possible transition from the under- to over-coupled regime around 450 nm. Solid line indicates an estimate of κ_{ex} while the dashed line shows the initial value of κ_0. (d) We see first an increase in the optical resonance frequency as in Figure 4.8(e), followed by a decrease beginning around 450 nm. This turning point appears correlated to the possible transition from under- to over-coupling in (c).

As was done at room temperature, we can again include the terms proportional to $b_1(T) = \epsilon(T) + \frac{1}{n_0}\frac{dn_0}{dT}$ and $b_2(T) = \frac{\epsilon(T)}{n_0}\frac{dn_0}{dT} + \epsilon^2(T) + \epsilon^{(2)}(T) + \frac{1}{n_0^2}\left(\frac{dn_0}{dT}\right)^2 - \frac{1}{2n_0}\frac{d^2 n_0}{dT^2}$ in a renormalized detuning, $\Delta \to \Delta + \Delta_{\mathrm{nl}} n_{\mathrm{cav}} + \Delta_{\mathrm{nl}}^{(2)} n_{\mathrm{cav}}^2$, giving

$$n_{\mathrm{cav}} = \frac{\kappa_{\mathrm{ex}}}{\frac{\kappa^2}{4} + \left(\Delta + \Delta_{\mathrm{nl}} n_{\mathrm{cav}} + \Delta_{\mathrm{nl}}^{(2)} n_{\mathrm{cav}}^2\right)^2} |s_{\mathrm{in}}|^2. \tag{4.8}$$

We see that the resonance is now a quintic polynomial in n_{cav} which cannot be solved analytically. Instead, the resonances can be fit numerically by varying the parameters Δ_{nl} and $\Delta_{\mathrm{nl}}^{(2)}$.

The form of Equation (4.8) gives rise to a tristable resonance, as observed in Ref. 110. Simulations of this resonance shape and the hysteresis in forward and reverse scans of the resonance are illustrated in Figure 4.11. We note that the relative sign and magnitude of $\Delta_{\mathrm{nl}} n_{\mathrm{cav}}$ and $\Delta_{\mathrm{nl}}^{(2)} n_{\mathrm{cav}}^2$ are both important in determining the particular shape of the resonance. We assume that Δ_{nl} and $\Delta_{\mathrm{nl}}^{(2)}$ have opposite signs, since this is the most interesting regime and that which we observe in our experiments. As seen in Figure 4.11(a), for sufficiently low optical powers the resonance appears linear, as n_{cav} is so small that both $\Delta_{\mathrm{nl}} n_{\mathrm{cav}}$ and $\Delta_{\mathrm{nl}}^{(2)} n_{\mathrm{cav}}^2$ can be neglected. As the power is increased, $\Delta_{\mathrm{nl}} n_{\mathrm{cav}}$ becomes non-negligible, and we see the the lineshape trends towards a bistability on one side of the resonance. However, as n_{cav} is further increased, the magnitude of $\Delta_{\mathrm{nl}}^{(2)} n_{\mathrm{cav}}^2$ increases rapidly, and competition between $\Delta_{\mathrm{nl}} n_{\mathrm{cav}}$ and $\Delta_{\mathrm{nl}}^{(2)} n_{\mathrm{cav}}^2$ causes the resonance to bend in the opposite direction. For even higher optical power $\Delta_{\mathrm{nl}}^{(2)} n_{\mathrm{cav}}^2$ quickly overpowers $\Delta_{\mathrm{nl}} n_{\mathrm{cav}}$ since it scales with the square of the injected power.

Experimentally, we observe three regimes of nonlinear behaviour in the fridge. These regimes are governed by the presence of exchange gas in the IVC, which controls how well the heat generated by absorbed light is transferred to the environment via convection, which is the bottle's primary method of heat transfer, and thus the proportionality between n_{cav} and ΔT. At very high exchange gas pressures, we observe nonlinear behaviour similar to that seen at room temperature, shown in Figure 4.12. We fit these resonances with Equation (4.5) to determine the parameter $\Delta_{\mathrm{nl}}/2\pi = -3 \times 10^{-7}$ Hz. Note that here Δ_{nl} is negative, in contrast to the situation at room temperature, where it was positive. This is consistent with the change in sign of the thermorefractive effect observed in Ref. 81 and Ref. 110, and we see that the the bistability occurs on the blue side of the resonance, instead of the red side.

A second regime occurs when the IVC is completely evacuated. Similar behaviour results when the fridge is at 4.2 K, and when it is operating at the base temperature of 9 mK, shown in Figures 4.13 and 4.14, respectively. Under these conditions, the resonance again exhibits

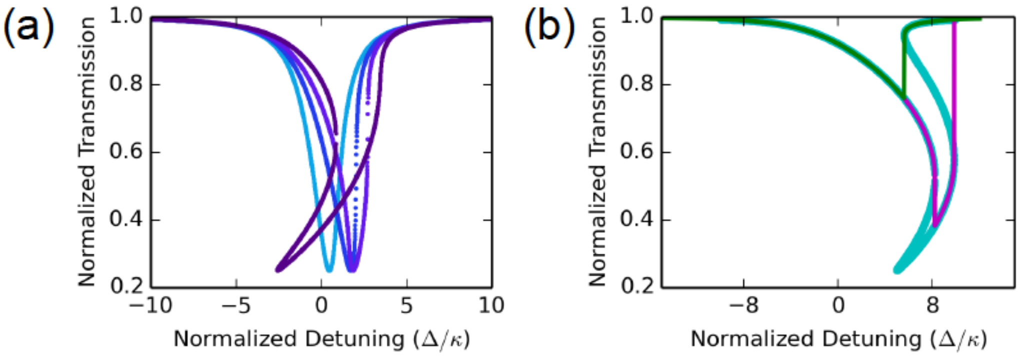

Figure 4.11: (a) Optical resonances with $\kappa/2\pi = 20$ MHz and $\kappa_{\mathrm{ex}}/2\pi = 5$ MHz simulated ny the real solutions of Equation (4.8) for increasing optical powers for $\Delta_{\mathrm{nl}}/2\pi = -8 \times 10^{-6}$ Hz and $\Delta_{\mathrm{nl}}^{(2)}/2\pi = 1.6 \times 10^{-18}$ Hz. (b) Extreme case for $\Delta_{\mathrm{nl}}/2\pi = -1$ Hz and $\Delta_{\mathrm{nl}}^{(2)}/2\pi = 2.5 \times 10^{-9}$ Hz at an input power of 5 mW, showing five real solutions to Equation (4.8) at some detunings as well as hysteresis between the forward (pink) and reverse (green) optical scans.

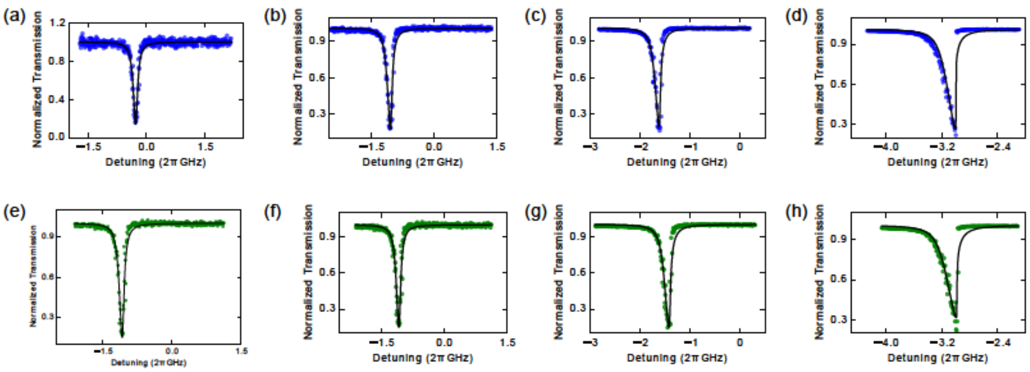

Figure 4.12: Forward (blue) and reverse (green) scans of the laser across an optical resonance at 4.2 K, when the bottles are immersed in helium exchange gas. Injected optical powers of 0.48 (a, e), 1.8 (b, f), 5.4 (c, g), and 18.4 (d, h) μW, corresponding to peak photon numbers of 4.3×10^4 (a), 3.8×10^4 (e), 1.4×10^5 (b,f), 4.3×10^5 (c,g) and 1.5×10^6 (d,h). Fits to the data using Equation (4.5) reveal a nonlinear detuning parameter $\Delta_{\mathrm{nl}}/2\pi = -3 \times 10^{-7}$ Hz.

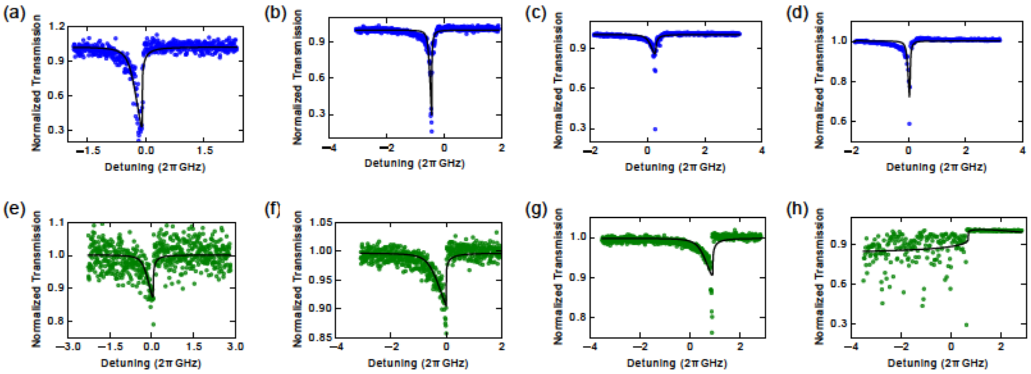

Figure 4.13: As in Figure 4.12 under vacuum at 4.2 K. Injected powers of 0.36 (a, e), 1.2 (b, f), 3.0 (c, g) and 4.8 (d, h) μW, corresponding to peak photon number 1.2×10^4 (a), 4.1×10^4 (b), 1.0×10^5 (c), 9.3×10^4 (d), 1.7×10^3 (e), 8.7×10^3 (f), 3.6×10^4 (g) and 2.3×10^4 (h). Fits to the data using Equation (4.5) reveal $\Delta_{\rm nl}/2\pi \sim -2 \times 10^{-6}$ Hz.

nonlinear optical behaviour that can be adequately described by the cubic in Equation (4.5). The bistability continues to occur on the blue side of the resonance and, although the resonances are more difficult to fit (note that the fits failed in Figures 4.13(h) and 4.14(f)), we extract $\Delta_{\rm nl}/2\pi \sim -2 \times 10^{-6}$ at 4.2 K, and $\Delta_{\rm nl}/2\pi \sim -3 \times 10^{-6}$ at 9 mK. We note that this is 10 times larger than the $\Delta_{\rm nl}$ for high exchange gas pressures, since the bottles are much more efficiently cooled in exchange gas. The constant of proportionality between $n_{\rm cav}$ and ΔT is thus approximately 10 times stronger when the bottles are under vacuum, meaning each photon absorbed increases the temperature by 10 times as much as when the bottles are immersed in helium exchange gas.

For moderate exchange gas pressures, the optical resonances exhibit the multistable behaviour described by Equation (4.8). Under these conditions, there is a competition between the $\Delta_{\rm nl}$ and $\Delta_{\rm nl}^{(2)}$ terms, with the resulting lineshapes shown in Figure 4.15. At the lowest injected powers ($P < 2\ \mu$W), we fit the resonances with a linear lineshape to extract κ and $\kappa_{\rm ex}$. As the power is increased, $\Delta_{\rm nl}$ becomes important so we fit the resonances with Equation (4.5) and extract $\Delta_{\rm nl}/2\pi = -5 \times 10^{-7}$ Hz. As shown in Figure 4.15(a), Equations (4.5) and (4.8) show good agreement for $P < 20\ \mu$W, where the resonance approaches a bistability on the blue-detuned side. For larger injected powers, $\Delta_{\rm nl}^{(2)}$ grows rapidly and must be included in the fit. At these powers, the resonance lineshape bends back towards the red side, eventually exhibiting a discontinuity. We use a genetic algorithm to simultaneously fit forward and reverse scans of the resonance while fixing κ, $\kappa_{\rm ex}$ and $\Delta_{\rm nl}$ (black lines in Figure 4.15).

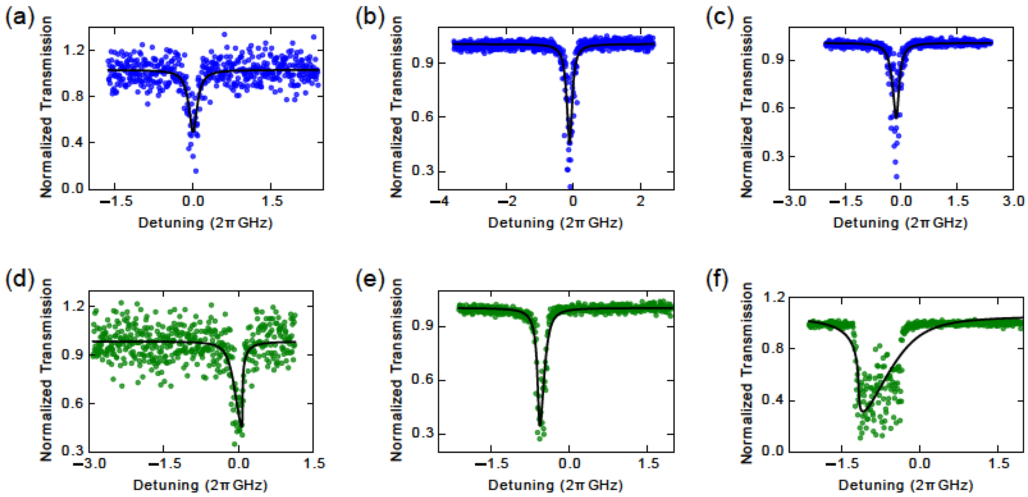

Figure 4.14: As in Figure 4.12 with the fridge at base temperature (9 mK). Injected powers of 0.12 (a, d), 0.75 (b, e), and 1.05 (c, f) μW, corresponding to peak photon number 5.3×10^3 (a), 2.9×10^4 (b), 4.1×10^4 (c), 4.1×10^3 (d), 2.6×10^4 (e) and 3.1×10^4 (f). Fits to the data using Equation (4.5) reveal $\Delta_{\text{nl}}/2\pi \sim -3 \times 10^{-6}$ Hz.

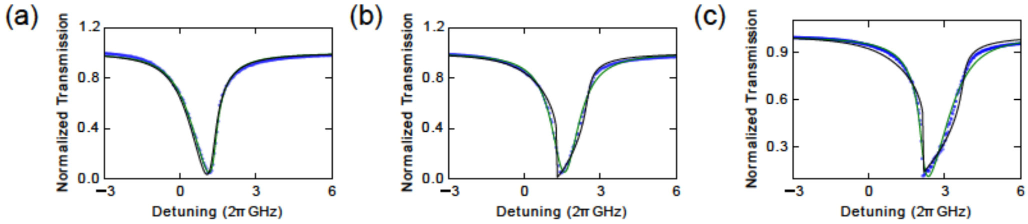

Figure 4.15: Optical multistability manifests at 4.2 K in moderate exchange gas. Transmisison data (blue circles) fit with Equations (4.5) (green) and (4.8) (black) for injected powers of (a) 20, (b) 95 and (c) 130 μW, corresponding to peak photon numbers of 9.4×10^4 (a), 4.5×10^6 (b) and 5.8×10^6 (c). At moderate powers $P < 20$ μW, $\Delta_{\text{nl}}^{(2)}$ is negligible and the data can be satisfactorily fit with Equation (4.5). As power is increased, $\Delta_{\text{nl}}^{(2)}$ becomes important until it eventually dominates.

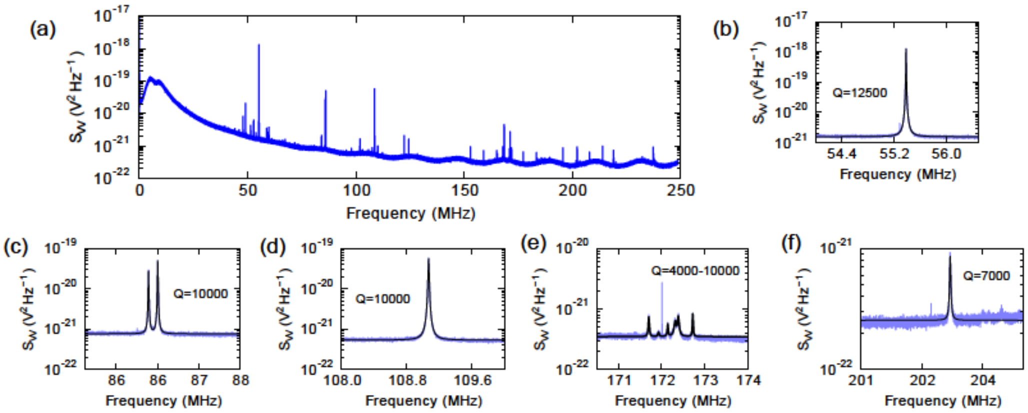

Figure 4.16: (a) Noise spectrum of the high-pass filtered optical transmission signal at room temperature. (b-f) The most prevalent mechanical modes of the bottle resonator with fits in black. We focus on the 55 MHz mode at low temperatures.

4.3 Mechanics

4.3.1 Room Temperature Mechanical Properties

Due to the large amplitude of thermally-driven motion at room temperature, we observe many modes of the bottle resonator, ranging in frequency from ∼50 MHz to well over 200 MHz. As expected, larger bottles exhibit lower frequency oscillations, while the fundamental mode of smaller bottle resonators is observed to be significantly increased. Figure 4.16 shows the high frequency noise spectrum of a bottle resonator transduced from the high-pass filtered (>30 kHz) optical transmission in the tapered fiber. The bottle used in these measurements is the same one used in the low temperature measurements presented in the rest of the thesis. The spectrum in Figure 4.16 shows a number of mechanical resonances with the most efficiently transduced at 55 MHz, 86 MHz, 109 MHz, 172 MHz and 202 MHz. We fit many of these resonances with Equation (2.43) and extract mechanical quality factors on the order of 10^4. We note that the 86 MHz mode is a doublet, while the modes around 172 MHz seem to be closely split multiplets. Since our bottles resemble spheroids, these multiplets are likely degeneracies that are split by the asymmetries in the bottle resonator's shape.

To further investigate the interaction of the optical cavity with the mechanical resonator, we can record the high frequency noise spectrum of the optical transmission as the laser is detuned across the optical resonance. We do this by tuning the laser across the resonance in discrete steps, stopping at each point to collect high-frequency data with the ADC. From

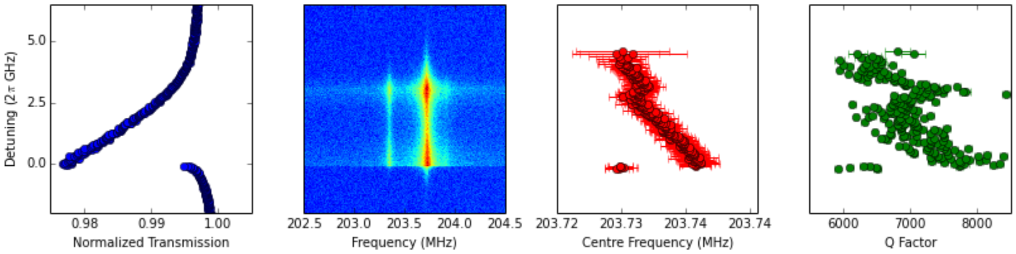

Figure 4.17: From left: normalized transmission of the laser as it is detuned across the optical resonance, $S_{VV}(f)$ around a mechanical resonance at 203 MHz, centre frequency and Q of the mechanical mode extracted from fits to $S_{VV}(f)$.

this data, we can construct plots, like the ones in Figure 4.17, that show the AC spectrum of a smaller bottle resonator near its mechanical resonance frequency as a function of laser detuning. Fitting these spectra, we can now examine any trends in the resonance frequency or quality factor. Looking at Figure 4.17, there is an increase in f_m as the laser is tuned to the centre of the optical cavity. The shape of this trend follows that of the optical transmission profile, with an additional feature around $\Delta/2\pi \simeq 3$ GHz. These effects are explained by heating of the bulk material due to photon absorption; the maximum value of f_m corresponds to the centre of the cavity resonance where n_cav, and therefore heating, is largest. The optical resonance exhibits a doublet structure at low input powers which is obscured by the nonlinear transmission; this is what causes the two peaks in f_m.

4.3.2 Low Temperature Mechanical Properties

At low temperatures, we focus primarily on the 55 MHz mode, which is the lowest energy mechanical mode and exhibits the largest signal at room temperature, making it the easiest mode to observe inside the dilution fridge. Convection is the main method of heat dissipation in the bottles, so the best way to ensure thermalization of the silica resonator is to immerse the experiment in an exchange gas. Figure 4.18 shows the spectrum of the 55 MHz mechanical mode at 300, 77 and 4.2 K, where it is thermalized using exchange gas (nitrogen at 300 and 77 K, and helium at 4.2 K). The spectra are thermomechanically calibrated [97] according to Equation (2.43) using $m_\mathrm{eff} = 47.6$ ng determined from COMSOL simulations. We observe that both the centre frequency and the quality factor of the mechanical resonance seem to vary with temperature, with the frequency decreasing from 55.4 MHz at room temperature to 54.8 MHz at 77 K, before increasing to 55.3 MHz at 4.2 K. We see a similar trend in the quality factors, with values of 12500, 640 and 1125 at 300, 77, and 4.2 K, respectively. We hypothesize that Q_m will continue to increase at lower temperatures as

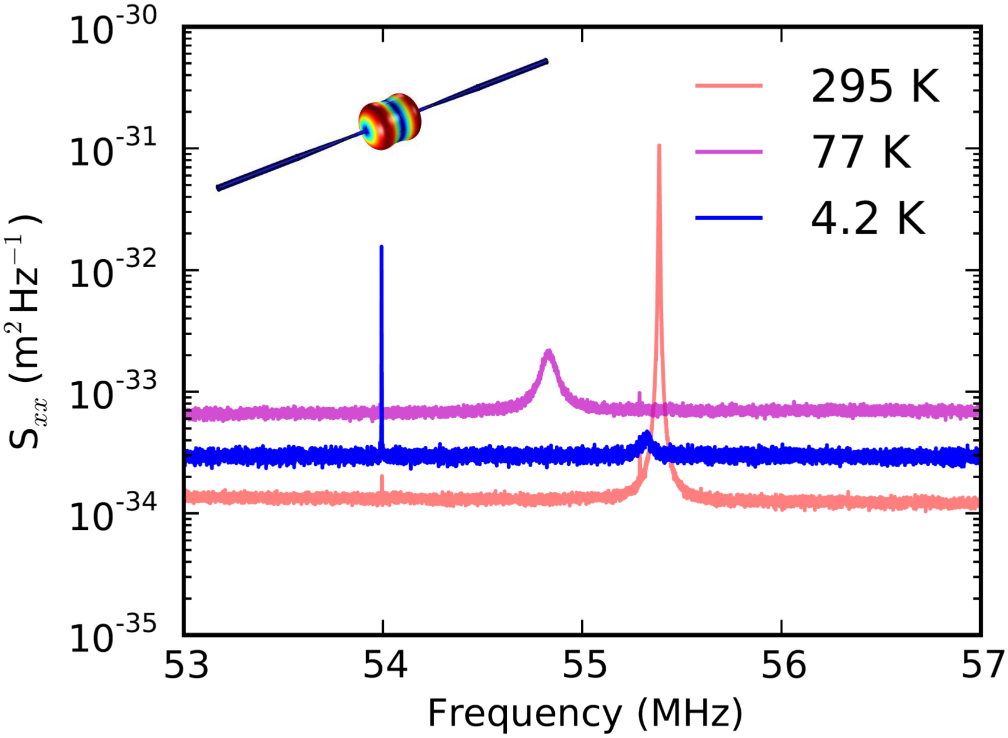

Figure 4.18: Displacement PSD of the 55 MHz mechanical mode at 300, 77 and 4.2 K, where it is thermalized using exchange gas. Inset: COMSOL-simulated breathing modeshape of the 55 MHz mechanical mode. Reprinted with permission from [A. J. R. MacDonald, G. G. Popowich, B. D. Hauer, P. H. Kim, A. Fredrick, X. Rojas, P. Doolin, and J. P. Davis. Optical microscope and tapered fiber coupling apparatus for a dilution refrigerator. *Review of Scientific Instruments*, 86(1):013107, 2015]. Copyright 2015, AIP Publishing LLC.

coupling of acoustic phonons to two-level systems in the silica freezes out [101, 102, 103].

4.3.3 Mechanical Mode Thermometry[1]

In order to cool the bottles further, or to study their motion at temperatures intermediate to 77 and 4.2 K, knowledge of the mechanical mode temperature is crucial. The thermally insulating properties of silica mean that the bottles are unlikely to thermalize well to the base plate of the fridge, so we cannot rely on the fridge thermometers. We note at this point that the temperature of the mechanical mode and the transduction coefficient α are

---

[1] This analysis is derived from those given in the supplementary information of Ref. [20] and the main text of Ref. [98].

indistinguishable in Equation (2.43) and thus are both contained in the fit amplitude A of S_{VV}. Thus, if we have prior knowledge of α, we can relatively easily determine the temperature of the mode. There are many factors that determine α including the number of photons in the cavity, the slope of the optical resonance (related to its Q factor), the optomechanical coupling strength and the efficiencies of the detection electronics, but if we can measure all of these factors, we can determine the temperature [26, 98, 112].

If we do not have a good understanding of α, we can instead generate a signal which is detected analogously to the mechanical motion to calibrate α and determine T. This can be done relatively simply by phase modulating the input light to the optical cavity [98]. An electro-optic modulator (EOM) is a nonlinear crystal which exhibits a voltage-dependent refractive index through the linear electro-optic effect. A sinusoidal drive voltage applied at angular frequency Ω_{mod} results in a phase modulation of the output light,

$$\begin{aligned} s_{\mathrm{out}}(t) &= s_{\mathrm{in}} e^{i\beta \sin \Omega_{\mathrm{mod}} t} \\ &= s_{\mathrm{in}} \sum_{k=-\infty}^{+\infty} (\pm 1)^k J_k(\beta) e^{ik\Omega_{\mathrm{mod}} t} \\ &\approx s_{\mathrm{in}} (J_0(\beta) + J_1(\beta) e^{i\Omega_{\mathrm{mod}} t} - J_1(\beta) e^{-i\Omega_{\mathrm{mod}} t}), \end{aligned} \tag{4.9}$$

where $\beta = \pi V / V_\pi$ is the phase modulation depth for an applied voltage V and J_0, J_1 are Bessel functions of the first kind. V_π is a device-dependent quantity which describes the voltage required to generate a π phase shift between the input and output light fields. As shown in Equation 4.9 and Figure 4.19, weak driving of the EOM will generate sidebands on the input laser, spaced at $\pm\Omega_{\mathrm{mod}}$. Here, we have assumed that $\beta \ll 1$ such that only the first order sidebands need be included.

We note that through the optomechanical interaction, sinusoidal motion of the mechanical oscillator also modulates laser light which passes through the cavity with the modulation strength $\xi = G x_0 / \Omega_{\mathrm{m}}$. Note that the temperature enters into this relation through the amplitude of the mechanical motion $x_0 = \sqrt{k_B T / m_{\mathrm{eff}} \Omega_{\mathrm{m}}^2}$, as given by Equation (2.36). Assuming $\xi \ll 1$ (see Appendix A), the sidebands modify the light to have the form

$$s_{\mathrm{out}}(t) = s_{\mathrm{in}} e^{i\xi \sin \Omega_{\mathrm{m}} t} \approx s_{\mathrm{in}} (J_0(\xi) + J_1(\xi) e^{i\Omega_{\mathrm{m}} t} - J_1(\xi) e^{-i\Omega_{\mathrm{m}} t}). \tag{4.10}$$

This is identical to the modulation given by Equation (4.9).

We can more rigorously prove that the optomechanical interaction and the phase modulation give rise to analogous signals by returning to Equation (2.53). We again solve this equation,

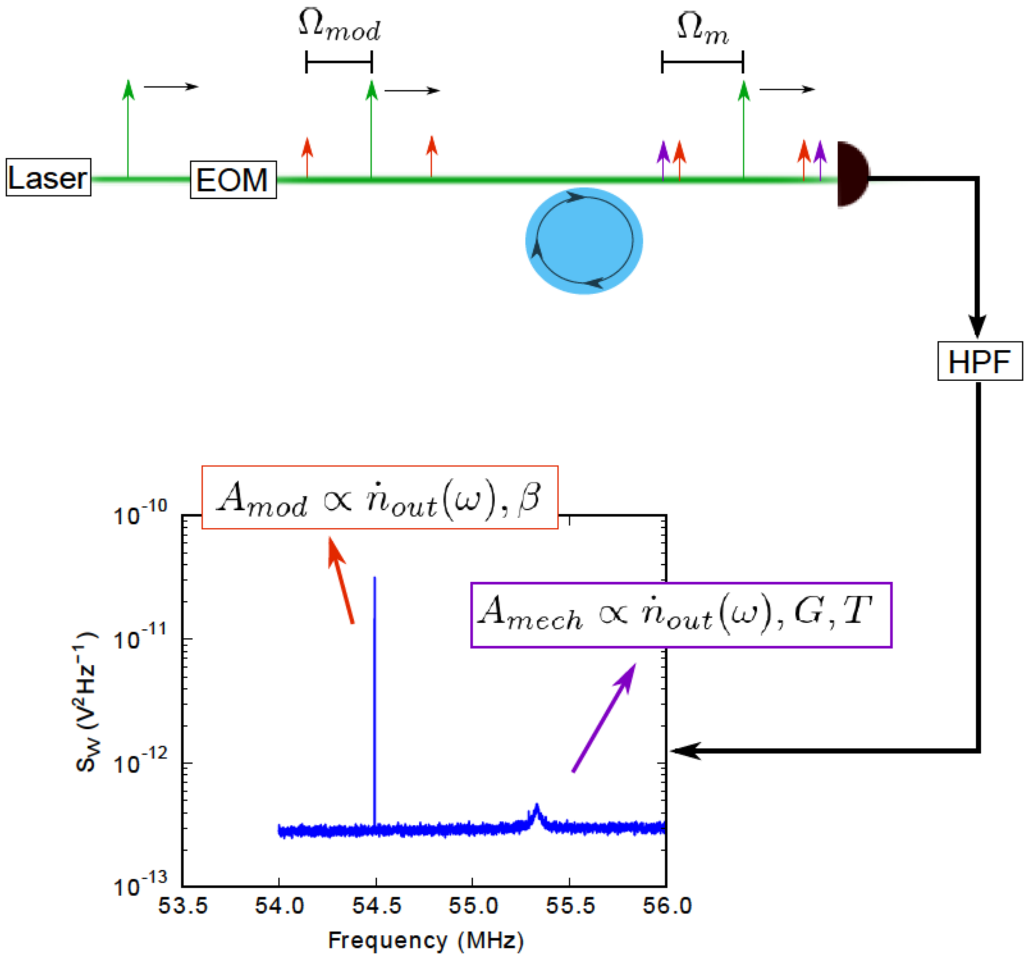

Figure 4.19: Schematic of the phase calibration process. Sidebands at $\pm\Omega_{\mathrm{mod}}$ are generated on the laser by an EOM. When the light passes through the optical cavity, the mechanical motion also adds sidebands, at $\pm\Omega_{\mathrm{m}}$. When the laser light is detected on the photodiode, the sidebands result in peaks in the high-frequency PSD. The energy in the mechanical signal depends on the optomechanical coupling strength G and the temperature T of the mode, while the phase modulation signal depends on the modulation depth β. As shown in detail in Appendix A, both signals are transduced by the optical cavity identically, and so have the same dependence on the transmission spectrum $\dot{n}_{\mathrm{out}}(\omega)$. Therefore, as long as β remains constant, $R_{\mathrm{T}} = A_{\mathrm{mech}}/A_{\mathrm{mod}} \propto T$.

but do not make the assumption of near-steady state optics (*i.e.*, we do not take $a \rightarrow \bar{a}+\delta a$), since phase modulation of the light input to the cavity will make s_{in} time-dependent. We begin by assuming that the solution to this differential equation takes the form of $a(t) = a_{\mathrm{h}}(t) + a_{\mathrm{p}}(t)$, where $a_{\mathrm{h}}(t)$ is the solution to the associated homogeneous equation (where $s_{\mathrm{in}} = 0$) and $a_{\mathrm{p}}(t)$ is the particular solution [20]. We can further make the assumption that the particular and homogeneous solutions are related by $a_{\mathrm{p}}(t) = a_{\mathrm{h}}(t)f(t)$, where $f(t)$ is a yet-to-be-determined function, dependent on the input field $s_{\mathrm{in}}(t)$.

Choosing the form $x(t) = x_0 e^{-\Gamma t/2}\cos\Omega_{\mathrm{m}}t$ for the mechanical motion of a damped harmonic oscillator and recalling that the mechanical oscillator operates in the high Q regime ($\Omega_{\mathrm{m}} \gg \Gamma$), we find

$$a_{\mathrm{h}}(t) = a_0 e^{-\left(\frac{\kappa}{2}-i\Delta\right)t}\left(1+\frac{\xi}{2}e^{-\Gamma t/2}\left[e^{i\Omega_{\mathrm{m}}t}-e^{-i\Omega_{\mathrm{m}}t}\right]\right). \tag{4.11}$$

We now move on to the particular solution which requires first solving for $f(t)$ (see Appendix A) and multiplying the result by Equation (4.11). Assuming first a single-toned drive at the laser frequency ($s_{\mathrm{in}}(t) = s_{\mathrm{in}}$), we find that

$$a_{\mathrm{p}}(t) = \sqrt{\kappa_{\mathrm{ex}}}s_{\mathrm{in}}\left(\frac{1}{\frac{\kappa}{2}-i\Delta}+\frac{\xi}{2}e^{-\Gamma t/2}\left[\frac{e^{i\Omega_{\mathrm{m}}t}}{\frac{\kappa}{2}-i\Delta}-\frac{e^{-i\Omega_{\mathrm{m}}t}}{\frac{\kappa}{2}-i\Delta}-\frac{e^{i\Omega_{\mathrm{m}}t}}{\frac{\kappa}{2}-i(\Delta-\Omega_{\mathrm{m}})}+\frac{e^{-i\Omega_{\mathrm{m}}t}}{\frac{\kappa}{2}-i(\Delta+\Omega_{\mathrm{m}})}\right]\right). \tag{4.12}$$

Since $a_{\mathrm{h}}(t)$ decays at a rate proportional to κ (on the order of $2\pi \times 10$ MHz in our experiments), which is much faster than the decay rate Γ (typically, $2\pi \times 5 - 100$ kHz in our experiments, depending on the temperature) of $a_{\mathrm{p}}(t)$, we take $a(t) = a_{\mathrm{p}}(t)$ and neglect the homogeneous solution. We use Equation (2.21) to calculate the intensity, proportional to $|s_{\mathrm{out}}(t)|^2$, of light impinging on a photodetector in the case of direct detection. The voltage signal output by the detector is

$$V_{\mathrm{out}}(t) = V_{\mathrm{DC}} + V_{\mathrm{mech}}(t), \tag{4.13}$$

where

$$V_{\mathrm{DC}} = H(\omega)|s_{\mathrm{in}}|^2\left(1-\frac{\kappa_{\mathrm{ex}}\kappa_0}{\frac{\kappa^2}{4}+\Delta^2}\right) \tag{4.14}$$

is the time-independent signal representing the transmission profile of the cavity and

$$V_{\mathrm{mech}}(t) = H(\omega)|s_{\mathrm{in}}|^2 \frac{\xi\kappa_{\mathrm{ex}}}{2} e^{-\frac{\Gamma t}{2}} \left(\frac{C_1(\Omega_{\mathrm{m}}) \cos \Omega_{\mathrm{m}} t}{D(0)D(\Omega_{\mathrm{m}})D(-\Omega_{\mathrm{m}})} + \frac{C_2(\Omega_{\mathrm{m}}) \sin \Omega_{\mathrm{m}} t}{D(0)D(\Omega_{\mathrm{m}})D(-\Omega_{\mathrm{m}})} \right) \tag{4.15}$$

is the voltage signal oscillating at the mechanical frequency Ω_{m}. $H(\omega)$ incorporates all electronic and optical gains in the detection system and, in practice, is weakly frequency-dependent, but we will choose Ω_{mod} such that $H(\omega) = H$ is flat across the region of interest. For simplicity of notation, we have defined $C_1(\Omega), C_2(\Omega)$ and $D(\Omega)$ as

$$C_1(\Omega) = \Delta\Omega \left(-\kappa[\kappa^2 + 4\Delta^2] + \kappa_{\mathrm{ex}}[\kappa^2 + 4\Delta^2 - 4\Omega^2] \right) \tag{4.16}$$

$$C_2(\Omega) = \Delta\Omega^2 \left(\kappa[4\kappa_{\mathrm{ex}} - 3\kappa] + 4[\Delta^2 - \Omega^2] \right) \tag{4.17}$$

$$D(\Omega) = \frac{\kappa^2}{4} + (\Delta - \Omega)^2, \tag{4.18}$$

which we note are time-independent functions of both the applied frequency Ω and the laser detuning Δ.

We note at this point that the time-independent V_{DC} and high-frequency $V_{\mathrm{mech}}(t)$ are filtered by our photodetector, so we only concern ourselves with the latter, which can be rewritten as

$$V_{\mathrm{mech}}(t) = H|s_{\mathrm{in}}|^2 \frac{G\kappa_{\mathrm{ex}}}{2\Omega_{\mathrm{m}}} \frac{(C_1(\Omega_{\mathrm{m}})x(t) - C_2(\Omega_{\mathrm{m}})\dot{x}(t)/\Omega_{\mathrm{m}})}{D(0)D(\Omega_{\mathrm{m}})D(-\Omega_{\mathrm{m}})}. \tag{4.19}$$

Fourier transforming and squaring Equation (4.19) to find the voltage PSD, according to Equation (2.32), yields

$$S_{VV}(\omega) = \alpha S_{xx}(\omega) \tag{4.20}$$

where

$$\alpha = \frac{H^2|s_{\mathrm{in}}|^4 G^2 \kappa_{\mathrm{ex}}^2}{4\Omega_{\mathrm{m}}^2} \frac{C_1^2(\Omega_{\mathrm{m}}) + C_2^2(\Omega_{\mathrm{m}})}{D^2(0)D^2(\Omega_{\mathrm{m}})D^2(-\Omega_{\mathrm{m}})} \tag{4.21}$$

is the detuning-dependent transduction coefficient introduced in Equation (2.43) and $S_{xx}(\omega)$ is the displacement PSD of the mechanical mode derived in Section 2.3.1.

In the case of a phase-modulated drive, we take $s_{\mathrm{in}}(t) = s_{\mathrm{in}}(1 + i\beta e^{-\gamma t/2} \sin \Omega_{\mathrm{mod}} t)$ in Equation (2.53), where we have included a damping rate γ in the phase modulation for generality (although in reality $\gamma \ll \Gamma$). The homogeneous solution is drive-independent so we need only recalculate $a(t) \approx a_{\mathrm{p}}(t)$ with the new drive,

$$\begin{aligned} a(t) = \sqrt{\kappa_{\mathrm{ex}}} s_{\mathrm{in}} \Bigg(& \frac{1}{\frac{\kappa}{2} - i\Delta} + \frac{\beta}{2} e^{-\frac{\gamma t}{2}} \left[\frac{e^{i\Omega_{\mathrm{mod}} t}}{\frac{\kappa}{2} - i(\Delta - \Omega_{\mathrm{mod}})} - \frac{e^{-i\Omega_{\mathrm{mod}} t}}{\frac{\kappa}{2} - i(\Delta + \Omega_{\mathrm{mod}})} \right] \\ & - \frac{\xi}{2} e^{-\frac{\Gamma t}{2}} \left[\frac{e^{i\Omega_{\mathrm{m}} t}}{\frac{\kappa}{2} - i(\Delta - \Omega_{\mathrm{m}})} - \frac{e^{-i\Omega_{\mathrm{m}} t}}{\frac{\kappa}{2} - i(\Delta + \Omega_{\mathrm{m}})} - \frac{e^{i\Omega_{\mathrm{m}} t}}{\frac{\kappa}{2} - i\Delta} + \frac{e^{-i\Omega_{\mathrm{m}} t}}{\frac{\kappa}{2} - i\Delta} \right] \Bigg). \end{aligned} \tag{4.22}$$

Keeping in mind the time dependence of $s_{\mathrm{in}}(t)$ in the rotating frame, we can now write

$$\begin{aligned} s_{\mathrm{out}}(t) = s_{\mathrm{in}} \Bigg(& 1 + \frac{\beta}{2} e^{-\gamma t/2} \left[e^{i\Omega_{\mathrm{mod}} t} - e^{-i\Omega_{\mathrm{mod}} t} \right] - \frac{\kappa_{\mathrm{ex}}}{\frac{\kappa}{2} - i\Delta} \\ & - \frac{\kappa_{\mathrm{ex}}\beta}{2} e^{-\frac{\gamma t}{2}} \left[\frac{e^{i\Omega_{\mathrm{mod}} t}}{\frac{\kappa}{2} - i(\Delta - \Omega_{\mathrm{mod}})} - \frac{e^{-i\Omega_{\mathrm{mod}} t}}{\frac{\kappa}{2} - i(\Delta + \Omega_{\mathrm{mod}})} \right] \\ & + \frac{\kappa_{\mathrm{ex}}\xi}{2} e^{-\frac{\Gamma t}{2}} \left[\frac{e^{i\Omega_{\mathrm{m}} t}}{\frac{\kappa}{2} - i(\Delta - \Omega_{\mathrm{m}})} - \frac{e^{-i\Omega_{\mathrm{m}} t}}{\frac{\kappa}{2} - i(\Delta + \Omega_{\mathrm{m}})} - \frac{e^{i\Omega_{\mathrm{m}} t}}{\frac{\kappa}{2} - i\Delta} + \frac{e^{-i\Omega_{\mathrm{m}} t}}{\frac{\kappa}{2} - i\Delta} \right] \Bigg). \end{aligned} \tag{4.23}$$

Squaring Equation (4.23), we can again separate $V_{\mathrm{out}}(t)$ into a DC component and components $V_{\mathrm{mech}}(t)$ and $V_{\mathrm{mod}}(t)$, oscillating at Ω_{m} and Ω_{mod}, respectively. The component at Ω_{m} is identical to the one in Equation (4.15), while the component at Ω_{mod} is

$$V_{\mathrm{mod}}(t) = -H|s_{\mathrm{in}}|^2 \frac{\beta\kappa_{\mathrm{ex}}}{2} e^{-\frac{\gamma t}{2}} \left[\frac{C_1(\Omega_{\mathrm{mod}}) \cos \Omega_{\mathrm{mod}} t}{D(0)D(\Omega_{\mathrm{mod}})D(-\Omega_{\mathrm{mod}})} + \frac{C_2(\Omega_{\mathrm{mod}}) \sin \Omega_{\mathrm{mod}} t}{D(0)D(\Omega_{\mathrm{mod}})D(-\Omega_{\mathrm{mod}})} \right]. \tag{4.24}$$

Note that this has the same form as $V_{\mathrm{mech}}(t)$, under the transformations $\xi \to -\beta$, $\Omega_{\mathrm{m}} \to \Omega_{\mathrm{mod}}$ and $\Gamma \to \gamma$. Since the Fourier transform is linear, the phase modulation is transduced through the cavity identically to the optomechanical signal, and a definite relationship between the peaks at Ω_{m} and Ω_{mod} has been established. Following the procedure above, we find the total voltage power spectral density to be given by (see Appendix A)

$$S_{VV}(\omega) = \alpha S_{xx}(\omega) + \alpha_{\mathrm{mod}} S_{\phi\phi}(\omega) \tag{4.25}$$

where the $S_{\phi\phi}(\omega)$ is defined as the PSD of the phase modulation signal $\phi(t) = \beta e^{-\gamma t/2} \sin \Omega_{\mathrm{mod}} t$ and α_{mod} is given by

$$\alpha_{\mathrm{mod}} = \frac{H^2|s_{\mathrm{in}}|^4\kappa_{\mathrm{ex}}^2}{4} \frac{C_1^2(\Omega_{\mathrm{mod}}) + C_2^2(\Omega_{\mathrm{mod}})}{D^2(0)D^2(\Omega_{\mathrm{mod}})D^2(-\Omega_{\mathrm{mod}})}. \tag{4.26}$$

We ignore any cross terms when squaring the Fourier transform by choosing Ω_{mod} such that $|\Omega_{\mathrm{mod}} - \Omega_{\mathrm{m}}| \gg \Gamma, \gamma$. We additionally choose Ω_{mod} close to Ω_{m} so that any frequency dependence in H can be neglected.

As discussed in Section 2.3.1, the equipartition theorem states that the temperature of the mechanical mode is proportional to the area under the $S_{xx}(\omega)$ signal. Since $S_{\phi\phi}(\omega)$ and $S_{xx}(\omega)$ are transduced analogously in Equation (4.25), knowledge (via the applied voltage V and V_π) of the energy in the phase modulation signal can be used to absolutely determine the mode temperature [98].

4.3.3.1 Practical Implementation

In practice, we implement the phase calibration procedure outlined above by driving the EOM shown in Figures 3.21 and 4.19 with a 1 mV peak-to-peak voltage at a frequency of 54.5 MHz, chosen to be near the lowest-frequency mechanical mode. We unfortunately do not have a good measure of V_π and so do not know β or the absolute energy in the phase modulation signal. We do, however, know that only the mechanical mode should be affected by a change in temperature, such that the ratio R_{T} of the area under the mechanical peak, A_{mech}, to the area under the phase calibration peak, A_{mod}, is proportional to the temperature of the mechanical mode

$$R_{\mathrm{T}} = \frac{A_{\mathrm{mech}}}{A_{\mathrm{mod}}} \propto T. \tag{4.27}$$

In our experiments, the linewidth γ is much too small to be resolved by our detection system (due to the sub-Hz linewidth of our modulation source), so we approximate the area of the phase modulation signal by summing the bins in $S_{VV}(f)$ around the peak (of approximate bandwidth 400 Hz) and subtracting off the noise floor contribution. In contrast to Equation (2.43), we find that our experimental noisefloor tends to vary linearly with frequency (as $S_{VV}^{\mathrm{NF}} = y_0 + y_1 f$) on the scales of interest to us. To find the noisefloor contribution, we simply fit a line to the region containing the peak, with the peak excluded. The area of the mechanical peak is proportional to the amplitude, A, in the fit

$$S_{VV}(f) = y_0 + y_1 f + \frac{A f_{\mathrm{m}}}{Q_{\mathrm{m}}[(f^2 - f_{\mathrm{m}}^2)^2 + (f f_{\mathrm{m}}/Q_{\mathrm{m}})^2]}. \tag{4.28}$$

Since we are only concerned with the ratio R_{T} of the two areas and not their absolute value, we take $A_{\mathrm{mech}} = A$ for simplicity.

To fix the temperature scale, we need at least one point where the temperature is well-known. We make several measurements of the mechanical mode as a function of laser detuning

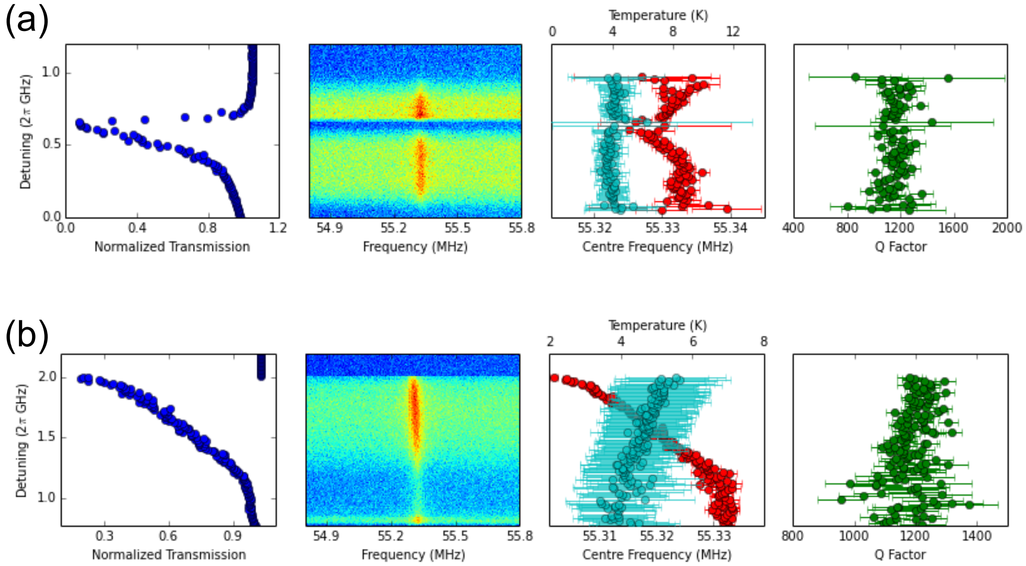

Figure 4.20: Laser detuning versus (from left): normalized optical transmission, $S_{VV}(f)$, f_{m} (red) and calibrated temperature (cyan) and Q_{m} for bottle resonators in helium exchange gas at 4.2 K. Injected optical powers of 12 μW (corresponding to a peak photon number of 5.7×10^5) (a) and 24 μW (peak photon number 9.5×10^5)(b). At lower optical powers, the resonator thermalizes well and f_{m} is roughly constant across detuning, while at higher powers, there is a slight increase in temperature and corresponding decrease in f_{m}.

across each of the 1516 nm and 1581 nm resonances at 4.2 K, with a high pressure of helium exchange gas inside the IVC. This ensures good thermalization of the bottle resonators to the surrounding helium bath. At low optical powers, f_{m} is flat across detuning, indicating little or no heating to the resonator, as shown in Figure 4.20(a). As the injected laser power is increased, we see a shift in f_{m}, as in Figure 4.20(b). To calibrate the value of R_{T} which corresponds to good thermalization with the helium bath at 4.2 K, we plot the ratio R_{T} versus f_{m} for all fits, as shown in blue in Figure 4.21(a) and (b). The points in green are those data points (*i.e.*, fits to mechanical spectra) for which both f_{m} and R_{T} were relatively constant. For the data shown in Figure 4.20(b), for instance, data points at laser detunings $\Delta \lesssim 1.2 \times 2\pi$ GHz are shown in green while those at all other detunings are shown in blue. This procedure was conducted independently for each of the two optical resonances, since different optomechanical coupling strengths between the two could lead to different values of R_{T}. The average of the green data points, those estimated to be best thermalized to 4.2 K, is marked with a yellow star in Figure 4.21. For the 1516 nm resonance, we find a ratio of $R_{4.2} = (1.2 \pm 0.2) \times 10^{15}$ at 4.2 K, while the 1581 nm ratio is $R_{4.2} = (1.3 \pm 0.3) \times 10^{15}$ at a mechanical resonance frequency of $\Omega_{\mathrm{m}} = 55.329 \pm 0.005$ MHz. Uncertainties in these values are taken to be the standard deviations of the selected data about the mean. We also note that the black points show a linear trend in f_{m} versus R_{T}, indicating that f_{m} decreases approximately linearly with increasing temperature over this temperature scale (of a few K). As long as we keep the drive voltage of the EOM constant, we can calibrate the temperature of all our other measurements through

$$T = 4.2 \times \frac{R_{\mathrm{T}}}{R_{4.2}}. \tag{4.29}$$

4.3.4 Detection Methods

As outlined in Section 3.5.2, one of the goals of these experiments was to test and, if possible, refine several different detection schemes, with the goal of improving our detection efficiency at cryogenic temperatures. One way of measuring progress towards this goal is to measure the lowest temperature at which the mechanical signal can be discerned. Lower temperatures result in smaller amplitudes of motion, which in turn result in smaller shifts in the cavity resonance through the optomechanical coupling G. Therefore, the mechanical signal is increasingly difficult to detect as the mode temperature is lowered. Since, along with enhancing the detection, the injected laser light heats the mechanical mode, we will use the injected optical power required to probe the mechanics as one figure-of-merit of the various detection schemes.

Ultimately, there are many factors which determine the sensitivity and detection efficiency

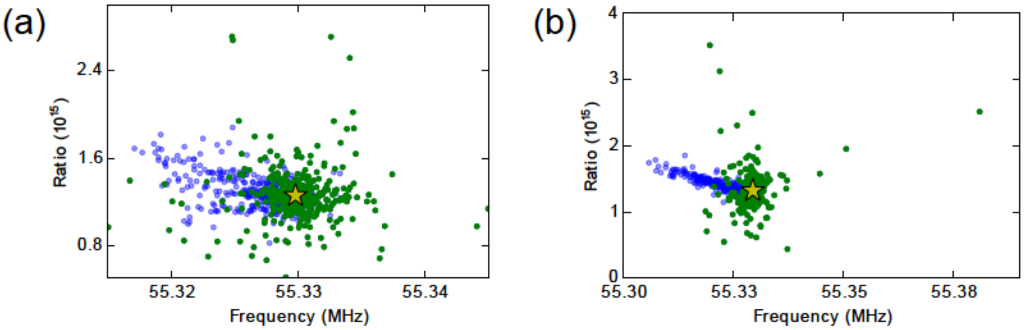

Figure 4.21: Measured ratio $R_{4.2}$ at 4.2 K for coupling between the 55 MHz mechanical mode and the 1516 nm (a) and 1581 nm (b) optical modes. Blue points are data taken at all laser powers in exchange gas at 4.2 K. Green points are the data used to calculate $R_{4.2}$, with the stars denoting the mean values of the green points in each plot.

of a given optomechanical measurement scheme. The first is a convolution of the optomechanical coupling strength G, the number of photons in the cavity n_{cav} and the Q factor of the optical resonance used for detection. The optomechanical coupling strength, along with the amplitude of motion x_0, determines the spectral shift in the cavity resonance. The quality factor of the optical cavity and n_{cav} together determine the slope of the optical resonance, which translates the resonance frequency shift into a change in transmission or phase of the light entering the taper. Finally, the efficiency and response of the optics and electronics, including fiber connections, photodetector, preamplifier and ADC in our case, determine how well this amplitude or phase signal is transduced against a background of electronic and optical noise. Any sources of noise, such as laser noise, electronic noise or vibrations in the environment will detract from the signal. We have worked to minimize such noise by, among other initiatives, increasing the shielding of our Santec laser, using a low-noise preamplifier, shielding our coaxial cables and isolating the system from vibrations in the room as much as possible.

As outlined in Section 3.5.2, we considered three enhancements over the simple direct detection scheme used in the room temperature setup: inserting an EDFA into the optical path, using an avalanche photodiode in place of the usual 1 GHz photodetector and implementing a Mach-Zehnder interferometer, enabling homodyne detection.

4.3.4.1 EDFA

Inserting an EDFA into the optical path between the output of the fridge system and the 1 GHz photodetector, we found that we were indeed able to detect the mechanical modes of

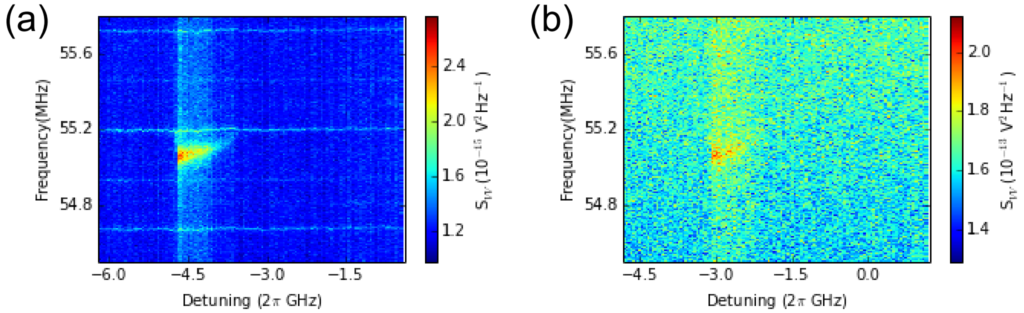

Figure 4.22: PSD of the mechanical signal with (a) and without (b) the use of an EDFA. The EDFA certainly improves the signal-to-noise ratio of the detected spectrum but also adds high-frequency noise, seen here at 54.6 and 55.2 MHz.

the bottle resonator at lower optical powers, as shown in Figure 4.22. However, the EDFA also added significant high-frequency noise to the spectrum, which can interfere with fitting the mechanical resonance.

Furthermore, when we looked at the phase calibration ratio R_{T} with the EDFA, we found that it did not correlate with the change in f_{m}, an indicator of heating in the system. In Figure 4.23, we see that when using the EDFA, R_{T} exhibits peaks which are uncorrelated with the frequency, suggesting that the phase calibration signal and the optomechanical modulation are not transduced through the cavity and detection system in the same way. Since we have already shown (in Section 4.3.3) that these modulation signals should indeed be transduced identically, we believe that the threshold nature of the EDFA results in a greater amplification of the optomechanical signal relative to the phase modulation signal at certain detuning values. We conclude that more work is needed to understand the function of the EDFA before it is compatible with our thermometry.

4.3.4.2 APD

We also tested an avalanche photodiode in place of the 1 GHz detector. Unfortunately we found that the detector was quickly saturated at the optical intensities required to probe the mechanical motion, despite the stated specifications. We thus found no improvement in using it.

4.3.4.3 Balanced Homodyne

Finally we tested the balanced homodyne detection scheme, which we hope to incorporate into future experiments capable of measuring the phase response of the optical cavity. We

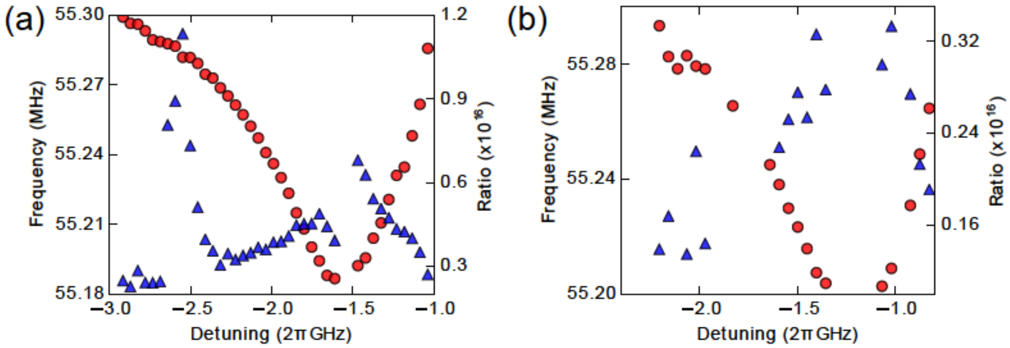

Figure 4.23: The phase calibration ratio (blue triangles) and mechanical frequency (red circles) as the laser is scanned across an optical resonance with (a) and without (b) the use of the EDFA. The threshold nature of the EDFA leads to unequal amplification of the optomechanical and phase modulation signals in (a). Without the EDFA, the trend in R_{T} is anti-correlated to that in f_{m} although the weaker signal makes this trend difficult to discern.

found in some cases that the homodyne detection scheme did provide a larger signal-to-noise ratio for the mechanical resonance, and allowed us to probe the resonance at lower optical powers. Locking the relative phase of the signal and local oscillator arms using the PI servo was an important consideration for a steady signal, as demonstrated in Figure 4.24. The unsteadiness in the signal when the MZI phase is unlocked results from random fluctuations in the phase causing changes in the interference of the signal and local oscillator arms. We experimented with using fast MEMS switches to switch between the homodyne and direct detection schemes, allowing the measurement of the optical resonance profile while detuning the laser, but found the disturbance caused by this switching was enough to unlock the interferometer phase. The PI servo used in this experiment also didn't allow variation in the setpoint, and thus the relative DC phase between the signal and local oscillator, so we were not able to investigate measurements in different quadratures of the light although this is something we hope to improve upon in the future.

Another issue seen with the homodyne scheme results from the nonlinear nature of the optical resonance. This nonlinearity made tuning the laser to the centre of the optical resonance extremely difficult. In the future, a Pound-Drever-Hall laser frequency stabilization scheme [149] might help to track the optical resonance as it shifts, allowing dynamical back-action free measurements at $\Delta = 0$. The bistability present in the bottle resonators might still pose a problem in this regard, so the solution may be to study a system which is less susceptible to laser heating.

Finally, the main issue with the homodyne scheme was once again that the phase calibration

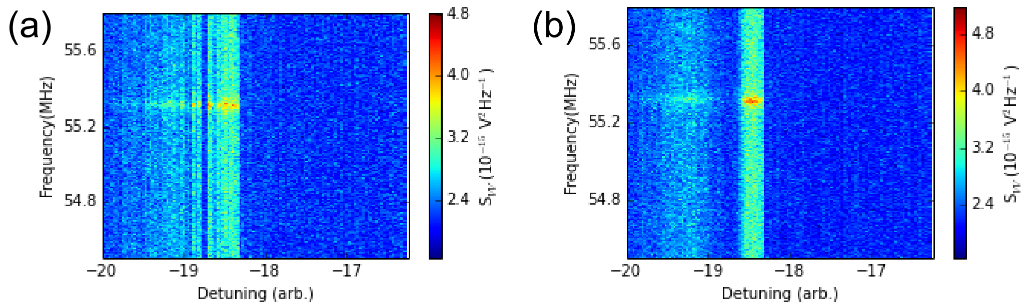

Figure 4.24: Observed mechanical signal at 55 MHz when the relative DC phase of the MZI is (a) unlocked and (b) locked using the PI servo.

ratio did not respond as expected. As shown in Figure 4.25(a), the peak in R_{T} does not correspond to the mechanical frequency shift. Instead the peak is red-detuned from the centre of the optical resonance and does not exhibit the same shape as the cavity profile, which is well-correlated to the shape of the f_{m} versus Δ curve. Taking a closer look at the integrated areas A_{mech} and A_{mod} (Figure 4.25(b)), we see that A_{mech} is peaked slightly red-detuned from the resonance centre, which corresponds to the area of best optomechanical transduction. A_{mod}, on the other hand, exhibits a minimum here, which we believe is due to unwanted interference between the phase modulated light in the local oscillator arm with that in the signal arm. We further test this in Figure 4.25(c) and (d), where we compare the high-pass filtered signal at the modulation frequency (54 MHz here) when the taper is coupled and uncoupled to an optical resonator. In either case, we see that the signal at 54 MHz is independent of the laser detuning, leading us to conclude that the phase calibration signal does not respond to the cavity in the way that we expect. We attempted to remedy this situation by placing the EOM inside the signal arm of the MZI, but found the same behaviour. More work still needs to be done to understand these effects as the phase calibration thermometry is expected to be compatible with homodyne detection [98].

4.3.5 Low Temperature Observations

Using the simplest direct detection measurement scheme (no EDFA or APD), we study the effects of heating to the resonator under various experimental conditions. When the IVC is filled with a high pressure of helium exchange gas, there is little heating to the mechanical resonator as photons are added to the optical cavity (Figure 4.20). For moderate input powers (∼12 μW), we see a very minimal change in the resonance frequency and the phase calibration indicates that the temperature of the mode remains fairly constant at 4.2 K. For larger optical inputs, the temperature increases moderately, to ∼6 K, and the frequency of

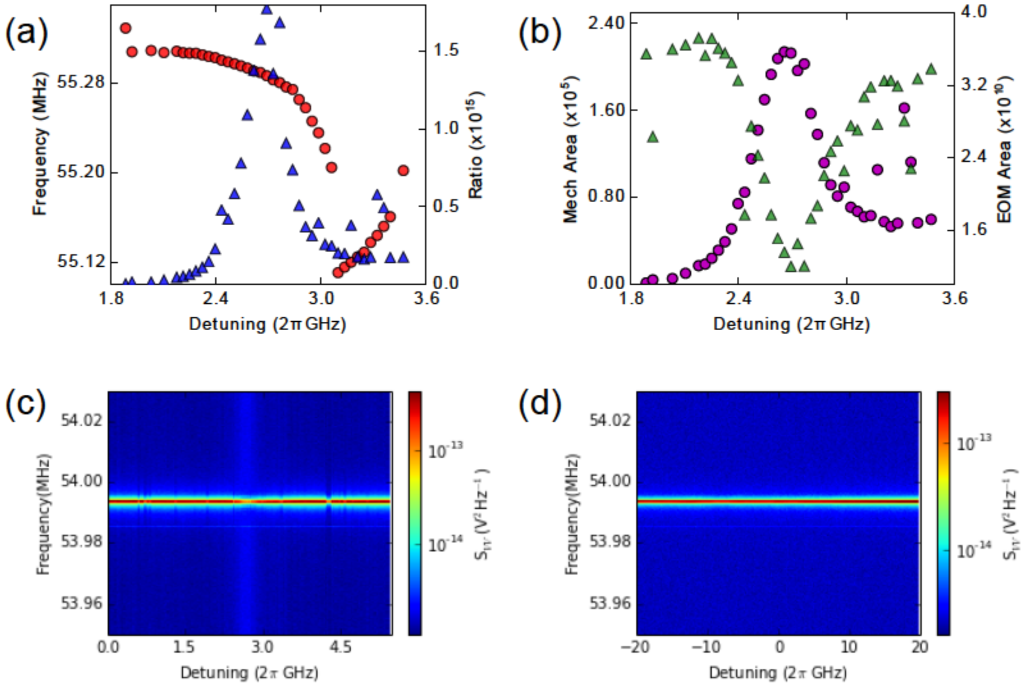

Figure 4.25: (a) Mechanical frequency (red circles) and phase calibration ratio (blue triangles). (b) Integrated PSD area of the mechanical signal (purple circles) and the phase calibration signal (green triangles). PSD of the phase calibration signal is independent of detuning when coupled (c) and uncoupled (d) to an optical resonance.

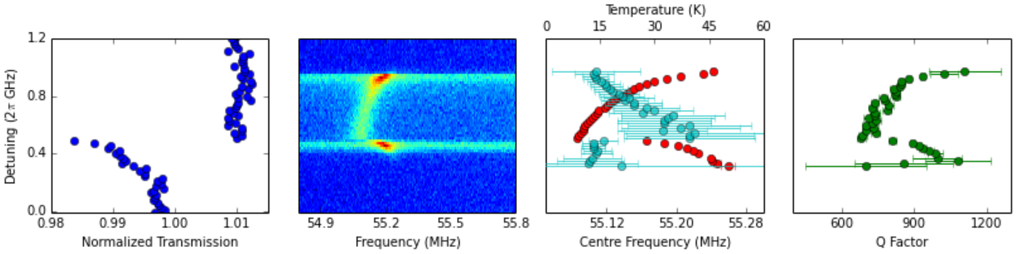

Figure 4.26: As in Figure 4.20 for bottles under vacuum with the fridge at 4.2 K and an injected optical power of 24 μW (peak photon number 2.4×10^4). We notice changes in f_m and Q_m as more photons are coupled into the cavity and the temperature increases.

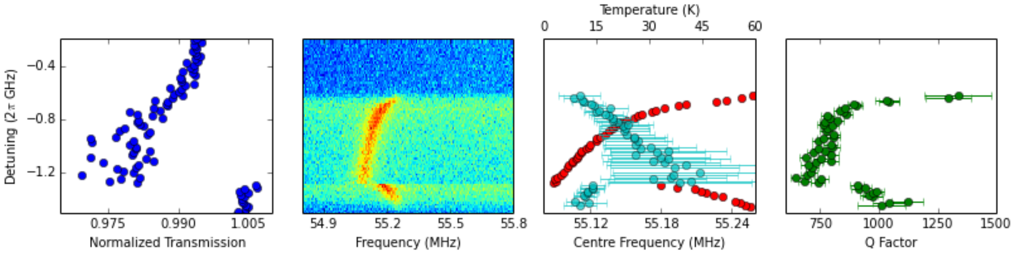

Figure 4.27: As in Figures 4.20 and 4.26 with the fridge operating at base temperature and an injected optical power of 24 μW (peak photon number 2.4×10^4). The observed behaviour is very similar to that in Figure 4.26 where the bottle is under vacuum with the fridge at 4.2 K.

the mode decreases with this temperature increase over 0.02 MHz, a relative shift of ~0.04%.

When the IVC is completely evacuated at 4.2 K (Figure 4.26), we notice first that the optical resonances are extremely nonlinear at the powers used to probe the mechanical motion, making them difficult to fit. Mechanical motion of the bottle resonator is still observable across the optical resonance, with the frequency decreasing considerably. Figure 4.26 shows a relative change in frequency of ~0.3% (0.15 MHz), corresponding to a temperature increase from approximately 13 K to 45 K. The quality factor of the resonance also drops by approximately 40% from 1100 to 700.

When the fridge is operating at its base temperature, the behaviour of the optical and mechanical resonances is very similar to that at 4.2 K, as shown in Figure 4.27. This is because in both cases the bottle has very little opportunity to dissipate additional heat and thus heats up quickly once laser power is injected. At 9 mK, the bottle mode is initially colder (the coldest temperature is approximately 9 K, in contrast to Figure 4.26) but is quickly heated to the same temperature of 45 K with the laser tuned to the optical resonance at a similar injected optical power. We also see a similar decrease in both the quality factor, from 1200 to 700, and the resonance frequency, which again shows a relative shift of $\sim$0.3%.

The fit frequencies and quality factors for all measurements made at fridge temperatures $\leq$4.2 K are shown as points in Figure 4.28 with measurements in nitrogen exchange gas at 77 K and 300 K denoted by triangles. We see that temperatures as high as 70 K were reached when the fridge was operated under vacuum. For temperatures below $\sim$70 K, the frequency of the mechanical mode decreases with increasing temperature, which is in rough agreement with the results of Ref. 110. We notice that the data collected at high exchange gas pressures is clustered around 4.2 K and 55.3 MHz, as expected, and that the relative shift in f_m for small changes in temperature tends to zero as the temperature is lowered.

Figure 4.28(b) plots the inverse of the quality factor, which is proportional to the mechanical decay rate, versus the calibrated mode temperature. We see that for high exchange gas pressures (blue points), Q_m^{-1} increases more rapidly with temperature, an effect that may be related to viscous damping of the exchange gas or to interactions between the mechanical motion and a thin film of liquid He on the surface of the bottle. We also note that the quality factor will continue to increase as the temperature is lowered, which is consistent with theoretical predictions and experimental observations of two-level systems in glass [101, 102, 103]. These systems are well-modelled by a collection of double-welled potentials with asymmetric bound states, giving rise to three distinct temperature regimes. At high temperatures, transitions between the wells occur as a result of thermal excitations. As the temperature is lowered, transitions occur via tunnelling, which allows coupling between the two level systems and acoustic phonons present in the resonator. In this regime, Q_m^{-1}, sometimes termed the internal friction, is constant with temperature. As the temperature is decreased further, phonon-assisted tunnelling ceases, leading to a T^3 dependence of Q_m^{-1}. From Figure 4.28, we postulate that at MHz frequencies, the silica bottles remain in the thermally-activated region. If we were able to reach lower temperatures, we expect that Q_m would continue to increase to values much greater than those observed at room temperature as first thermal activation and then tunneling processes were frozen out.

The lowest temperatures were achieved when the IVC was filled with helium exchange gas (black points in Figure 4.28), meaning that our lowest observable temperature was approximately 4.2 K. Since there was some distribution to the data points used to constrain $R_{4.2}$, we attribute any temperature < 4.2 K in Figure 4.28 to this spread. We thus conclude that the lowest phonon occupation achieved was $\bar{n} \sim 1500$.

It is perhaps interesting to highlight similarities between the behaviour of the optical and mechanical resonances in various temperature regimes. At room temperature, the bistability caused by the thermo-optical nonlinearity occurs when the laser is red-detuned, correspond-

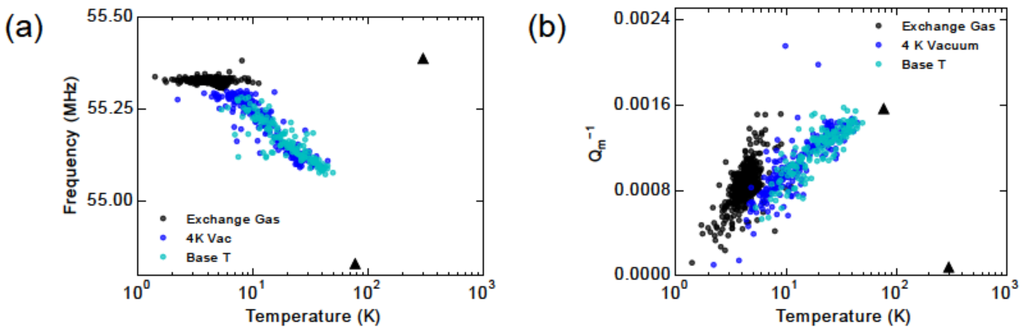

Figure 4.28: (a) Centre frequency of the 55 MHz mechanical resonance and (b) inverse mechanical quality factor as a function of temperature of the resonator for various environmental conditions. Triangles are data from 77 and 300 K in nitrogen exchange gas. We notice that f_m and Q_m behave similarly when the IVC is under vacuum, regardless of whether the fridge is operating at 4.2 K or 9 mK. With high pressures of exchange gas in the IVC, f_m remains roughly constant and Q_m decreases more rapidly with increasing temperature, indicating a larger damping of the mechanics.

ing to positive Δ_nl, while at low temperature, the resonance exhibits a bistability on the blue-detuned side and negative Δ_nl. Similarly, at room temperature, an increase in n_cav and the corresponding increase in temperature causes an increase in both f_m and Q_m, while inside the dilution fridge, both f_m and Q_m decrease with heating of the resonator. When the IVC is filled with a high pressure of exchange gas, the resonator is more efficiently brought into thermal equilibrium with its surroundings and it is better able to dissipate additional heat generated by optical absorption. This increased efficiency in heat dissipation is evident in both the optics and mechanics. The nonlinear detuning parameter Δ_nl for the optical resonances is roughly 10 times smaller when the resonator is immersed in exchange gas than in vacuum. Similarly, the relative frequency shift of the mechanical resonance is also decreased by an order of magnitude (from 0.3 to 0.04 %) in exchange gas. These parallels in the mechanics and the optics reinforce our identification of these observations as heating effects.

4.3.5.1 85 MHz Mode

Although we have primarily focussed on the 55 MHz mode at low temperatures, we note that we did sometimes observe the 86 MHz mode shown in Figure 4.16(c). It is interesting to note that not only did the frequency shift at low temperatures, as for the 55 MHz mode, but also that the mode manifested itself as a single peak at low temperatures, in contrast to the doublet structure observed at room temperature, where the mode exhibits a splitting of

$\sim$180 kHz and Q factors (for each peak) of $\sim 10^4$. However, as the temperature is lowered, the mechanical damping rate increases (Q factor decreases) to the extent that the linewidth of the resonance exceeds the splitting rate, thus obscuring it.

CHAPTER 5

Conclusion

5.1 Summary

Optomechanical devices are systems in which the motion of a mechanical resonator couples to an optical cavity through a position-dependent shift in the optical resonance frequency. Such devices provide a scalable and sensitive detection mechanism for physical phenomena on very small scales. When coupled to a tertiary system, the optomechanical device can be used for manipulation or readout of that system. They are also promising systems to study the interaction between light and mechanics, as well as the quantum-to-classical crossover through the observation of the quantum mechanical behaviour of the mesoscopic mechanical resonator.

One significant goal in the optomechanics community is the observation of quantized jumps in the phonon occupancy of the mechanical resonator, indicating a transition from the ground state to an excited state, a clear indication of quantum mechanical behaviour of the device. One requirement, along with the presence of nonlinear optomechanical coupling, is preparation of the mechanical resonator in its ground state. Since these mechanical resonators have relatively low frequencies (kHz-GHz), there is significant thermal occupation of the resonator at room temperature, requiring cooling to the ground state. Despite recent advances in active laser cooling techniques, a fundamental limit on the final phonon occupation is imposed by the temperature of the resonator's thermal bath, as discussed in Section 2.5.1. Passive cooling is therefore a prerequisite for the types of quantum measurements we wish to make.

To this end, we have designed and tested an optomechanical tapered fiber coupling apparatus situated on the base plate of a commercial dilution refrigerator. Our design features three orthogonal nanopositioning stages, which allow full-control over the taper-resonator coupling conditions, as well as a low-temperature microscope. This imaging system uses light from a green LED and a simple set of optics to image the optomechanical resonator *in situ*, along with a coherent bundle of 37000 optical fibers to transport the image from the interior of the fridge to room temperature. An image resolution of 1 μm was achieved, which is sufficient for aligning the resonator to the tapered fiber. We furthermore found that our coupling system causes negligible heating to the dilution fridge environment, with the achieved base temperature of 9 mK representing only a slight increase over the unloaded base temperature of 7 mK. Under normal experimental conditions, the main source of heating to the fridge is laser light scattered from the tapered fiber.

Since we cannot expect that the mechanical resonator will necessarily thermalize well to the base temperature of the fridge, we cannot rely on the installed mixing chamber thermometers. We have therefore described a method for calibrating the temperature of the mechanical mode using a known optical signal, as detailed in Section 4.3.3. This signal is derived from a phase modulation of the input laser light using an EOM, and is transduced by the cavity identically to the motion of the mechanical resonator. In the phase modulated signal, parallels can be drawn between $\xi = Gx_0/\Omega_\mathrm{m}$, which incorporates optomechanical coupling strength G and temperature of the mode, and the phase modulation strength $\beta = \pi V/V_\pi$. In practice, a phase calibration peak in the voltage PSD is introduced near the mechanical resonance. Since the areas of these two peaks are proportional to β and ξ, respectively, their ratio gives access to the temperature of the mode.

Finally, we tested our system and mechanical mode thermometry using silica bottle optomechanical resonators and a straight tapered fiber. Using this setup, we were able to measure optical resonances of the bottles at a fridge temperature of 9 mK, and demonstrate critical coupling of the resonator at 4 K. At higher injected optical powers, photon absorption in the silica drives thermal expansion of the resonator and temperature-dependent changes in its refractive index. The resonances thus exhibit nonlinear behaviour, which can be described by adding additional photon number-dependent terms in the detuning parameter. Under most experimental conditions, the nonlinearity can be modelled using a cubic equation in n_cav, which is exactly solvable. With a moderate pressure of helium exchange gas at 4 K, however, the nonlinearity exhibits higher-order multistability better modelled with a quintic equation in n_cav. We numerically solve this equation to fit these multistable resonances.

We measured the mechanical motion of the bottle resonators under various experimental conditions and used the phase calibration to determine the temperature of the observed mode spectrum. We found that significant heating to the resonator occurred as the laser was tuned to the centre of the optical resonance and more photons entered the cavity. In particular, when the experimental area was evacuated, the mechanical mode temperature increased to up to 70 K. This increase in temperature was also correlated to a decrease in the frequency and quality factor of the mechanical mode, which can be explained through the presence of two level systems in the silica. Only when the IVC was filled with helium exchange gas (at 4 K), did the bottles thermalize well to the temperature of the fridge since convection is the primary method of heat transfer in this particular geometry. In fact, the bottles did not reach temperatures below 4 K, even with the fridge at its base temperature. We thus estimate a minimum occupation of $\bar{n} \sim 1500$ phonons.

5.2 Future Directions

In the near future, silicon and silicon nitride chip-based optomechanical devices, such as torsion paddles and cantilevers coupled to optical microdisks, will be studied in the fridge. In order to couple to these two-dimensional structures, a tapered fiber with a low spot, called a dimple, must be used in place of the straight tapered fiber [86]. The dimple is more challenging to locate in the imaging system, so the red HeNe laser will be used to assist in this process. Furthermore, the addition of a fourth attocube nanopositioning stage between the fiber holder and the Invar block will enable low temperature adjustments of the dimpled fiber along the fiber axis. This will allow translation of the fiber along its axis, ensuring that the dimple remains in the image field of view during cooldown.

To increase thermalization of on-chip devices to the mixing chamber of the dilution fridge, and therefore lower the final phonon occupancy, the chip will be clamped to the top OFHC copper plate with strips of copper and the areas of the chip around the devices will be coated with gold. This will maximize the conduction of heat from the resonator to the edge of the chip, where it will be conducted away from the chip to the base plate of the fridge via the copper braids discussed earlier. Additionally, the use of physically separated optical and mechanical resonators will reduce the optically-induced heating of the mechanical resonator seen in our work.

We hope to further increase our detection efficiency at low temperatures by eliminating the use of splices inside the fridge, which have been shown to contribute considerable optical losses at low temperature. There is also more work to be done in optimizing the balanced homodyne detection scheme to increase its suitability for use with the mechanical mode thermometry. Some work has already been done towards implementing a Pound-Drever-Hall stabilization scheme [149], which would allow tracking of the optical resonance by the laser, and thus facilitate on-resonance optomechanical measurements. Using a better PI servo that allows a variation in the setpoint, we can exploit the potential of this detection method by exerting full control over the relative phase of the MZI and thus the measurement quadrature.

Future work towards performing optomechanical quantum jump spectroscopy will involve optimizing the quadratic optomechanical coupling already observed in Ref. 85 while simultaneously eliminating the linear coupling. This will ensure that the measurement operator commutes fully with the Hamiltonian of the system, as required for a proper QND measurement. Future experiments may also involve the use of pulses of light in place of the continuous wave input fields used in this work. Suggested protocols for performing QND measurements with pulsed light may make these experiments more feasible [116].

Finally, future iterations of dilution fridge optomechanics experiments will make use of a nuclear demagnetization stage, reaching temperatures as low as 300 μK. However, imaging at that stage will not be possible so the development of on-chip waveguide coupling to the optomechanical resonators will be necessary.

Bibliography

[1] K. L. Ekinci and M. L. Roukes. Nanoelectromechanical systems. *Review of Scientific Instruments*, 76:061101, 2005.

[2] A. Gupta, D. Akin, and R. Bashir. Single virus particle mass detection using microresonators with nanoscale thickness. *Applied Physics Letters*, 84(11):1976, 2004.

[3] M. D. LaHaye, J. Suh, P. M. Echternach, K. C. Schwab, and M. L. Roukes. Nanomechanical measurements of a superconducting qubit. *Nature*, 459(7249):960–964, 2009.

[4] A. D. O'Connell, M. Hofheinz, M. Ansmann, R. C. Bialczak, M. Lenander, M. Lucero, E.and Neeley, D. Sank, H. Wang, M. Weides, J. Wenner, J. M. Martinis, and A. N. Cleland. Quantum ground state and single-phonon control of a mechanical resonator. *Nature*, 464(7289):697–703, 2010.

[5] D. Rugar, R. Budakian, H. J. Mamin, and B. W. Chui. Single spin detection by magnetic resonance force microscopy. *Nature*, 430:329, 2004.

[6] I. Bargatin, E. B. Myers, J. Arlett, B. Gudlewski, and M. L. Roukes. Sensitive detection of nanomechanical motion using piezoresistive signal downmixing. *Applied Physics Letters*, 86:133109, 2005.

[7] J. P. Davis, D. Vick, D. C. Fortin, J. A. J. Burgess, W. K. Hiebert, and M. R. Freeman. Nanotorsional resonator torque magnetometry. *Applied Physics Letters*, 96(7):072513, 2010.

[8] A. Suhel, B. D. Hauer, T. S. Biswas, K. S. D. Beach, and J. P. Davis. Dissipation mechanisms in thermomechanically driven silicon nitride nanostrings. *Applied Physics Letters*, 100(17):173111, 2012.

[9] T. J. Kippenberg and K. J. Vahala. Cavity Optomechanics: Back-Action at the Mesoscale. *Science*, 321(5893):1172–1176, 2008.

[10] F. Marquardt and S. Girvin. Optomechanics. *Physics*, 2:40, 2009.

[11] M. Aspelmeyer, T. J. Kippenberg, and F. Marquardt. Cavity optomechanics. *Reviews of Modern Physics*, 86(4):1391–1452, 2014.

[12] Y. Chen. Macroscopic quantum mechanics theory and experimental concepts of optomechanics. *Journal of Physics B: Atomic, Molecular and Optical Physics*, 46:104001, 2013.

[13] S. Gröblacher, K. Hammerer, M. R. Vanner, and M. Aspelmeyer. Observation of strong coupling between a micromechanical resonator and an optical cavity field. *Nature*, 460(7256):724–727, 2009.

[14] J. C. Sankey, C. Yang, B. M. Zwickl, A. M. Jayich, and J. G. E. Harris. Strong and tunable nonlinear optomechanical coupling in a low-loss system. *Nature Physics*, 6(9):707–712, 2010.

[15] M. Eichenfield, J. Chan, R. M. Camacho, K. J. Vahala, and O. Painter. Optomechanical crystals. *Nature*, 462(7269):78–82, 2009.

[16] J. D. Teufel, T. Donner, D. Li, J. W. Harlow, M. S. Allman, K. Cicak, A. J. Sirois, J. D. Whittaker, K. W. Lehnert, and R. W. Simmonds. Sideband cooling of micromechanical motion to the quantum ground state. *Nature*, 475(7356):359–363, 2011.

[17] A. J. Weinstein, C. U. Lei, E. E. Wollman, J. Suh, A. Metelmann, A. A. Clerk, and K. C. Schwab. Observation and Interpretation of Motional Sideband Asymmetry in a Quantum Electromechanical Device. *Physical Review X*, 4(4):041003, 2014.

[18] S. Schreppler, N. Spethmann, N. Brahms, T. Botter, M. Barrios, and D. M. Stamper-Kurn. Optically measuring force near the standard quantum limit. *Science*, 344(6191):1481–1486, 2014.

[19] Y.-S. Park and H. Wang. Resolved-sideband and cryogenic cooling of an optomechanical resonator. *Nature Physics*, 5(7):489–493, 2009.

[20] A. Schliesser, R. Rivière, G. Anetsberger, O. Arcizet, and T. J. Kippenberg. Resolved-sideband cooling of a micromechanical oscillator. *Nature Physics*, 4(5):415–419, 2008.

[21] E. Gavartin, P. Verlot, and T. J. Kippenberg. A hybrid on-chip optomechanical transducer for ultrasensitive force measurements. *Nature Nanotechnology*, 7(8):509–514, 2012.

[22] P. H. Kim, C. Doolin, B. D. Hauer, A. J. R. MacDonald, M. R. Freeman, P. E. Barclay, and J. P. Davis. Nanoscale torsional optomechanics. *Applied Physics Letters*, 102(5):053102, 2013.

[23] G. Anetsberger, E. Gavartin, O. Arcizet, Q. P. Unterreithmeier, E. M. Weig, M. L. Gorodetsky, J. P. Kotthaus, and T. J. Kippenberg. Measuring nanomechanical motion with an imprecision below the standard quantum limit. *Physical Review A*, 82(6):061804(R), 2010.

[24] J. D. Cohen, S. M. Meenehan, and O. Painter. Optical coupling to nanoscale optomechanical cavities for near quantum-limited motion transduction. *Optics Express*, 21(9):11227, 2013.

[25] B. P. Abbott and R. Abbott *et al.* LIGO: the Laser and Interferometer Gravitational-Wave and Observatory. *Reports on Progress in Physics*, 72:076901, 2009.

[26] C. Doolin, P. H. Kim, B. D. Hauer, A. J. R. MacDonald, and J. P. Davis. Multidimensional optomechanical cantilevers for high-frequency force sensing. *New Journal of Physics*, 16:035001, 2014.

[27] H. Miao, K. Srinivasan, and V. Aksyuk. A microelectromechanically controlled cavity optomechanical sensing system. *New Journal of Physics*, 14:075015, 2012.

[28] M. Wu, A. C. Hryciw, C. Healey, D. P. Lake, H. Jayakumar, M. R. Freeman, J. P. Davis, and P. E. Barclay. Dissipative and Dispersive Optomechanics in a Nanocavity Torque Sensor. *Physical Review X*, 4(2):021052, 2014.

[29] A. G. Krause, M. Winger, T. D. Blasius, Q. Lin, and O. Painter. A high-resolution microchip optomechanical accelerometer. *Nature Photonics*, 6(11):768–772, 2012.

[30] K. Stannigel, P. Rabl, A. S. Sørensen, P. Zoller, and M. D. Lukin. Optomechanical Transducers for Long-Distance Quantum Communication. *Physical Review Letters*, 105(22):220501, 2010.

[31] A. H. Safavi-Naeini and O. Painter. Proposal for an optomechanical traveling wave phononphoton translator. *New Journal of Physics*, 13:013017, 2011.

[32] K. Børkje. Scheme for steady-state preparation of a harmonic oscillator in the first excited state. *Physical Review A*, 90(2):023806, 2014.

[33] A. A. Gangat, T. M. Stace, and G. J. Milburn. Phonon number quantum jumps in an optomechanical system. *New Journal of Physics*, 13:043024, 2010.

[34] A. H. Safavi-Naeini, S. Gröblacher, J. T. Hill, J. Chan, M. Aspelmeyer, and O. Painter. Squeezed light from a silicon micromechanical resonator. *Nature*, 500:185, 2013.

[35] T. A. Palomaki, J. D. Teufel, R. W. Simmonds, and K. W. Lehnert. Entangling Mechanical Motion with Microwave Fields. *Science*, 342(6159):710–713, 2013.

[36] S. G. Hofer, W. Wieczorek, M. Aspelmeyer, and K. Hammerer. Quantum entanglement and teleportation in pulsed cavity optomechanics. *Physical Review A*, 84(5):052327, 2011.

[37] S. Weis, R. Rivière, S. Deleglise, E. Gavartin, O. Arcizet, A. Schliesser, and T. J. Kippenberg. Optomechanically Induced Transparency. *Science*, 330(6010):1520–1523, 2010.

[38] A. H. Safavi-Naeini, T. P. Mayer Alegre, J. Chan, M. Eichenfield, M. Winger, Q. Lin, J. T. Hill, D. E. Chang, and O. Painter. Electromagnetically induced transparency and slow light with optomechanics. *Nature*, 472(7341):69–73, 2011.

[39] V. Fiore, Y. Yang, M. C. Kuzyk, R. Barbour, L. Tian, and H. Wang. Storing Optical Information as a Mechanical Excitation in a Silica Optomechanical Resonator. *Physical Review Letters*, 107(13):133601, 2011.

[40] J. T. Hill, A. H. Safavi-Naeini, J. Chan, and O. Painter. Coherent optical wavelength conversion via cavity optomechanics. *Nature Communications*, 3:1196, 2012.

[41] Y. Liu, M. Davanço, V. Aksyuk, and K. Srinivasan. Electromagnetically Induced Transparency and Wideband Wavelength Conversion in Silicon Nitride Microdisk Optomechanical Resonators. *Physical Review Letters*, 110(22):223603, 2013.

[42] C. Dong, V. Fiore, M. C. Kuzyk, and H. Wang. Optomechanical Dark Mode. *Science*, 338(6114):1609, 2012.

[43] J. Bochmann, A. Vainsencher, D. D. Awschalom, and A. N. Cleland. Nanomechanical coupling between microwave and optical photons. *Nature Physics*, 9:712–716, 2013.

[44] K. Srinivasan and O. Painter. Optical fiber taper coupling and high-resolution wavelength tuning of microdisk resonators at cryogenic temperatures. *Applied Physics Letters*, 90:031114, 2007.

[45] R. Rivière, O. Arcizet, A. Schliesser, and T. J. Kippenberg. Evanescent straight tapered-fiber coupling of ultra-high Q optomechanical micro-resonators in a low-vibration helium-4 exchange-gas cryostat. *Review of Scientific Instruments*, 84(4):043108, 2013.

[46] S. M. Meenehan, J. D. Cohen, S. Gröblacher, J. T. Hill, A. H. Safavi-Naeini, M. Aspelmeyer, and O. Painter. Silicon optomechanical crystal resonator at millikelvin temperatures. *Physical Review A*, 90(1):011803(R), 2014.

[47] A. J. R. MacDonald, G. G. Popowich, B. D. Hauer, P. H. Kim, A. Fredrick, X. Rojas, P. Doolin, and J. P. Davis. Optical microscope and tapered fiber coupling apparatus for a dilution refrigerator. *Review of Scientific Instruments*, 86(1):013107, 2015.

[48] G. Kakarantzas, T. E. Dimmick, T. A. Birks, R. Le Roux, and P. St. J. Russell. Miniature all-fiber devices based on CO_2 laser microstructuring of tapered fibers. *Optics Letters*, 26(15):1137, 2001.

[49] M. Pöllinger, D. O'Shea, F. Warken, and A. Rauschenbeutel. Ultrahigh-Q Tunable Whispering-Gallery-Mode Microresonator. *Physical Review Letters*, 103(5):053901, 2009.

[50] G. Senthil Murugan, M. N. Petrovich, Y. Jung, J. S. Wilkinson, and M. N. Zervas. Hollow-bottle optical microresonators. *Optics Express*, 19(21):20773, 2011.

[51] X. Zhang, L. Liu, and L. Xu. Ultralow sensing limit in optofluidic micro-bottle resonator biosensor by self-referenced differential-mode detection scheme. *Applied Physics Letters*, 104(3):033703, 2014.

[52] K. N. Dinyari, R. J. Barbour, D. A. Golter, and H. Wang. Mechanical tuning of whispering gallery modes over a 0.5 THz tuning range with MHz resolution in a silica microsphere and at cryogenic temperatures. *Optics Express*, 19(19):17966, 2011.

[53] N. E. Flowers-Jacobs, S. W. Hoch, J. C. Sankey, A. Kashkanova, A. M. Jayich, C. Deutsch, J. Reichel, and J. G. E. Harris. Fiber-cavity-based optomechanical device. *Applied Physics Letters*, 101(22):221109, 2012.

[54] S. John. Strong Localization and of Photons and in Certain and Disordered Dielectric and Superlattices. *Physical Review Letters*, 58(23):2486, 1987.

[55] Y. Akahane, T. Asano, B.-S.Song, and S. Noda. Fine-tuned high-Q photonic-crystal nanocavity. *Optics Express*, 13(4):1202, 2005.

[56] E. Kuramochi, M. Notomi, S. Mitsugi, A. Shinya, and T. Tanabe, T.and Watanabe. Ultrahigh-Q photonic crystal nanocavities realized by the local width modulation of a line defect. *Applied Physics Letters*, 88(4):041112, 2006.

[57] V. B. Braginsky, M. L. Gorodetsky, and V. S. Ilchenko. Quality-factor and nonlinear properties of optical whipering gallery modes. *Physics Letters A*, 137(7):8, 1989.

[58] T. Carmon and K. J. Vahala. Visible continuous emission from a silica microphotonic device by third-harmonic generation. *Nature Physics*, 3(6):430–435, 2007.

[59] A. Srinivasan, K.and Stintz, S. Krishna, and O. Painter. Photoluminescence measurements of quantum-dot-containing semiconductor microdisk resonators using optical fiber taper waveguides. *Physical Review B*, 72(20):205318, 2005.

[60] Lord Rayleigh. The problem of the whispering gallery. *Philosophical Magazine*, 20:1001, 1910.

[61] J.L. Dominguez-Juarez, G. Kozyreff, and J. Martorell. Whispering gallery microresonators for second harmonic light generation from a low number of small molecules. *Nature Communications*, 2:254, 2011.

[62] S. M. Spillane, T. J. Kippenberg, and K. J. Vahala. Ultralow-threshold Raman laser using a spherical dielectric microcavity. *Nature*, 415:621, 2002.

[63] T. J. Kippenberg, S. M. Spillane, and K. J. Vahala. Kerr-Nonlinearity Optical Parametric Oscillation in an Ultrahigh-Q Toroid Microcavity. *Physical Review Letters*, 93(8):083904, 2004.

[64] J. U. Fürst, D. V. Strekalov, D. Elser, A. Aiello, U. L. Andersen, Ch. Marquardt, and G. Leuchs. Low-Threshold Optical Parametric Oscillations in a Whispering Gallery Mode Resonator. *Physical Review Letters*, 105(26):263904, 2010.

[65] P. Del'Haye, A. Schliesser, O. Arcizet, T. Wilken, R. Holzwarth, and T. J. Kippenberg. Optical frequency comb generation from a monolithic microresonator. *Nature*, 450(7173):1214–1217, 2007.

[66] N. M. Hanumegowda, C. J. Stica, B. C. Patel, I. White, and X. Fan. Refractometric sensors based on microsphere resonators. *Applied Physics Letters*, 87(20):201107, 2005.

[67] C. Doolin, P. Doolin, B. C. Lewis, and J. P. Davis. Refractometric sensing of Li salt with visible-light Si_3N_4 microdisk resonators. *Applied Physics Letters*, 106(8):081104, 2015.

[68] A. Meldrum and F. Marsiglio. Capillary-Type Microfluidic Sensors Based on Optical Whispering Gallery Mode Resonances. *Reviews in Nanoscience and Nanotechnology*, 3(3):193–209, 2014.

[69] F. Vollmer, S. Arnold, and D. Keng. Single virus detection from the reactive shift of a whispering-gallery mode. *Proceedings of the National Academy of Sciences*, 105(52):20701, 2008.

[70] S. Arnold, R. Ramjit, D. Keng, V. Kolchenko, and I. Teraoka. MicroParticle photophysics illuminates viral bio-sensing. *Faraday Discussions*, 137:65–83, 2007.

[71] T. Aoki, B. Dayan, E. Wilcut, W. P. Bowen, A. S. Parkins, T. J. Kippenberg, K. J. Vahala, and H. J. Kimble. Observation of strong coupling between one atom and a monolithic microresonator. *Nature*, 443(7112):671–674, 2006.

[72] P. E. Barclay, K.-M. C. Fu, C. Santori, A. Faraon, and R. G. Beausoleil. Hybrid Nanocavity Resonant Enhancement of Color Center Emission in Diamond. *Physical Review X*, 1(1):011007, 2011.

[73] B. E. Little, J.-P. Laine, and A. Haus. Analytic Theory of Coupling from Tapered Fibers and Half-Blocks into Microsphere Resonators. *Journal of Lightwave Technology*, 17(4):704, 1999.

[74] M. Humphrey. *Calculation of Coupling Between Tapered Fiber Modes and Whispering-Gallery Modes of a Spherical Microlaser*. PhD thesis, Oklahoma State University, 2004.

[75] T. Carmon, L. Yang, and K. J. Vahala. Dynamical thermal behaviour and thermal self-stability of microcavities. *Optics Express*, 12(20):4742, 2004.

[76] D. W. Vernooy, V. S. Il'chenko, H. Mabuchi, E. W. Streed, and H. J. Kimble. High-Q measurements of fused-silica microsphers in the near infrared. *Optics Letters*, 23(4):247, 1998.

[77] M. L. Gorodetsky, A. A. Savchenkov, and V. S. Ilchenko. Ultimate Q of optical microsphere resonators. *Optics Letters*, 21(7):453, 1996.

[78] M. Eichenfield, J. Chan, A. H. Safavi-Naeini, K. J, Vahala, and O. Painter. Modeling dispersive coupling and losses of localized optical and mechanical modes in optomechanical crystals. *Optics Express*, 17:20078, 2009.

[79] T. J. Kippenberg, S. M. Spillane, and K. J. Vahala. Demonstration of ultra-high-Q small mode volume toroid microcavities on a chip. *Applied Physics Letters*, 85(25):6113, 2004.

[80] X. Sun, X. Zhang, C. Schuck, and H. X. Tang. Nonlinear optical effects of ultrahigh-Q silicon photonic nanocavities immersed in superfluid helium. *Scientific Reports*, 3:1436, 2013.

[81] Y.-S. Park and H. Wang. Regenerative pulsation in silica microspheres. *Optics Letters*, 32(21):3104, 2007.

[82] F. Treussart, V. S. Ilchenko, J.-F. Roch, J. Hare, V. Lefèvre-Seguin, J.-M. Raimond, and S. Haroche. Evidence for intrinsic Kerr bistability of high-Q microsphere resonators in superfluid helium. *European Physcal Journal D*, 1:235, 1998.

[83] J. C. Knight, G. Cheung, F. Jacques, and T. A. Birks. Phase-matched excitation of whipering-gallery-mode resonances by a fiber taper. *Optics Letters*, 22(15):1129, 1997.

[84] M. Cai, O. Painter, and K. J. Vahala. Observation of Critical Coupling in a Fiber Taper to a Silica-Microsphere Whispering-Gallery Mode System. *Physical Review Letters*, 85(1):74, 2000.

[85] C. Doolin, B. D. Hauer, P. H. Kim, A. J. R. MacDonald, H. Ramp, and J. P. Davis. Nonlinear optomechanics in the stationary regime. *Physical Review A*, 89(5):053838, 2014.

[86] B. D. Hauer, P. H. Kim, C. Doolin, A. J. R. MacDonald, H. Ramp, and J. P. Davis. On-chip cavity optomechanical coupling. *EPJ Techniques and Instrumentation*, 1:4, 2014.

[87] P. Kim. Nanoscale Torsional Optomechanics. Master's thesis, University of Alberta, 2014.

[88] T. A. Birks and Y.W. Li. The Shape of Fiber Tapers. *Journal of Lightwave Technology*, 10(4):432, 1992.

[89] S. M. Spillane, T. J. Kippenberg, O. J. Painter, and K. J. Vahala. Ideality in a Fiber-Taper-Coupled Microresonator System for Application to Cavity Quantum Electrodynamics. *Physical Review Letters*, 91(4):043902, 2003.

[90] M. Cai and K. J. Vahala. Highly efficient optical power transfer to whispering-gallery modes by use of a symmetrical dual-coupling configuration. *Optics Letters*, 25(4):260, 2000.

[91] A.Tanaka, T. Asai, K. Toubaru, H. Takashima, M. Fujiwara, R. Okamoto, and S.Takeuchi. Phase shift spectra of a fibermicrosphere system at the single photon level. *Optics Express*, 19(3):2278, 2011.

[92] M. Fujiwara, T. Noda, A. Tanaka, K. Toubaru, H.-Q. Zhao, and S. Takeuchi. Coupling of ultrathin tapered fibers with high-Q microsphere resonators at cryogenic temperatures and observation and of phase-shift transition from undercoupling to overcoupling. *Optics Express*, 20(17):19545, 2012.

[93] A. H. Safavi-Naeini, J. Chan, J. T. Hill, T. P. Mayer Alegre, A. Krause, and O. Painter. Observation of Quantum Motion of a Nanomechanical Resonator. *Physical Review Letters*, 108(3):033602, 2012.

[94] J. Fritz, M. K. Baller, H. P. Lang, H. Rothuizen, P. Vettiger, E. Meyer, H.-J. Gntherodt, Ch. Gerber, and J. K. Gimzewski. Translating Biomolecular Recognition into Nanomechanics. *Science*, 288:316, 2000.

[95] S. Schmid, S. Dohn, and A. Boisen. Real-Time Particle Mass Spectrometry Based on Resonant Micro Strings. *Sensors*, 10(9):8092–8100, 2010.

[96] T. S. Biswas, N. Miriyala, C. Doolin, X. Liu, T. Thundat, and J. P. Davis. Femtogram-Scale Photothermal Spectroscopy of Explosive Molecules on Nanostrings. *Analytical Chemistry*, 86(22):11368–11372, 2014.

[97] B. D. Hauer, C. Doolin, K. S. D. Beach, and J. P. Davis. A general procedure for thermomechanical calibration of nano/micro-mechanical resonators. *Annals of Physics*, 339:181–207, 2013.

[98] M. L. Gorodetsky, A. Schliesser, G. Anetsberger, S. Deleglise, and T. J. Kippenberg. Determination of the vacuum optomechanical coupling rate using frequency noise calibration. *Optics Express*, 18(22):23236, 2010.

[99] S. S. Verbridge, R. Ilic, H. G. Craighead, and J. M. Parpia. Size and frequency dependent gas damping of nanomechanical resonators. *Applied Physics Letters*, 93(1):013101, 2008.

[100] G. Anetsberger, R. Rivière, A. Schliesser, O. Arcizet, and T. J. Kippenberg. Ultralow-dissipation optomechanical resonators on a chip. *Nature Photon*, 2(10):627–633, 2008.

[101] R. Vacher, E. Courtens, and M. Foret. Anharmonic versus relaxational sound damping in glasses. II. Vitreous silica. *Physical Review B*, 72(21):214205, 2005.

[102] J. Classen, C. Enss, C. Bechinger, G. Weiss, and S. Hunklinger. Low frequency acoustic and dielectric measurements on glasses. *Annalen der Physik*, 3:315, 1994.

[103] Christian Enss and Siegfried Hunklinger. *Low-Temperature Physics*. Springer, 2005.

[104] A. A. Clerk and F. Marquardt. *Cavity Optomechanics*, chapter Basic Theory of Cavity Optomechanics, pages 5–24. Springer, 2014.

[105] M. Ludwig and F. Marquardt. Quantum Many-Body Dynamics in Optomechanical Arrays. *Physical Review Letters*, 111(7):073603, 2013.

[106] M. Zalalutdinov, A. Zehnder, A. Olkhovets, S. Turner, L. Sekaric, B. Ilic, D. Czaplewski, J. M. Parpia, and H. G. Craighead. Autoparametric optical drive for micromechanical oscillators. *Applied Physics Letters*, 79(5):695, 2001.

[107] M. Zhang, G. S. Wiederhecker, S. Manipatruni, A. Barnard, P. McEuen, and M. Lipson. Synchronization of Micromechanical Oscillators Using Light. *Physical Review Letters*, 109(23):233906, 2012.

[108] J. D. Teufel, D. Li, M. S. Allman, K. Cicak, A. J. Sirois, J. D. Whittaker, and R. W. Simmonds. Circuit cavity electromechanics in the strong-coupling regime. *Nature*, 471(7337):204–208, 2011.

[109] R. M. Cole, G. A. Brawley, V. P. Adiga, R. De Alba, J. M. Parpia, B. Ilic, H. G. Craighead, and W. P. Bowen. Evanescent-Field Optical Readout of Graphene Mechanical Motion at Room Temperature. *Physical Review Applied*, 3(2):024004, 2015.

[110] O. Arcizet, R. Rivière, A. Schliesser, G. Anetsberger, and T. Kippenberg. Cryogenic properties of optomechanical silica microcavities. *Physical Review A*, 80(2):021803(R), 2009.

[111] R. Rivière, S. Deléglise, S. Weis, E. Gavartin, O. Arcizet, A. Schliesser, and T. J. Kippenberg. Optomechanical sideband cooling of a micromechanical oscillator close to the quantum ground state. *Physical Review A*, 83(6):063835, 2011.

[112] J. Chan, T. P. Mayer Alegre, A. H.H. Safavi-Naeini, J. T. Hill, A. Krause, S. Gröblacher, M. Aspelmeyer, and O. Painter. Laser cooling of a nanomechanical oscillator into its quantum ground state. *Nature*, 478(7367):89–92, 2011.

[113] A. A. Clerk, M. H. Devoret, S. M. Girvin, F. Marquardt, and R. J. Schoelkopf. Introduction to quantum noise, measurement, and amplification. *Reviews of Modern Physics*, 82(2):1155–1208, 2010.

[114] T. Corbitt, Y. Chen, E. Innerhofer, H. Müller-Ebhardt, D. Ottaway, H. Rehbein, D. Sigg, S. Whitcomb, C. Wipf, and N. Mavalvala. An All-Optical Trap for a Gram-Scale Mirror. *Physical Review Letters*, 98(15):150802, 2007.

[115] M. H. Schleier-Smith, I. D. Leroux, H. Zhang, M. A. Van Camp, and V. Vuletić. Optomechanical Cavity Cooling of an Atomic Ensemble. *Physical Review Letters*, 107(14):143005, 2011.

[116] M. R. Vanner, I. Pikovski, G. D. Cole, M. S. Kim, C. Brukner, K. Hammerer, G. J. Milburn, and M. Aspelmeyer. Pulsed quantum optomechanics. *Proceedings of the National Academy of Sciences*, 108(39):16182–16187, 2011.

[117] X. Wang, S. Vinjanampathy, F. W. Strauch, and K. Jacobs. Ultraefficient Cooling of Resonators: Beating Sideband Cooling with Quantum Control. *Physical Review Letters*, 107(17):177204, 2011.

[118] Florian Elste, S. M. Girvin, and A. A. Clerk. Quantum Noise Interference and Back-action Cooling in Cavity Nanomechanics. *Physical Review Letters*, 102(20):207209, 2009.

[119] L. A. De Lorenzo and K. C. Schwab. Superfluid optomechanics coupling of a superfluid to a superconducting condensate. *New Journal of Physics*, 16:113020, 2014.

[120] J. M. Ward, D. G. O'Shea, B. J. Shortt, M. J. Morrissey, K. Deasy, and S. G. Nic Chormaic. Heat-and-pull rig for fiber taper fabrication. *Review of Scientific Instruments*, 77(8):083105, 2006.

[121] G. Brambilla, V. Finazzi, and D. J. Richardson. Ultra-low-loss optical fiber nanotapers. *Optics Express*, 12(10):2258, 2004.

[122] J. E. Hoffman, S. Ravets, J. A. Grover, P. Solano, P. R. Kordell, J. D. Wong-Campos, L. A. Orozco, and S. L. Rolston. Ultrahigh transmission optical nanofibers. *AIP Advances*, 4(6):067124, 2014.

[123] M. Pöllinger. *Bottle microresonators for applications in quantum optics and all-optical signal processing.* PhD thesis, Johannes Gutenberg Universität Mainz, 2010.

[124] D. O'Shea, C. Junge, J. Volz, and A. Rauschenbeutel. Fiber-Optical Switch Controlled by a Single Atom. *Physical Review Letters*, 111(19):193601, 2013.

[125] M. Sumetsky. Delay of Light in an Optical Bottle Resonator with Nanoscale Radius Variation: Dispersionless, Broadband, and Low Loss. *Physical Review Letters*, 111(16):163901, 2013.

[126] F. Pobell. *Matter and Methods at Low Temperatures.* Springer-Verlag, third edition, 2007.

[127] N. Kurti, N. H. Robinson, Sir F. Simon, and D. A. Spohr. Nuclear Cooling. *Nature*, 178:450, 1956.

[128] D. S. Greywall and P. A. Busch. ^{3}He-Melting-Curve Thermometry. *Journal of Low Temperature Physics*, 46(5/6):451, 1982.

[129] P. M. Berglund, H. K. Collan, G. J. Ehnholm, R. G. Gylling, and O. V. Lounasmaa. The Design and Use of Nuclear Orientation Thermometers Employing ^{54}Mn and ^{60}Co Nuclei in Ferromagnetic Hosts. *Journal of Low Temperature Physics*, 6(3/4):357, 1972.

[130] A. Haziot, X. Rojas, A. Fefferman, J. Beamish, and S. Balibar. Giant Plasticity of a Quantum Crystal. *Physical Review Letters*, 110(3):035301, 2013.

[131] S. Balibar, H. Alles, and A. Y. Parshin. The surface of helium crystals. *Reviews of Modern Physics*, 77:317, 2005.

[132] J. P. Franck and J. Jung. Dendritic Crystal Growth in Pure ^{4}He. *Journal of Low Temperature Physics*, 64:165, 1986.

[133] R. Nomura, Y. Suzuki, S. Kimura, and Y. Okuda. Interface Motion and Nucleation of Solid Helium-4 Induced by Acoustic Waves. *Physical Review Letters*, 90(7):075301, 2003.

[134] X. Rojas, A. Haziot, V. Bapst, S. Balibar, and H. J. Maris. Anomalous Softening of ^{4}He Crystals. *Physical Review Letters*, 105(14):145302, 2010.

[135] F. Souris, J. Grucker, J. Dupont-Roc, and P. Jacquier. Investigating Metastable hcp Solid Helium Below Its Melting Pressure. *Journal of Low Temperature Physics*, 162(5-6):412–420, 2011.

[136] A. J. Manninen, J. P. Pekola, G. M. Kira, J. P. Ruutu, A. V. Babkin, H. Alles, and O.V. Lounasmaa. First Optical and Observations of Superfluid ^{3}He. *Physical Review Letters*, 69(16):2392, 1992.

[137] H. Alles, J. P. Ruutu, A. V. Babkin, P. J. Hakonen, A. J. Manninen, and J. P. Pekola. Cooled video camera for optical investigations below 1-mK. *Review of Scientific Instruments*, 65(5):1784, 1994.

[138] R. Wagner, P. J. Ras, P. Remeijer, S. C. Steel, and G. Frossati. Observation of ^{3}He Crystallization down to 1 mK Using a Cooled CCD Camera. *Journal of Low Temperature Physics*, 95(5/6):715, 1994.

[139] P. J. Hakonen, H. Alles, A. V. Babkin, and J. P. Ruutu. Optical Interferometry at Ultra Low Temperatures. *Journal of Low Temperature Physics*, 101(1/2):41, 1995.

[140] H. P. Yuen and V. W. S. Chan. Noise in homodyne and heterodyne detection. *Optics Letters*, 8(3):177, 1983.

[141] T. J. Kippenberg, S. M. Spillane, and K. J. Vahala. Modal coupling in traveling-wave resonators. *Optics Letters*, 27(19):1669, 2002.

[142] U. Fano. Sullo spettro di assorbimento dei gas nobili presso il llimit dello spettro d'arco. *Nuovo Cimento*, 12:154–161, 1935.

[143] U. Fano. Effects of Configuration and Interaction on Intensities and Phase Shifts. *Physical Review*, 124(6):1866, 1961.

[144] V. S. Il'chenko and M. L. Gorodetskii. Thermal Nonlinear Effects in Optical Whispering Gallery Microresonators. *Laser Physics*, 2(6):1004, 1992.

[145] P. E. Barclay, K. Srinivasan, and O. Painter. Nonlinear response of silicon photonic crystal microresonators excited via an integrated waveguide and fiber taper. *Optics Express*, 13(3):801, 2005.

[146] F. Marquardt, J. G. E. Harris, and S. M. Girvin. Dynamical Multistability Induced by Radiation Pressure in High-Finesse Micromechanical Optical Cavities. *Physical Review Letters*, 96(10):103901, 2006.

[147] H. Rokhsari, T. J. Kippenberg, T. Carmon, and K. J. Vahala. Radiation-pressure-driven micro-mechanical oscillator. *Optics Express*, 13(14):5293, 2005.

[148] G. K. White. Thermal Expansion of Vitreous Silica at Low Temperatures. *Physical Review Letters*, 34(4):204, 1975.

[149] E. D. Black. An introduction to Pound-Drever-Hall laser frequency stabilization. *American Journal of Physics*, 69(1):79, 2001.

APPENDIX A

Mechanical Mode Thermometry[1]

This Appendix describes in greater detail the mechanical mode thermometry introduced in Section 4.3.3 for the case of a direct detection scheme. Since both the optomechanical signal and the phase modulation signal will be transduced in the transmission of a tapered fiber coupled to the optical cavity, we begin by solving the equation of motion for light in an optical cavity, which is coupled to a mechanical resonator with strength G (Equation (2.55)). We then show that the transduced signal is the power spectral density from Equation (2.41). Finally, we introduce the phase modulation into the drive term $s_{\text{in}}(t)$ and show that it gives rise to additional terms in the transmission signal which are of the same form as the optomechanical terms.

A.1 Non-Stationary State Solution to the Optomechanical Cavity

Recall that the equation of motion for light in an optical cavity coupled to the motion of a mechanical resonator $x(t)$ is given by

$$\dot{a} = -\left(\frac{\kappa}{2} - i\Delta - iGx\right) a + \sqrt{\kappa_{\text{ex}}} s_{\text{in}}. \tag{A.1}$$

where s_{in} is the input optical amplitude (in units of $\sqrt{\text{photons/s}}$) and a is the intracavity field, and κ, κ_{ex}, and G are as defined in the main text. These amplitudes are normalized in terms of photon quanta such that $|a|^2 = n_{\text{cav}}$, where n_{cav} is the number of photons in

---

[1] This analysis follows from the supplementary information in Ref. [20] and the main text of Ref. [98].

the cavity and $|s_{\mathrm{in}}|^2 = P/\hbar\omega_{\mathrm{L}}$ is the rate of photons incident on the cavity. The amplitude s_{out} output by the cavity is

$$s_{\mathrm{out}}(t) = s_{\mathrm{in}}(t) - \sqrt{\kappa_{\mathrm{ex}}}a(t), \tag{A.2}$$

which is the field that will be measured in our experiments.

In Section 2.4, we solved Equation (A.2) by linearizing the coupled equations of motion for x and a for small perturbations δx and δa around the stationary state solutions $\bar{x}$ and $\bar{a}$. Here we will not linearize Equation (A.1) since the multi-toned drive provided by the phase modulated light may prevent the cavity from reaching the steady state.

Instead, we divide the solution into the sum of two parts: $a_{\mathrm{h}}(t)$, which is the solution to the associated homogeneous differential equation and $a_{\mathrm{p}}(t)$, the particular solution to Equation (A.1) [20]. We furthermore define $a_{\mathrm{p}}(t) = a_{\mathrm{h}}(t)f(t)$ where $f(t)$ is a to-be-determined function of time which will depend on the form of $s_{\mathrm{in}}(t)$. The total solution is thus given by

$$a(t) = a_{\mathrm{h}}(t)(1 + f(t)). \tag{A.3}$$

Beginning with the homogeneous solution (where $s_{\mathrm{in}} = 0$), $a_{\mathrm{h}}(t)$, we see that it must satisfy

$$\dot{a}_{\mathrm{h}} = -\left(\frac{\kappa}{2} - i\Delta - iGx(t)\right) a_{\mathrm{h}}. \tag{A.4}$$

Integration gives

$$a_{\mathrm{h}}(t) = a_0 \exp\left(-\left[\frac{\kappa}{2} - i\Delta\right] t + iG\int x(t)dt\right), \tag{A.5}$$

where a_0 is an amplitude set by the initial conditions of the problem.

The particular solution can be found by noting that

$$\begin{aligned} \dot{a} &= \dot{a}_{\mathrm{h}} + \dot{a}_{\mathrm{p}} \\ &= \dot{a}_{\mathrm{h}} + \dot{a}_{\mathrm{h}} f + \dot{f} a_{\mathrm{h}}. \end{aligned} \tag{A.6}$$

Since $a(t)$ satisfies Equation (A.1), it follows that

$$\dot{a}_{\mathrm{h}} + \dot{a}_{\mathrm{h}} f + a_{\mathrm{h}}\dot{f} = -\left(\frac{\kappa}{2} - i\Delta - iGx(t)\right)(a_{\mathrm{h}} + a_{\mathrm{h}} f) + \sqrt{\kappa_{\mathrm{ex}}}s_{\mathrm{in}}, \tag{A.7}$$

and since $a_{\mathrm{h}}(t)$ satisfies Equation (A.4),

$$a_{\mathrm{h}}(t)\dot{f}(t) - \sqrt{\kappa_{\mathrm{ex}}}s_{\mathrm{in}} = 0. \tag{A.8}$$

The function $f(t)$ is then found by integrating

$$\dot{f} = \frac{\sqrt{\kappa_{\mathrm{ex}}}s_{\mathrm{in}}}{a_0} \exp\left(\left[\frac{\kappa}{2} - i\Delta\right] t - iG \int x(t)dt\right). \tag{A.9}$$

At this point, we can choose a form for the position, which we will take to be $x(t) = x_0 e^{-\frac{\Gamma t}{2}} \cos(\Omega_{\mathrm{m}} t)$ for a damped harmonic oscillator. Here, as in the main text, x_0 is the amplitude of motion, Γ is the mechanical damping rate and Ω_{m} is the mechanical resonator's resonance frequency. Integrating $x(t)$ in this form gives

$$\int x(t)dt = \frac{x_0 e^{-\frac{\Gamma t}{2}}}{\left(\frac{\Gamma}{2}\right)^2 + \Omega_{\mathrm{m}}^2} \left(\Omega_{\mathrm{m}} \sin(\Omega_{\mathrm{m}} t) - \frac{\Gamma}{2}\cos(\Omega_{\mathrm{m}} t)\right). \tag{A.10}$$

In the high-Q limit ($Q = \frac{\Omega_{\mathrm{m}}}{\Gamma} \gg \frac{1}{2}$), which is valid for the mechanical resonators used in our experiments, we can neglect the cosine term, and take $\Gamma \ll \Omega_{\mathrm{m}}$. The result is then

$$\int x(t)dt = \frac{x_0}{\Omega_{\mathrm{m}}} e^{-\frac{\Gamma t}{2}} \sin(\Omega_{\mathrm{m}} t). \tag{A.11}$$

Substituting this into Equation (A.5) gives

$$a_{\mathrm{h}}(t) \approx a_0 e^{-\left(\frac{\kappa}{2} - i\Delta\right)t} \left(1 + \frac{\xi}{2} e^{-\frac{\Gamma t}{2}} \left[e^{i\Omega_{\mathrm{m}} t} - e^{-i\Omega_{\mathrm{m}} t}\right]\right). \tag{A.12}$$

where we have defined

$$\xi \equiv \frac{G x_0}{\Omega_{\mathrm{m}}} \tag{A.13}$$

and used the approximation $e^{i\Lambda \sin\phi} = \sum_{k=-\infty}^{+\infty} (\pm 1)^k J_k(\Lambda) e^{ik\phi} \simeq 1 + i\Lambda \sin\phi$. In doing so, we assume that our $\Lambda = \xi e^{-\Gamma t/2} \ll 1$. It is not immediately obvious that this is the case, but note first that $e^{-\Gamma t/2}$ will always be less than 1 for finite positive time t. If we then rewrite ξ, making use of the root-mean-square of the amplitude of motion $x_0 = \sqrt{k_{\mathrm{B}} T / m_{\mathrm{eff}} \Omega_{\mathrm{m}}^2}$ given by the equipartition theorem (Equation (2.36)), we have

$$\xi = \frac{g_0\sqrt{\frac{2k_\mathrm{B}T}{\hbar\Omega_\mathrm{m}}}}{\Omega_\mathrm{m}} \simeq \frac{g_0\sqrt{2\bar{n}}}{\Omega_\mathrm{m}} \tag{A.14}$$

for $k_\mathrm{B}T \gg \hbar\Omega_\mathrm{m}$. Here we have made use of the zero-point motion of the resonator, $x_{zpf} = \sqrt{\hbar/2m_\mathrm{eff}\Omega_\mathrm{m}}$, and the vacuum optomechanical coupling rate, $g_0 = Gx_{zpf}$. In this form, we see that ξ depends only on the intrinsic parameters g_0 and Ω_m of the system, along with the average phonon occupation $\bar{n}$ of the mode (this approximation for $\bar{n}$ only breaks down at very low occupancies, $\bar{n} \ll 1$, where the full Bose-Einstein statistics must be taken into account via Equation (2.69)).

For micro- and nano-optomechanical resonators operating at optical frequencies, no device has thus far demonstrated $g_0 > \Omega_\mathrm{m}$. For devices in the resolved sideband regime ($\Omega_\mathrm{m} > \kappa$), this is an even more stringent requirement than the single-photon strong-coupling condition ($g_0 > \kappa, \Gamma$) since $\Omega_\mathrm{m} > \Gamma, \kappa$, which no optical-frequency device has yet achieved. In fact, all state-of-the-art systems remain outside these regimes by several orders of magnitude. Thus a phonon occupation of $n \gtrsim 10^6$ would be required in order for $\xi \sim 1$. For relatively high-frequency devices ($\gtrsim$10 MHz), these occupations are only achieved at temperatures well above room temperature, thus justifying our approximation.

Returning to Equation (A.9), the particular solution to Equation (A.1) is dependent on the input amplitude $s_\mathrm{in}(t)$. To illustrate optomechanical detection of the mechanical resonator, let us first consider a single-toned coherent optical drive provided by a laser at frequency ω_L. In the rotating reference frame we have been using, this corresponds simply to $s_\mathrm{in}(t) = s_\mathrm{in}$. Using this drive and Equation (A.11), Equation (A.9) becomes

$$\dot{f} = \frac{\sqrt{\kappa_\mathrm{ex}}}{a_0} s_\mathrm{in} e^{(\frac{\kappa}{2}-i\Delta)t}\left(1 - \frac{\xi}{2}e^{-\frac{\Gamma t}{2}}\left[e^{i\Omega_\mathrm{m}t} - e^{-i\Omega_\mathrm{m}t}\right]\right), \tag{A.15}$$

where we have used the same approximation as in Equation (A.12), and

$$f(t) = \frac{\sqrt{\kappa_\mathrm{ex}}}{a_0} s_\mathrm{in} e^{(\frac{\kappa}{2}-i\Delta)t}\left(\frac{1}{\frac{\kappa}{2} - i\Delta} - \frac{\xi}{2}e^{-\frac{\Gamma t}{2}}\left[\frac{e^{i\Omega_\mathrm{m}t}}{\frac{\kappa-\Gamma}{2} - i(\Delta - \Omega_\mathrm{m})} - \frac{e^{-i\Omega_\mathrm{m}t}}{\frac{\kappa-\Gamma}{2} - i(\Delta + \Omega_\mathrm{m})}\right]\right). \tag{A.16}$$

We then find $a_\mathrm{p}(t) = a_\mathrm{h}(t)f(t)$ to be

$$
\begin{aligned}
a_{\mathrm{p}}(t) = \sqrt{\kappa_{\mathrm{ex}}} s_{\mathrm{in}} \left(1 + \frac{\xi}{2} e^{-\Gamma t/2} (e^{i\Omega_{\mathrm{m}} t} - e^{-i\Omega_{\mathrm{m}} t})\right) \Bigg(& \frac{1}{\kappa/2 - i\Delta} \\
- \frac{\xi}{2} (\frac{e^{-\Gamma t/2 + i\Omega_{\mathrm{m}} t}}{\frac{\kappa - \Gamma}{2} - i(\Delta - \Omega_{\mathrm{m}})} & - \frac{e^{-\Gamma t/2 - i\Omega_{\mathrm{m}} t}}{\frac{\kappa - \Gamma}{2} - i(\Delta + \Omega_{\mathrm{m}})} \Bigg) .
\end{aligned}
\tag{A.17}
$$

Since $a_{\mathrm{h}}(t)$ (Equation (A.12)) decays with the rate κ, which is much larger than the mechanical decay rate Γ governing the decay of $a_{\mathrm{p}}(t)$, we approximate the full solution $a(t)$ by the particular solution given in Equation (A.17). Keeping only terms to first order in the small parameter ξ and taking $\kappa \gg \Gamma$ (that is, cavity photons are lost much faster than the mechanical resonator exchanges phonons with its thermal bath - valid for our experiments, which exhibit $\kappa/2\pi \sim 10$ MHz and $\Gamma/2\pi \approx 5 - 100$ kHz), we find the intracavity field to be

$$
\begin{aligned}
a(t) = \sqrt{\kappa_{\mathrm{ex}}} s_{\mathrm{in}} \Bigg(\frac{1}{\frac{\kappa}{2} - i\Delta} + \frac{\xi}{2} e^{-\frac{\Gamma t}{2}} \Bigg[& \frac{e^{i\Omega_{\mathrm{m}} t}}{\frac{\kappa}{2} - i\Delta} - \frac{e^{-i\Omega_{\mathrm{m}} t}}{\frac{\kappa}{2} - i\Delta} \\
- \frac{e^{i\Omega_{\mathrm{m}} t}}{\frac{\kappa}{2} - i(\Delta - \Omega_{\mathrm{m}})} & + \frac{e^{-i\Omega_{\mathrm{m}} t}}{\frac{\kappa}{2} - i(\Delta + \Omega_{\mathrm{m}})} \Bigg] \Bigg) ,
\end{aligned}
\tag{A.18}
$$

while the output amplitude, given by Equation (A.2), is

$$
\begin{aligned}
s_{\mathrm{out}}(t) = & s_{\mathrm{in}} \Bigg(1 - \frac{\kappa_{\mathrm{ex}}}{\frac{\kappa}{2} - i\Delta} - \frac{\kappa_{\mathrm{ex}} \xi}{2} e^{-\frac{\Gamma t}{2}} \Bigg[\frac{e^{i\Omega_{\mathrm{m}} t}}{\frac{\kappa}{2} - i\Delta} - \frac{e^{-i\Omega_{\mathrm{m}} t}}{\frac{\kappa}{2} - i\Delta} \\
& - \frac{e^{i\Omega_{\mathrm{m}} t}}{\frac{\kappa}{2} - i(\Delta - \Omega_{\mathrm{m}})} + \frac{e^{-i\Omega_{\mathrm{m}} t}}{\frac{\kappa}{2} - i(\Delta + \Omega_{\mathrm{m}})} \Bigg] \Bigg) .
\end{aligned}
\tag{A.19}
$$

A.2 Direct Detection

Let us now consider the direct detection of this transmission signal. In our experiments, we use a photodiode which is sensitive to the intensity of light passing through the taper and thus produces a voltage signal $V \propto |s_{\mathrm{out}}(t)|^2$,

$$
V_{\mathrm{out}}(t) = V_{\mathrm{DC}} + V_{\mathrm{mech}}(t). \tag{A.20}
$$

Since our photodetector will filter the low- and high-frequency signals, we have defined the time-independent signal as

$$V_{\mathrm{DC}} = H(\omega)|s_{\mathrm{in}}|^2 \left(1 - \frac{\kappa_{\mathrm{ex}}\kappa_0}{\frac{\kappa^2}{4} + \Delta^2}\right) \tag{A.21}$$

and the signal oscillating at Ω_m as

$$V_{\mathrm{mech}}(t) = H(\omega)|s_{\mathrm{in}}|^2 \frac{\xi\kappa_{\mathrm{ex}}}{2} e^{-\frac{\Gamma t}{2}} \left(\frac{C_1(\Omega_\mathrm{m})\cos\Omega_\mathrm{m} t}{D(0)D(\Omega_\mathrm{m})D(-\Omega_\mathrm{m})} + \frac{C_2(\Omega_\mathrm{m})\sin\Omega_\mathrm{m} t}{D(0)D(\Omega_\mathrm{m})D(-\Omega_\mathrm{m})}\right) \tag{A.22}$$

where $H(\omega)$ is describes all factors which contribute to the transformation of the light intensity exiting the cavity into a voltage signal. This includes optical and detector efficiencies, and the gains of the photodetector and associated electronics. It is in principle frequency-dependent, but we will assume that it is flat in the region of interest, and take $H(\omega) = H$. We have furthermore defined the coefficients

$$C_1(\Omega) = \Delta\Omega\left(-\kappa[\kappa^2 + 4\Delta^2] + \kappa_{\mathrm{ex}}[\kappa^2 + 4\Delta^2 - 4\Omega^2]\right), \tag{A.23}$$

$$C_2(\Omega) = \Delta\Omega^2\left(\kappa[4\kappa_{\mathrm{ex}} - 3\kappa] + 4[\Delta^2 - \Omega^2]\right) \tag{A.24}$$

and

$$D(\Omega) = \frac{\kappa^2}{4} + (\Delta - \Omega)^2. \tag{A.25}$$

We now find the power spectral density $S_{VV}(\omega)$ of $V_{\mathrm{mech}}(t)$ by taking its Fourier transform and squaring it, according to Equation (2.32). We begin by substituting in the form for ξ and rewriting Equation (A.22) as

$$\begin{aligned} V_{\mathrm{mech}}(t) &= \frac{H|s_{\mathrm{in}}|^2 G\kappa_{\mathrm{ex}}}{2\Omega_\mathrm{m} D(0)D(\Omega_\mathrm{m})D(-\Omega_\mathrm{m})}\Big(C_1(\Omega_\mathrm{m}) x_0 e^{-\Gamma t/2}\cos\Omega_\mathrm{m} t \\ &\quad + \frac{C_2(\Omega_\mathrm{m})}{\Omega_\mathrm{m}}\Omega_\mathrm{m} x_0 e^{-\Gamma t/2}\sin\Omega_\mathrm{m} t\Big) \\ &= H|s_{\mathrm{in}}|^2 \frac{G\kappa_{\mathrm{ex}}}{2\Omega_\mathrm{m}} \frac{(C_1(\Omega_\mathrm{m})x(t) - C_2(\Omega_\mathrm{m})\dot{x}(t)/\Omega_\mathrm{m})}{D(0)D(\Omega_\mathrm{m})D(-\Omega_\mathrm{m})} \end{aligned} \tag{A.26}$$

where we have taken

$$\begin{aligned} \dot{x}(t) &= -\Gamma \frac{x_0}{2} e^{-\Gamma t/2} \cos \Omega_\mathrm{m} t - \Omega_\mathrm{m} x_0 e^{-\Gamma t/2} \sin \Omega_\mathrm{m} t \\ &\approxeq -\Omega_\mathrm{m} x_0 e^{-\Gamma t/2} \sin \Omega_\mathrm{m} t, \end{aligned} \tag{A.27}$$

and neglected the $\cos \Omega_\mathrm{m} t$ term since $\Omega_\mathrm{m} \gg \Gamma$.

Taking the Fourier transform of Equation (A.26), we obtain

$$V_\mathrm{mech}(\omega) = H|s_\mathrm{in}|^2 \frac{G\kappa_\mathrm{ex}}{2\Omega_\mathrm{m}} \frac{(C_1(\Omega_\mathrm{m})X(\omega) - i\omega C_2(\Omega_\mathrm{m})X(\omega)/\Omega_\mathrm{m})}{D(0)D(\Omega_\mathrm{m})D(-\Omega_\mathrm{m})}, \tag{A.28}$$

which becomes

$$V_\mathrm{mech}(\omega) = H|s_\mathrm{in}|^2 \frac{G\kappa_\mathrm{ex}}{2\Omega_\mathrm{m}} \frac{(C_1(\Omega_\mathrm{m}) - iC_2(\Omega_\mathrm{m}))}{D(0)D(\Omega_\mathrm{m})D(-\Omega_\mathrm{m})} X(\omega) \tag{A.29}$$

for $\omega \approx \Omega_\mathrm{m}$. Finally, we calculate $S_{VV}(\omega)$ as in Equation (2.32),

$$\begin{aligned} S_{VV}(\omega) &= \lim_{\tau_\mathrm{m} \to \infty} \frac{1}{\tau_\mathrm{m}} |V_\mathrm{mech}(\omega)|^2 \\ &= \frac{H^2 |s_\mathrm{in}|^4 G^2 \kappa_\mathrm{ex}^2}{4\Omega_\mathrm{m}^2} \frac{C_1^2(\Omega_\mathrm{m}) + C_2^2(\Omega_\mathrm{m})}{D^2(0)D^2(\Omega_\mathrm{m})D^2(-\Omega_\mathrm{m})} \left(\lim_{\tau_\mathrm{m} \to \infty} \frac{1}{\tau_\mathrm{m}} |X(\omega)|^2 \right) \\ &= \alpha S_{xx}(\omega). \end{aligned} \tag{A.30}$$

Here, α is simply the transduction factor introduced in Equation (4.25),

$$\alpha = \frac{H^2 |s_\mathrm{in}|^4 G^2 \kappa_\mathrm{ex}^2}{4\Omega_\mathrm{m}^2} \frac{C_1^2(\Omega_\mathrm{m}) + C_2^2(\Omega_\mathrm{m})}{D^2(0)D^2(\Omega_\mathrm{m})D^2(-\Omega_\mathrm{m})}. \tag{A.31}$$

Note that if the laser is on-resonance ($\Delta = 0$), $C_1(\Omega_\mathrm{m})$ and $C_2(\Omega_\mathrm{m})$ are both zero and $S_{VV}(\omega)$ disappears, in agreement with direct detection measurements.

A.3 Phase Modulation of the Drive Laser

Now that we understand how mechanical motion can be transduced in the optical intensity, we can consider an optical drive which is weakly phase-modulated using an electro-optic modulator. This occurs through the linear electro-optical effect, where a non-linear optical crystal exhibits a voltage-dependent refractive index, altering the phase of light propagating in the crystal. In the case of a sinusoidally-varying voltage, the input laser drive to the cavity takes the form

$$s_{\text{in}}(t) = s_{\text{in}} e^{i\beta e^{-\frac{\gamma t}{2}} \sin \Omega_{\text{mod}} t}, \tag{A.32}$$

where Ω_{mod} is the frequency of the applied voltage signal and γ is the decay rate of the phase modulation process. The modulation depth or strength is given by $\beta = \pi V/V_\pi$, which is determined by the applied voltage V and the voltage required to induce a π phase shift in the crystal, V_π.

Making the same approximations as in Equation (A.12) for weak modulation ($\beta \ll 1$), we obtain

$$e^{i\beta e^{-\frac{\gamma t}{2}} \sin \Omega_{\text{mod}} t} \approx 1 + \frac{\beta}{2} e^{-\frac{\gamma t}{2}} \left(e^{i\Omega_{\text{mod}} t} - e^{-i\Omega_{\text{mod}} t} \right). \tag{A.33}$$

We see that modulating laser light in the EOM results in sidebands at frequencies $\omega_{\text{L}} \pm \Omega_{\text{mod}}$. If we consider Equation (A.33) in terms of a Bessel function expansion

$$e^{i\beta \sin \phi} = \sum_{k=-\infty}^{+\infty} (\pm 1)^k J_k(\beta) e^{ik\phi}, \tag{A.34}$$

the relative amplitude of light in the carrier and sidebands is given by the ratio $J_1(\beta e^{-\frac{\gamma t}{2}})/J_0(\beta e^{-\frac{\gamma t}{2}})$. For greater modulation strength, more terms in the Bessel function expansion must be kept, leading to higher order sidebands at $\pm k\Omega_{\text{mod}}$.

A.3.1 Intracavity Field

We again solve Equation (A.1), with $s_{\text{in}}(t)$ given by Equations (A.32) and (A.33). As before, we can divide the problem into a solution to the homogeneous equation and a solution to the particular equation. Since $a_{\text{h}}(t)$ is independent of the optical drive, it is still given by Equation (A.5), so we turn our attention to $a_{\text{p}}(t)$. The function $f(t)$ is now determined by

$$\dot{f} = \frac{\sqrt{\kappa_{\text{ex}}}}{a_0} s_{\text{in}} \left(1 + \frac{\beta}{2} e^{-\frac{\gamma t}{2}} \left(e^{i\Omega_{\text{mod}} t} - e^{-i\Omega_{\text{mod}} t} \right) \right) \times e^{\left(\frac{\kappa}{2} - i\Delta\right)t} \left(1 - \frac{\xi}{2} e^{-\frac{\Gamma t}{2}} \left(e^{i\Omega_{\text{m}} t} - e^{-i\Omega_{\text{m}} t} \right) \right). \tag{A.35}$$

As before, we integrate to find $f(t)$ and then multiply by $a_{\text{h}}(t)$ (Equation (A.12)) to obtain $a(t) \approx a_{\text{p}}(t)$,

$$\begin{aligned} a(t) \approx a_{\mathrm{p}}(t) =& \sqrt{\kappa_{\mathrm{ex}}} s_{\mathrm{in}} \left(\frac{1}{\frac{\kappa}{2} - i\Delta} + \frac{\beta}{2} e^{-\frac{\gamma t}{2}} \left[\frac{e^{i\Omega_{\mathrm{mod}} t}}{\frac{\kappa}{2} - i(\Delta - \Omega_{\mathrm{mod}})} - \frac{e^{-i\Omega_{\mathrm{mod}} t}}{\frac{\kappa}{2} - i(\Delta + \Omega_{\mathrm{mod}})} \right] \right. \\ & \left. - \frac{\xi}{2} e^{-\frac{\Gamma t}{2}} \left[\frac{e^{i\Omega_{\mathrm{m}} t}}{\frac{\kappa}{2} - i(\Delta - \Omega_{\mathrm{m}})} - \frac{e^{-i\Omega_{\mathrm{m}} t}}{\frac{\kappa}{2} - i(\Delta + \Omega_{\mathrm{m}})} - \frac{e^{i\Omega_{\mathrm{m}} t}}{\frac{\kappa}{2} - i\Delta} + \frac{e^{-i\Omega_{\mathrm{m}} t}}{\frac{\kappa}{2} - i\Delta} \right] \right), \end{aligned} \tag{A.36}$$

where we have again assumed $\kappa \gg \gamma$ and kept only terms to first order in either of the small parameters β and ξ. The output field of the cavity is then

$$\begin{aligned} s_{\mathrm{out}}(t) =& s_{\mathrm{in}} \left(1 + \frac{\beta}{2} e^{-\gamma t/2} \left[e^{i\Omega_{\mathrm{mod}} t} - e^{-i\Omega_{\mathrm{mod}} t} \right] - \frac{\kappa_{\mathrm{ex}}}{\frac{\kappa}{2} - i\Delta} \right. \\ & - \frac{\kappa_{\mathrm{ex}} \beta}{2} e^{-\frac{\gamma t}{2}} \left[\frac{e^{i\Omega_{\mathrm{mod}} t}}{\frac{\kappa}{2} - i(\Delta - \Omega_{\mathrm{mod}})} - \frac{e^{-i\Omega_{\mathrm{mod}} t}}{\frac{\kappa}{2} - i(\Delta + \Omega_{\mathrm{mod}})} \right] \\ & \left. + \frac{\kappa_{\mathrm{ex}} \xi}{2} e^{-\frac{\Gamma t}{2}} \left[\frac{e^{i\Omega_{\mathrm{m}} t}}{\frac{\kappa}{2} - i(\Delta - \Omega_{\mathrm{m}})} - \frac{e^{-i\Omega_{\mathrm{m}} t}}{\frac{\kappa}{2} - i(\Delta + \Omega_{\mathrm{m}})} - \frac{e^{i\Omega_{\mathrm{m}} t}}{\frac{\kappa}{2} - i\Delta} + \frac{e^{-i\Omega_{\mathrm{m}} t}}{\frac{\kappa}{2} - i\Delta} \right] \right). \end{aligned} \tag{A.37}$$

A.3.2 Detection

We are again interested in the power spectral density of the intensity of the light field $S_{VV}(\omega) = |V(\omega)|^2$. Squaring Equation (A.37) and keeping only terms to first order in the small parameters ξ and β, we find

$$V_{\mathrm{out}}(t) = V_{\mathrm{DC}} + V_{\mathrm{mech}}(t) + V_{\mathrm{mod}}(t), \tag{A.38}$$

where V_{DC} and $V_{\mathrm{mech}}(t)$ are defined as in Equations (A.21) and (A.22), respectively. The signal oscillating at the modulation frequency Ω_{mod} is

$$V_{\mathrm{mod}}(t) = -H|s_{\mathrm{in}}|^2 \frac{\beta \kappa_{\mathrm{ex}}}{2} e^{-\frac{\gamma t}{2}} \left[\frac{C_1(\Omega_{\mathrm{mod}}) \cos \Omega_{\mathrm{mod}} t}{D(0) D(\Omega_{\mathrm{mod}}) D(-\Omega_{\mathrm{mod}})} + \frac{C_2(\Omega_{\mathrm{mod}}) \sin \Omega_{\mathrm{mod}} t}{D(0) D(\Omega_{\mathrm{mod}}) D(-\Omega_{\mathrm{mod}})} \right]. \tag{A.39}$$

This is identical to the expression for $V_{\mathrm{mech}}(t)$ given in Equation (A.22) under the transformations $\xi \to -\beta$, $\Omega_{\mathrm{m}} \to \Omega_{\mathrm{mod}}$ and $\Gamma \to \gamma$. We can also rewrite it in terms of the original drive signal applied to the EOM $\phi(t) = \beta e^{-\gamma t/2} \sin \Omega_{\mathrm{mod}} t$,

$$V_{\rm mod}(t) = -\frac{H|s_{\rm in}|^2\kappa_{\rm ex}}{2D(0)D(\Omega_{\rm mod})D(-\Omega_{\rm mod})}\left(\frac{C_1(\Omega_{\rm mod})}{\Omega_{\rm mod}}\dot{\phi}(t) + C_2(\Omega_{\rm mod})\phi(t)\right). \tag{A.40}$$

Fourier transforming Equation (A.40) results in

$$\begin{aligned} V_{\rm mod}(\omega) &= -H|s_{\rm in}|^2\frac{\kappa_{\rm ex}}{2}\frac{(i\omega C_1(\Omega_{\rm mod})\Phi(\omega)/\Omega_{\rm mod} + C_2(\Omega_{\rm mod})\Phi(\omega))}{D(0)D(\Omega_{\rm mod})D(-\Omega_{\rm mod})} \\ &= -H|s_{\rm in}|^2\frac{\kappa_{\rm ex}}{2}\frac{(iC_1(\Omega_{\rm mod}) + C_2(\Omega_{\rm mod}))}{D(0)D(\Omega_{\rm mod})D(-\Omega_{\rm mod})}\Phi(\omega) \end{aligned} \tag{A.41}$$

where $\Phi(\omega)$ is the Fourier transform of $\phi(t)$ and we have taken $\omega \approx \Omega_{\rm mod}$.

Since the Fourier transform is linear, $V(\omega) = V_{\rm mech}(\omega) + V_{\rm mod}(\omega)$ (recall that $V_{\rm DC}$ is filtered out by the photodetector). Squaring $V(\omega)$ will yield terms proportional to $|X(\omega)|^2$, terms proportional to $|\Phi(\omega)|^2$ and cross terms proportional to $\Phi(\omega)X(\omega)$. We choose $\Omega_{\rm mod}$ such that $|\Omega_{\rm mod} - \Omega_{\rm m}| \gg \Gamma, \gamma$ (*i.e.*, such that the $\Phi(\omega)$ and $X(\omega)$ have negligible overlap) and neglect any cross terms. The result is then

$$\begin{aligned} S_{VV}(\omega) &= \lim_{\tau_{\rm m}\to\infty}\frac{1}{\tau_{\rm m}}|V(\omega)|^2 \\ &= \lim_{\tau_{\rm m}\to\infty}\frac{1}{\tau_{\rm m}}|V_{\rm mech}(\omega)|^2 + \lim_{\tau_{\rm m}\to\infty}\frac{1}{\tau_{\rm m}}|V_{\rm mod}(\omega)|^2 \\ &= \alpha S_{xx}(\omega) + \alpha_{\rm mod}S_{\phi\phi}(\omega), \end{aligned} \tag{A.42}$$

where $S_{\phi\phi}(\omega)$ is the PSD of the input phase modulation, and $\alpha_{\rm mod}$ is defined by

$$\alpha_{\rm mod} = \frac{H^2|s_{\rm in}|^4\kappa_{\rm ex}^2}{4}\frac{C_1^2(\Omega_{\rm mod}) + C_2^2(\Omega_{\rm mod})}{D^2(0)D^2(\Omega_{\rm mod})D^2(-\Omega_{\rm mod})}. \tag{A.43}$$

We see then that the phase modulation $\phi(t)$ and mechanical motion $x(t)$ are transduced into the PSD of the detector voltage through the transduction coefficients $\alpha_{\rm mod}$ and α, respectively. Since α and $\alpha_{\rm mod}$ have the same form, aside from a constant factor of $G^2/\Omega_{\rm m}^2$, the absolute displacement PSD $S_{xx}(\omega)$ can be calibrated with knowledge of the phase modulation strength $S_{\phi\phi}(\omega)$. We note that the only constraints imposed by our assumptions are that $\Omega_{\rm mod}$ and $\Omega_{\rm m}$ lie close enough in frequency that we can assume $H(\omega) = H$ is constant, and that $|\Omega_{\rm mod} - \Omega_{\rm m}| \gg \Gamma, \gamma$ so that cross terms in $S_{VV}(\omega)$ can be neglected. No restrictions have been placed on the magnitude of the optical decay rate κ relative to $\Omega_{\rm m}$ or $\Omega_{\rm mod}$, making this analysis general to optomechanical systems lying in either the resolved sideband or Doppler regimes.